

2003

Magnetohydrodynamic turbulence: The development of lattice Boltzmann methods for dissipative systems

Angus Ian Duncan Macnab
College of William & Mary - Arts & Sciences

Follow this and additional works at: <https://scholarworks.wm.edu/etd>



Part of the [Plasma and Beam Physics Commons](#)

Recommended Citation

Macnab, Angus Ian Duncan, "Magnetohydrodynamic turbulence: The development of lattice Boltzmann methods for dissipative systems" (2003). *Dissertations, Theses, and Masters Projects*. Paper 1539623425.

<https://dx.doi.org/doi:10.21220/s2-1p7e-jk10>

This Dissertation is brought to you for free and open access by the Theses, Dissertations, & Master Projects at W&M ScholarWorks. It has been accepted for inclusion in Dissertations, Theses, and Masters Projects by an authorized administrator of W&M ScholarWorks. For more information, please contact scholarworks@wm.edu.

MAGNETOHYDRODYNAMIC TURBULENCE: THE
DEVELOPMENT OF LATTICE BOLTZMANN METHODS FOR
DISSIPATIVE SYSTEMS

A Dissertation

Presented to

The Faculty of the Department of Physics
The College of William and Mary in Virginia

In Partial Fulfillment

Of the Requirements for the Degree of
Doctor of Philosophy

by

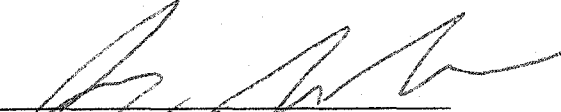
Angus I.D. Macnab

2003

APPROVAL SHEET

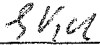
This dissertation is submitted in partial fulfillment of
the requirements for the degree of

Doctor of Philosophy

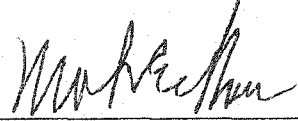


Angus I.D. Macnab

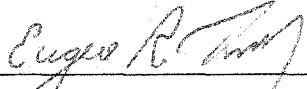
Approved, July 2003



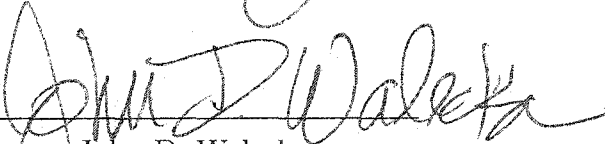
George M. Vahala



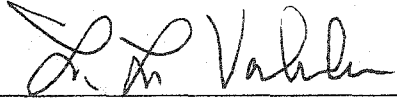
Morton Eckhause



Eugene R. Tracy



John D. Walecka



Linda L. Vahala
Old Dominion University

To my wonderful wife Amie

CONTENTS

LIST OF TABLES	viii
LIST OF FIGURES	xi
ABSTRACT	xii
CHAPTER	
1 Introduction	2
1.1 The Dynamic Evolution of Matter	2
1.2 Nonlinear Conservation Equations	3
1.3 Juxtaposition of Simulation Methods	5
2 From Kinetic Theory to the LBE	10
2.1 The Boltzmann Equation	10
2.2 BGK Collision Approximation	12
2.3 Lattice Boltzmann Equation	15
3 Basic Lattice Boltzmann Method	17
3.1 Computational Procedure	17
3.2 Chapman-Enskog Expansion	18
3.3 Specifying Distribution Functions	23
4 Resistive Magnetohydrodynamics	25
4.1 Maxwell's Equations and the MHD Approximations	25
4.2 Magnetic Induction Equation	27
4.3 Current	28
4.4 Equation of Mass Continuity	29

4.5	Momentum Evolution Equation	30
4.6	Adding Collisional Effects to MHD	32
4.7	Heuristics of MHD	33
4.8	$\nabla \cdot \mathbf{B} = 0$ Condition	34
5	LBM for 2-D Resistive MHD	37
5.1	Comparison of the Square and Octagonal Streaming Lattice	38
5.2	Bi-Directional Streaming Models	43
5.2.1	Previous Bi-Directional Streaming Models	43
5.2.2	Octagonal Bi-Directional Streaming Model	45
5.3	Two Distribution Function Models	51
5.3.1	Previous Two Distribution Function Models	51
5.3.2	Octagonal Two Distribution Function Model	52
5.4	Advantages of Two Distribution Function Models	63
6	Simulations of 2-D Resistive MHD	65
6.1	Dimensionless Parameters	65
6.2	The Orszag-Tang Vortex Model	67
6.3	Modified Orszag-Tang Vortex	76
7	Non-Uniform Grid LBMs	82
7.1	The Need for Non-Uniform Grid LBMs	82
7.1.1	LBM for Burger's Equation	84
7.1.2	Simulation of Burger's Equation	88
7.2	Unmatched Node Non-Uniform Grid LBM	92
7.2.1	Development of the Unmatched Node Model	92
7.2.2	Testing the Unmatched Node Model	94
7.3	Non-Uniform Grid LBM Using Coupled Lattices	97

7.3.1	Developing the Coupled Lattice Model	97
7.3.2	Testing the Coupled Lattice Model	104
8	Lattice Boltzmann Model for 1-D MHD	108
8.1	Derivation of the 1-D Resistive MHD Equations	108
8.2	Derivation of the LBM for 1-D Resistive MHD	111
9	Simulations of 1-D Resistive MHD	120
9.1	Comparison of MHD and Burgers Turbulence	120
9.2	A 1-D MHD Simulation Using Gaussian Wave Packets	131
9.3	1-D MHD Simulation Using an Initially Large Magnetic Field . . .	142
10	Conclusion	150
BIBLIOGRAPHY	154
VITA	157

ACKNOWLEDGMENTS

I would first like to thank my research advisor, George Vahala, for his guidance over the past three years. His calming presence always left me with a better perspective on research and on life. I would also like to thank my defense committee for their participation in the review of this dissertation.

I could not have gotten to this point without the love and support of my family, Pamela, Andrea and Jeannie. We have overcome some hurdles and had a lot of fun over the years together.

Finally, I would like to thank my wonderful wife Amie for her love and companionship over the last seven years. I have been incredibly lucky to find a best friend, intellectual partner, and soulmate contained in a single person.

LIST OF TABLES

5.1 Comparison of Transport Coefficients	64
--	----

LIST OF FIGURES

2.1	Relaxation of the Distribution Function	14
3.1	Flow Chart of the LBM Computational Procedure	18
3.2	The Octagonal Lattice	19
6.1	Initial Fields for the Orszag-Tang Vortex	68
6.2	The OT Vortex After 400 LBM Time Steps	69
6.3	The OT Vortex After 800 LBM Time Steps	70
6.4	The OT Vortex After 1600 LBM Time Steps	71
6.5	The OT Vortex After 3000 LBM Time Steps	72
6.6	The Turbulent OT Vortex After 600 LBM Time Steps	73
6.7	The Turbulent OT Vortex After 1000 LBM Time Steps	74
6.8	The Turbulent OT Vortex After 2000 LBM Time Steps	75
6.9	The Turbulent OT Vortex After 3000 LBM Time Steps	76
6.10	Initial Profile of the Modified OT Vortex	78
6.11	The Modified OT Vortex After 600 LBM Time Steps	79
6.12	The Modified OT Vortex After 1200 LBM Time Steps	80
6.13	The Modified OT Vortex After 2000 LBM Time Steps	81
7.1	Pictorial Representation of a 1-D Non-Uniform Grid	83
7.2	Uniform Grid Burger's Simulation With 600 Grid Points	89

7.3	Uniform Grid Burger's Simulation With 4800 Grid Points	90
7.4	Depiction of the 1-D Unmatched Non-Uniform Grid	92
7.5	Comparison of the Uniform and Non-Uniform Grid LBMs	95
7.6	Blow Up of the Comparison of the Uniform and Non-Uniform Grid LBMs	96
7.7	Computational Procedure for the Non-Uniform Coupled LBM	103
7.8	Comparison of the Uniform and Coupled Non-Uniform Grid LBMs	106
7.9	Blow Up of the Comparison of the Uniform and Coupled Non-Uniform Grid LBMs	107
9.1	Initial Profile of the 1-D MHD Sinusoidal Simulation	121
9.2	Early Evolution of the Velocity Profile for the 1-D MHD Simulation	123
9.3	Early Evolution of the Magnetic Field for the 1-D MHD Simulation	124
9.4	Early Evolution of the Magnetic Field for the 1-D MHD Simulation	125
9.5	A Comparison of 1-D MHD and Burger's Equation	126
9.6	A Comparison of 1-D MHD and Burger's Equation (Magnified View)	127
9.7	Late Stage Evolution of the Magnetic Field	128
9.8	Late Stage Evolution of the Magnetic Field	129
9.9	Final Profile of the 1-D MHD Fields	130
9.10	Magnified View of the Final Field Profile	131
9.11	The Temporal Evolution of the Kinetic, Magnetic and Total Energies	132
9.12	Initial Gaussian Wave Packet Velocity Profile	133
9.13	Initial Gaussian Wave Packet Magnetic Field Profile	134
9.14	Velocity Profile of the Gaussian Simulation at $t=640$	135

9.15	Magnetic Field Profile of the Gaussian Simulation at $t=640$	136
9.16	Magnetic Field Profile of the Gaussian Simulation at $t=640$	137
9.17	Kinetic Magnetic and Total Energy of the Gaussian Simulation	138
9.18	Total Energy in Wavenumber Space for the Gaussian Simulation	139
9.19	Kinetic Energy in Wavenumber Space for the Gaussian Simulation	140
9.20	Magnetic Energy in Wavenumber Space for the Gaussian Simulation	141
9.21	Profile of the Initial Fields of a Gaussian Simulation with Large Magnetic Field	143
9.22	Velocity Profile of the Large Magnetic Field Gaussian Simulation After 160 and 1280 LBM Time Steps	144
9.23	Magnetic Field of the Large Magnetic Field Gaussian Simulation After 160 and 1280 LBM Time Steps	145
9.24	Magnetic Field of the Large Magnetic Field Gaussian Simulation After 160 and 1280 LBM Time Steps	146
9.25	Kinetic, Magnetic and Total Energy of the Large Magnetic Field Gaussian Simulation	147
9.26	Kinetic, Magnetic and Total Energy Wavenumber Spectra After 18000 LBM Time Steps.	149

ABSTRACT

Computer simulations of complex phenomena have become an invaluable tool for scientists in all disciplines. These simulations serve as a tool both for theorists attempting to test the validity of new theories and for experimentalists wishing to obtain a framework for the design of new experiments. Lattice Boltzmann Methods (LBM) provide a kinetic simulation technique for solving systems governed by non-linear conservation equations. Direct LBMs use the linearized single time relaxation form of the Boltzmann equation to temporally evolve particle distribution functions on a discrete spatial lattice. We will begin with a development of LBMs from basic kinetic theory and will then show how one can construct LBMs to model incompressible resistive magnetohydrodynamic (MHD) conservation laws. We will then present our work in extending existing models to the octagonal lattice, showing that the increased isotropy of the octagonal lattice produces better numerical stability and higher Reynolds numbers in MHD simulations. Finally, we will develop LBMs that use non-uniform grids and apply them to one dimensional MHD systems.

MAGNETOHYDRODYNAMIC TURBULENCE: THE DEVELOPMENT OF
LATTICE BOLTZMANN METHODS FOR DISSIPATIVE SYSTEMS

CHAPTER 1

Introduction

1.1 The Dynamic Evolution of Matter

Whether contemplating the vortices that swirl in a cup of coffee when cream is added, the turbulence of a class four whitewater river, or the constantly changing shape that a flock of sparrows forms as they fly through the sky, the dynamic evolution of matter has an aesthetic appeal which suggests an underlying beauty in the laws which govern our universe. These laws take many different forms and can be examined at many different scales of length and time. The most fundamental of these are the theories of elementary particles, which attempt to form a consistent theory for the interaction of “point-like” objects that carry associated interaction parameters such as charge, mass and spin. The difficulty with these particle theories however, lie in the lack of tractable analytic solutions to interesting physical phenomena. Physicists to date, are only capable of exactly solving rudimentary problems involving one or two interacting bodies. The remaining majority of problems must therefore be treated with approximate solution techniques.

Many rich areas of physics consist of generating approximate macroscopic equations to model the behavior of physical phenomena which obscure the complex interactions of particle physics. This obscuration attempts to extract all of the essential phenomena of a physical problem while hiding aspects of the problem which do not fit the particular length and time scale of interest. Still these macroscopic systems, although significantly simpler than their particle based counterparts, can rarely be solved exactly. Thus the majority of physics done in the last century has consisted of finding approximate solutions to such problems. These approximation techniques can be characterized as either analytic or computational.

Analytic approximation techniques such as perturbation theory, variational methods, WKB analysis, and multiple scale analysis have been very effective in solving a number of interesting problems in physics. Their application to non-linear dissipative fluid systems such as the types of problems treated in this dissertation, however, have not been met with great success. As a result, physicists have looked to computational techniques for the approximate solution of these types of complex fluid systems.

1.2 Nonlinear Conservation Equations for Macroscopic Systems

Before discussing the computational techniques available for treating non-linear fluid systems, we would like to discuss these fluid systems in more detail. Namely, we would like to introduce some examples of fluid conservation equations, which can be treated by lattice Boltzmann methods(LBM). Consider the generalized dissipative

conservation law

$$\partial_t q_i + \partial_j p_{i,j} = \nu \partial_j^m q_i, \quad (1.1)$$

where the temporal evolution of a scalar or vector field q_i depends on the spatial derivative of a nonlinear tensor $p_{i,j}$ and a diffusive (usually dissipative or dispersive) term characterized by the higher (usually second or third) spatial derivative of the field q_i . A large number of interesting phenomena in physics are governed by this class of nonlinear conservation laws. Some examples include Burger's equation

$$\partial_t u + \partial_x \left(\frac{1}{2} u^2 \right) = \nu \partial_x^2 u, \quad (1.2)$$

which is often used to model the flow of traffic along a highway or the velocity distribution during the formation of galaxies in the early universe. The KDV equation

$$\partial_t u + \partial_x \left(\frac{1}{2} u^2 \right) = \nu \partial_x^3 u \quad (1.3)$$

is often used to model shallow water wave theory and, in particular, the existence of solitons. The Navier Stokes equations

$$\frac{\partial \rho}{\partial t} + \nabla \cdot (\rho \mathbf{v}) = 0, \quad (1.4)$$

$$\frac{\partial}{\partial t} (\rho \mathbf{v}) + \nabla P + (\mathbf{v} \cdot \nabla) (\rho \mathbf{v}) + \mathbf{v} [\nabla \cdot (\rho \mathbf{v})] = \nu \nabla^2 (\rho \mathbf{v}), \quad (1.5)$$

describe the compressible flow of fluids and are used in numerous physics, engineering and aerospace applications. And finally, the resistive magnetohydrodynamics

(MHD) equations

$$\frac{\partial \rho}{\partial t} + \nabla \cdot (\rho \mathbf{v}) = 0, \quad (1.6)$$

$$\begin{aligned} \frac{\partial}{\partial t}(\rho \mathbf{v}) + \nabla \left[P + \frac{B^2}{2} \right] + (\mathbf{v} \cdot \nabla)(\rho \mathbf{v}) + \\ \mathbf{v} [\nabla \cdot (\rho \mathbf{v})] - (\mathbf{B} \cdot \nabla) \mathbf{B} = \nu \nabla^2 (\rho \mathbf{v}), \end{aligned} \quad (1.7)$$

$$\frac{\partial \mathbf{B}}{\partial t} + (\mathbf{v} \cdot \nabla) \mathbf{B} + \mathbf{B} (\nabla \cdot \mathbf{v}) - (\mathbf{B} \cdot \nabla) \mathbf{v} = \mu \nabla^2 \mathbf{B} \quad (1.8)$$

describe the coupled interaction of the density, velocity, and magnetic fields of a conducting fluid.

1.3 A Juxtaposition of Computer Simulation

Methods

A number of computational methods exist for solving the coupled partial differential equations (or nonlinear conservation equations) that govern these types of fluid systems. The available methods can be broadly classified into two main branches: spectral methods and finite difference methods.

Spectral and pseudo-spectral methods consist of solving a set of equations in Fourier transformed wave number and wave frequency space. If they are performed correctly, these methods have the advantage that they can be exponentially accurate. An obvious disadvantage lies in the large computational overhead required to perform these calculations accurately and the limitations of these methods to simple spatial geometries. Moreover, pseudo-spectral methods, which run with better

computational efficiency than conventional spectral methods have to contend with the alternate issue of sampling errors due to aliasing phenomena. These errors arise because pseudo-spectral methods solve a portion of the nonlinear conservation equation in physical space, which necessitates the transformation of the fields between wave number and physical space. While dealiasing procedures exist, the process of transferring data between spectral and Cartesian space is undesirable from a computational standpoint. More specifically, this transformation process (or fast Fourier transformation process as this is the method that is virtually always employed) involves non-local processes which possess an inherent resistance to parallelizability. These processes do not lend themselves in a natural way, to the decomposition and assignment of tasks to large numbers of parallel processors. These types of methods have therefore fallen out of favor in recent years as computational resources have begun to focus almost entirely on massively parallel computing environments and physicists have begun to focus on simulation methods that are capable of treating realistic physical geometries, which include obstacles, boundaries, and toroidal geometries.

The general class of finite difference methods, which include finite difference; finite element and finite volume methods, sit much more favorably in the minds of most computational physicists. These methods discretize and evolve fluid equations using methods derived from the fundamental differencing rules of calculus, which reduce to exact solutions for infinitesimal values of spatial and temporal stepping. Finite element and finite volume methods use a more sophisticated treatment of the discretization to resolve field gradients within a particular element or volumetric region. The essential feature consists of working with a discretization of all of the macroscopic variables contained in a given set of coupled partial differential equations. These include position, momentum, time, and any remaining fields responsible

for self consistent and externally imposed forces. In contrast to the general class of spectral methods, finite difference methods possess a larger degree of inherent parallelizability. This is due to the relative spatial and temporal localization of the parameters which directly affect the evolution of a given quantity. This relatively localized dependence means that a spatial domain or mesh can be decomposed and assigned to an array of processors in such a way that most of the computation for a given processor involves only information which is stored in that processor's local memory buffer. The boundary regions, however must utilize information which has been transferred from the neighboring processors. This transfer of information between processors is the aspect of finite difference methods that inhibits perfect scaling of the computational time as the number of processors is increased.

Another advantage of finite difference methods comes from the ability to implement non-uniform grids in the computational procedure. Such nested or non-uniform grids have the ability to apply refined computational effort around spatial regions containing structures of interest such as shocks and current sheets. These shocks or current sheets create large gradients in the associated fields which can often only be resolved by adding to the grid density. By altering the grid density non-uniformly one can perform detailed calculations in particular regions of interest without wasting computing power on those regions without significant field gradients. Furthermore, non-uniform grid methods which adapt themselves as the fluid evolves in time, undergo what is essentially a temporal refinement process. This full Cartesian plus time refinement results in a very efficient computational procedure.

An undesirable aspect of standard finite difference methods lies in the numerical instability associated with large time evolution steps. This limitation is often overcome with the use of implicit or semi-implicit temporal evolution. While implicit temporal evolution greatly increases the size of the time step that can be used,

it comes with the cost of higher computational overhead. As a result, the most prudent computational methods attempt to attain high numerical stability using explicit temporal evolution before including more sophisticated implicit temporal evolution methods.

As a final precursor to the introduction of lattice Boltzmann methods, we will point out some of the computational difficulty associated with standard finite difference methods. Virtually all finite difference methods solve a set of fluid equations in the space of the fields contained in those equations. This required that equations containing three dimensional density, velocity and magnetic fields that evolve in time are solved in a high dimensional discretized phase space. The cost of this high dimensionality is particularly exacerbated in the solution of the nonlinear convective derivative terms. In Eqs. (1.4)-(1.8) these are the terms with single spatial derivatives operating on them. For MHD the issue of resolving these nonlinear convective derivatives is compounded by the presence of two terms in each of Eq. (1.7), and Eq. (1.8) as well as one of these terms in Eq. (1.6).

Lattice Boltzmann methods (LBMs) are also predicated upon a finite difference scheme. The key difference, however, is that a given set of particle distribution functions are solved in a linearized kinetic space. These distribution functions are then chosen in such a way that their evolution consistently models the evolution of the original set of fluid equations. The first advantage of this methodology is the avoidance of the direct solution of the nonlinear convective derivative terms. Although more parallelizable than spectral simulations, these terms are responsible for most of the non-local parts of most finite difference simulations. LBMs however reduce this non-local dependence by advectively streaming distribution functions rather than solving these convective derivatives directly. The effect is a lower dependence on non-local information and thus a better parallel performance.

Since they are based on a kinetic finite difference scheme, LBMs can also be recast in a non-uniform grid or even adaptive grid framework. The only limitation here is the inherent coupling between time and space through the lattice streaming vectors. Because of this coupling, a number of different methods have been explored which either refine time and space identically (i.e. refine the time step, spatial step and hence the streaming vector length) or utilize some sort of interpolation procedure to connect the terminal of the streaming vector with the lattice node.

Lattice Boltzmann methods provide an accurate and computationally efficient methodology for simulating fluid flow. So much so that the present simulations have utilized explicit time stepping resulting in simple efficient computational algorithms, which lend themselves to ideal parallelization of massively parallel and parallel vector computing platforms. In what follows, we present the lattice Boltzmann method applied to the problem of 2-D resistive magnetohydrodynamics systems with some extensions of the work to non-uniform grid LBMs for 1-D resistive MHD.

CHAPTER 2

From Kinetic Theory to the Lattice Boltzmann Equation

2.1 The Boltzmann Equation

We start our discussion of the kinetic theory development of the lattice Boltzmann equation by introducing the concept of a particle distribution function $f(\mathbf{r}, \mathbf{p}, t)$ where f is a function of position \mathbf{r} , momentum \mathbf{p} , and time t . This distribution function is defined such that its integral over a particular region of six dimensional phase space produces the number of particles that one would expect to find in that region at a given time.

$$\int_{\mathbf{r}-\frac{\Delta\mathbf{r}}{2}}^{\mathbf{r}+\frac{\Delta\mathbf{r}}{2}} \int_{\mathbf{p}-\frac{\Delta\mathbf{p}}{2}}^{\mathbf{p}+\frac{\Delta\mathbf{p}}{2}} f(\mathbf{r}, \mathbf{p}, t) d^3\mathbf{r} d^3\mathbf{p} = N(\mathbf{r}, \mathbf{p}, t). \quad (2.1)$$

We also have a particle number density associated with this distribution function. This quantity, which often provides more pedagogical insight, is defined as

$$\int_{-\infty}^{\infty} f(\mathbf{r}, \mathbf{p}, t) d^3\mathbf{p} = \rho(\mathbf{r}, t) \quad (2.2)$$

the integral over all possible momentum states. As we do not allow for the spontaneous creation and annihilation of particles, the conservation of particle number can be written as a generalized conservation property associated with the particle distribution function in Lagrangian form

$$f(\mathbf{r} + \mathbf{v}\delta t, \mathbf{p} + \mathbf{F}\delta t, t + \delta t) = f(\mathbf{r}, \mathbf{p}, t). \quad (2.3)$$

Changes in the particle distribution function (hereafter referred to as the distribution function) are due only to external forces acting on the particle and to internal momentum. The distribution function therefore currently exists in a collision-less state where the internal evolution of the distribution function due to particle collisions has not yet been described. We can expand Eq. (2.3) to first order in δt and express the same conservation principle as

$$\frac{df}{dt} \equiv \partial_t f + \frac{p_i}{m} \partial_i f + \frac{F_i}{m} \partial_{p_i} f = 0. \quad (2.4)$$

Partial derivatives are expressed using the notation $\partial_t \equiv \frac{\partial}{\partial t}$ and $\partial_i \equiv \nabla$ with “i” describing a tensor index. The momentum gradient is written as $\partial_{\mathbf{p}} \equiv \nabla_{\mathbf{p}}$. Henceforth, the Einstein summation notation will be implied when repeated tensor subscripts are used.

Allowing for the possibility of collisions between particles alters the number of

particles contained in a given phase space volume. Adding a generalized collision term to Eq.(2.3) gives

$$f(\mathbf{r} + \mathbf{v}\delta t, \frac{\mathbf{p}}{m} + \frac{\mathbf{F}}{m}\delta t, t + \delta t) = f(\mathbf{r}, \mathbf{p}, t) + [\frac{\partial f}{\partial t}]_{coll}\delta t. \quad (2.5)$$

Finally, expanding to first order in δt gives the collisional kinetic equation

$$[\frac{\partial}{\partial t} + \frac{\mathbf{p}}{m}\cdot\nabla + \frac{\mathbf{F}}{m}\cdot\nabla_{\mathbf{p}}]f(\mathbf{r}, \mathbf{p}, t) = [\frac{\partial f}{\partial t}]_{coll}. \quad (2.6)$$

Eq. (2.6) introduces the fully self consistent evolution of our distribution function with a generalized partial temporal derivative representing mesoscopic particle collisions.

2.2 The BGK Collision Approximation

At this point, the task of formulating solutions to the Boltzmann equation require the specification of a collisional derivative. Since it is not needed to reproduce the desired macroscopic conservation equations, explicit treatment of particle interactions using cross-sectional derivatives is not our current aim. These methods are excellent for treating the fine scale phenomena present in small groups of particles, but are too cumbersome for large scale calculations involving particle densities typical in a fluid picture where details of the collisional processes are not needed. Although computational resources continue to improve at astonishing rates, explicit particle algorithms used to model small scale kinetic processes very quickly exhaust computational resources. We are left then, to search for an appropriate approximation to the explicit collisional derivative that reproduces the correct large scale

phenomena while obscuring the fine scale processes which do not directly alter the physical system of interest.

In searching for a suitable approximation for $[\frac{\partial f}{\partial t}]_{coll}$, the BBGKY hierarchy[14] builds from the most fundamental assumptions. In our development of the lattice Boltzmann method we intend to seek out the lowest order approximation to the collisional derivative which allows us to recover a set of dissipative macroscopic fluid equations. In examining the collisional process and its affect on the evolution of particle distribution functions, Boltzmann's H theorem [23] will provide us with the key piece of information needed for developing an appropriate approximation. This theorem states that a sufficiently collisional system which is not at equilibrium will always be driven toward equilibrium and never away from it. More precisely, for the quantity H defined as

$$H \equiv \int f(\mathbf{r}, \mathbf{p}, t) \ln[f(\mathbf{r}, \mathbf{p}, t)] d^3\mathbf{r} d^3\mathbf{p}, \quad (2.7)$$

where f is any distribution function that satisfies the Boltzmann equation, it can be shown that

$$\frac{dH}{dt} \leq 0. \quad (2.8)$$

A proof of Boltzmann's famous H theorem can be found in any book on kinetic theory [22]. Fig. (2.1) shows a stylized depiction of the temporal evolution of such a distribution function averaged over some mesoscopic area of phase space. This plot is intended to demonstrate that the obvious first choice for a collisional derivative

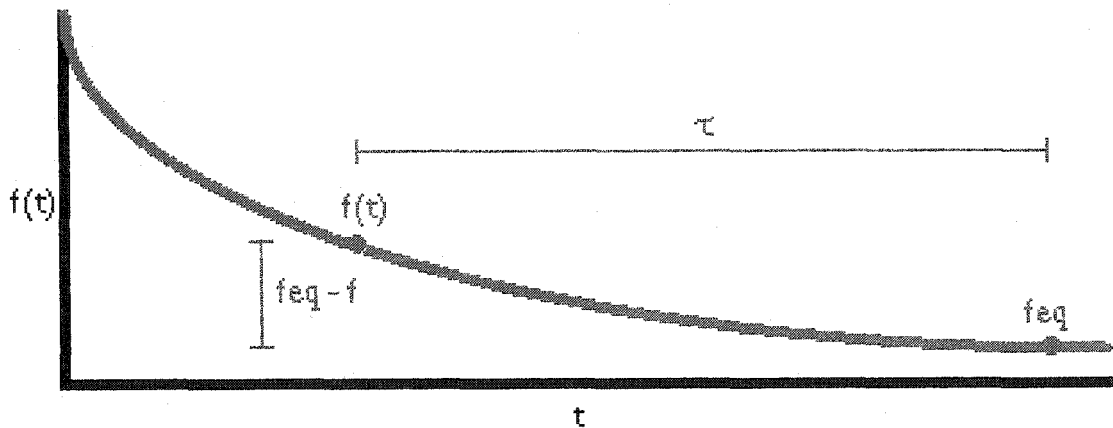


Figure 2.1: A depiction of a distribution function averaged over some mesoscopic region of phase space. The distribution function relaxes to local equilibrium illustrating the possible use of a first order difference for the approximation of this process.

should take the form of a first order forward difference derivative

$$\left[\frac{\partial f}{\partial t}\right]_{coll} \approx -\frac{f - f^{(eq)}}{\tau}, \quad (2.9)$$

which is widely known to reduce to an exact derivative in the limit of a small time step. The time step τ can be thought of as the characteristic time that it takes for the mesoscopic collisional process to drive a distribution function f toward local equilibrium (f^{eq}) in a mesoscopic region of phase space. This collisional approximation is known as the BGK single time relaxation rule[2, 9]. With this BGK collision operator in place, the Boltzmann equation takes the form

$$\left[\frac{\partial}{\partial t} + \frac{\mathbf{p}}{m} \cdot \nabla + \mathbf{F} \cdot \nabla_{\mathbf{p}}\right] f(\mathbf{r}, \mathbf{p}, t) = -\frac{f - f^{(eq)}}{\tau}. \quad (2.10)$$

We are therefore left only to discretize this equation in Cartesian and velocity space so that it can be solved computationally.

2.3 The Lattice Boltzmann Equation

At this point it is useful to restrict ourselves only to those problems which do not include any external forces. We will also rewrite the velocity in the non-canonical form $\frac{\mathbf{p}}{m} \rightarrow \mathbf{v}$. Thus the Boltzmann BGK equation appears as

$$\frac{\partial f}{\partial t} + \mathbf{v} \cdot \nabla f = -\frac{f - f^{(eq)}}{\tau}. \quad (2.11)$$

Where it should be understood that the forces which lead to the self consistent evolution of the distribution function are implicitly included in the collision term.

This simplified BGK Boltzmann equation can now be discretized in velocity space. By discretizing velocity, the particle distribution functions are automatically discretized also. A discrete number of distribution functions therefore exist for each of the discrete velocities

$$\frac{\partial f_a}{\partial t} + \mathbf{v}_a \cdot \nabla f_a = -\frac{f_a - f_a^{(eq)}}{\tau}, \quad (2.12)$$

where the subscript “a” represents any of the discrete velocities. We can discretize space such that these discrete distribution functions reside at points on a spatial lattice and time such that the transfer of information between these lattice sites occurs during discrete temporal steps. The continuous temporal and spatial derivatives are then rewritten as first order forward differences

$$\frac{f_a(x_i, t + \Delta t) - f_a(x_i, t)}{\Delta t} + v_{a,i} \frac{f_a(x_i + v_{a,i} \Delta t, t + \Delta t) - f_a(x_i, t + \Delta t)}{\Delta x} = -\frac{f_a - f_a^{(eq)}}{\tau}. \quad (2.13)$$

The act of discretizing space and time in such a manner requires that we relate

both scales through a discrete velocity vector. We therefore define the velocity vector as the discrete time step divided by a discrete spatial step $c_{a,i} \equiv \frac{\Delta x_i}{\Delta t}$. Replacing the velocities with these velocity vectors leads to

$$\frac{f_a(x_i, t + \Delta t) - f_a(x_i, t)}{\Delta t} + c_{a,i} \frac{f_a(x_i + c_{a,i} \Delta t, t + \Delta t) - f_a(x_i, t + \Delta t)}{\Delta x} = -\frac{f_a - f_a^{(eq)}}{\tau} \quad (2.14)$$

and one can readily replace $\frac{1}{\Delta t}$ with $\frac{c_{a,i}}{\Delta x}$ in the second term of the left hand side of Eq. (2.14). The first and last terms on the left hand side cancel and we are left with

$$f_a(x_i + c_{a,i} \Delta t, t + \Delta t) - f_a(x_i, t) = -\frac{\Delta t}{\tau} (f_a - f_a^{(eq)}). \quad (2.15)$$

Finally, absorbing the Δt into τ we can redefine τ as a dimensionless parameter that controls the rate of relaxation of the distribution functions. Thus the BGK lattice Boltzmann equation reads

$$f_a(x_i + c_{a,i} \Delta t, t + \Delta t) - f_a(x_i, t) = -\frac{1}{\tau} (f_a - f_a^{(eq)}). \quad (2.16)$$

It is somewhat remarkable that this discrete linearized equation can be used to recover such a large class of nonlinear macroscopic conservation equations. Furthermore, it is able to produce all of the fine scale details of fluid and magneto-fluid turbulence.

CHAPTER 3

The Basic Lattice Boltzmann Method

3.1 Computational Procedure

The computational procedure for lattice Boltzmann methods is quite straightforward. The lattice Boltzmann equation tells us that the distribution function at time $t + \Delta t$ can be calculated from the distribution function and the equilibrium distribution at time t . This computational procedure is simply split into a streaming step and a collisional step. During the streaming step the distribution functions are advected in the direction of the streaming vectors to the neighboring cells. During the collisional step moments of the advected distribution functions are taken to recover the macroscopic variables. The lattice Boltzmann equation is then evaluated to recover the new distribution functions. During the first initialization step, the initial macroscopic fields are used to create a set of distribution functions for each of the streaming vectors at each of the spatial nodes. Figure (3.1) shows a flow

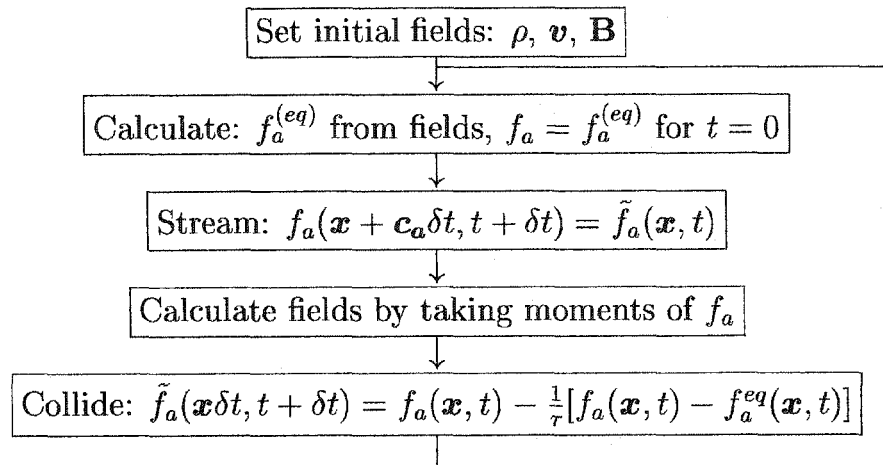


Figure 3.1: *The simple computational algorithm of lattice Boltzmann methods uses an advective streaming step and a local collision step*

chart of this simple computational procedure. These advection and collision steps can be carried out on a number of different spatial lattices. Prior two dimensional LBMs have used two dimensional square, and hexagonal lattices. Figure (3.2) shows a square spatial lattice that is connected by an octagonal streaming lattice. More will be written on the specific choice of lattices and the role that they play in the numerical stability of the models in chapter 5.

3.2 Chapman-Enskog Expansion Procedure

The critical step in deriving a LBM is the selection of a set of equilibrium distribution functions. These distribution functions are responsible for the form of the partial differential equation that is being modeled. This selection process

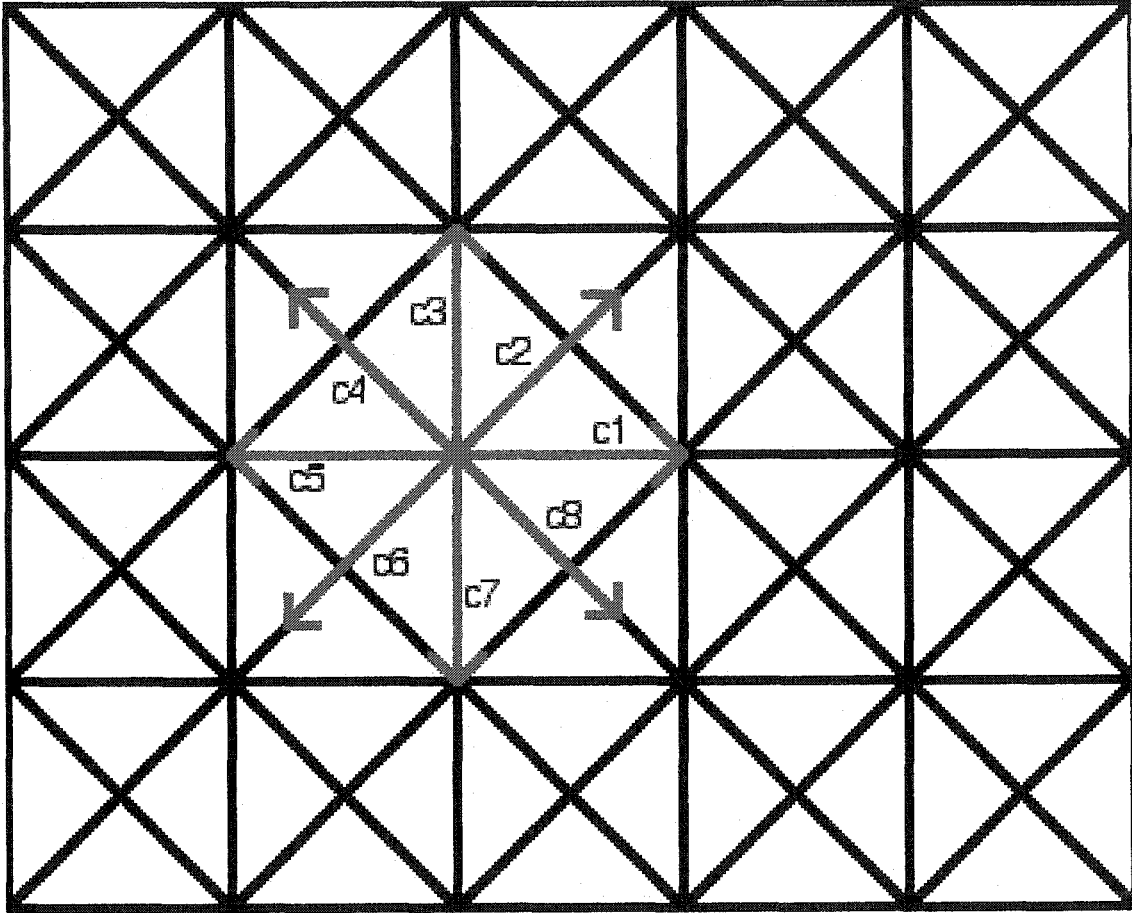


Figure 3.2: *The octagonal lattice consists of a square mesh coupled to an octagonal streaming lattice.*

is best illustrated with a Chapman-Enskog expansion procedure[7]. We begin the process by expanding the BGK lattice boltzmann equation (Eq. (2.16)) in a Taylor expansion using the small parameters Δt and $c_{a,i}\Delta t = \Delta x$. To all orders, the first term of Eq. (2.16) takes the form

$$f_a(x_i + c_{a,i}\Delta t, t + \Delta t) = \sum_{n=0}^{\infty} \frac{1}{n!} [\partial_t + c_{a,i}\partial_i]^n f_a(x_i, t), \quad (3.1)$$

which can be substituted in to Eq. (2.16) giving

$$\sum_{n=1}^{\infty} \frac{1}{n!} [\partial_t + c_{a,i} \partial_i]^n f_a(x_i, t) = -\frac{1}{\tau} (f_a - f_a^{(eq)}). \quad (3.2)$$

The lower limit on the summation has changed due to the cancellation of the first term in Eq. (3.1) with the second term in Eq. (2.16). Following the multiple scale expansion procedure of Chapman and Enskog, the partial time derivatives can be rewritten as

$$\partial_t \rightarrow \epsilon \partial_{t_0} + \epsilon^2 \partial_{t_1} + \epsilon^3 \partial_{t_2} + \epsilon^4 \partial_{t_3} + \dots \quad (3.3)$$

and the spatial derivatives become

$$\partial_i \rightarrow \epsilon \partial_i. \quad (3.4)$$

The distribution function itself is now written as

$$f_a \rightarrow f_a^{(0)} + \epsilon f_a^{(1)} + \epsilon^2 f_a^{(2)} + \epsilon^3 f_a^{(3)} + \dots \quad (3.5)$$

where the equilibrium distribution function is understood to be $f_a^{(eq)} \equiv f_a^{(0)}$ and conservation of number density requires that

$$\sum_a f_a^{(n)} = 0 \quad (3.6)$$

for all values of “n” greater than 0. Conservation of momentum density also requires that

$$\sum_a f_a^{(n)} c_{a,i} = 0 \quad (3.7)$$

for all values of “n” greater than 0.

Inserting these time scales into Eq. (3.2) and retaining only terms to the order of ϵ gives

$$\partial_{t_0} f_a^{(0)} + c_{a,i} \partial_i f_a^{(0)} = -\frac{1}{\tau} f_a^{(1)}. \quad (3.8)$$

The equation for terms to the order of ϵ^2 is

$$\partial_{t_0} f_a^{(1)} + c_{a,i} \partial_i f_a^{(1)} + \partial_{t_1} f_a^{(0)} + \frac{1}{2} [\partial_{t_0} + c_{a,i} \partial_i]^2 f_a^{(0)} = -\frac{1}{\tau} f_a^{(2)}, \quad (3.9)$$

and for terms to the order of ϵ^3 we have

$$\begin{aligned} \partial_{t_0} f_a^{(2)} + c_{a,i} \partial_i f_a^{(2)} + \partial_{t_1} f_a^{(1)} + \frac{1}{2} [\partial_{t_0} + c_{a,i} \partial_i]^2 f_a^{(1)} + \partial_{t_2} f_a^{(0)} + \\ \partial_{t_0} \partial_{t_1} f_a^{(0)} + c_{a,i} \partial_{t_1} \partial_{x_i} f_a^{(0)} + \frac{1}{6} [\partial_{t_0} + c_{a,i} \partial_i]^3 f_a^{(0)} = -\frac{1}{\tau} f_a^{(3)}. \end{aligned} \quad (3.10)$$

Equation (3.8) can be rewritten as

$$-\tau (\partial_{t_0} f_a^{(0)} + c_{a,i} \partial_i f_a^{(0)}) = f_a^{(1)}. \quad (3.11)$$

and substituted into Eq. (3.9) to eliminate all of the terms containing $f_a^{(1)}$. Eq.

(3.9) thus becomes

$$\partial_{t_1} f_a^{(0)} + \left(\frac{1}{2} - \tau\right) [\partial_{t_0} + c_{a,i} \partial_i]^2 f_a^{(0)} = -\frac{1}{\tau} f_a^{(2)}. \quad (3.12)$$

Equation (3.12) can also be rewritten as

$$-\tau \left\{ \partial_{t_1} f_a^{(0)} + \left(\frac{1}{2} - \tau\right) [\partial_{t_0} + c_{a,i} \partial_i]^2 f_a^{(0)} \right\} = f_a^{(2)}. \quad (3.13)$$

and substituted into Eq. (3.10) to eliminate all of the $f_a^{(2)}$ terms. This yields

$$\begin{aligned} \partial_{t_2} f_a^{(0)} + (1 - 2\tau) \partial_{t_1} [\partial_{t_0} + c_{a,i} \partial_i] f_a^{(0)} + \\ (\tau^2 - \tau + \frac{1}{6}) [\partial_{t_0} + c_{a,i} \partial_i]^3 f_a^{(0)} = -\frac{1}{\tau} f_a^{(3)}. \end{aligned} \quad (3.14)$$

Equations (3.8), (3.12) and (3.14) constitute the evolution equations for our distribution functions at the first three time scales. At the zeroth time scale we are able to recover a set of ideal evolution equations. That is, a set of dynamic nonlinear equations which do not include any dissipative terms. At the first time scale we recover the term responsible for dissipation and at the second time scale a term responsible for dispersion is introduced. Equations for higher order time scales can be derived which produce terms responsible for higher order diffusion. These terms become small very quickly, however, as the parameter τ is typically set to values between 1 and $\frac{1}{2}$ and the number of grid points is chosen to sufficiently minimize higher order gradients in the fields.

3.3 Specifying the Form of the Distribution

Functions

We will now outline the procedure for recovering a set of equilibrium distribution functions. As we have stated above, the form of the equilibrium distribution functions play a critical role in specifying which partial differential equations are being modeled. More precisely, the distribution functions are designed such that their moments correctly reproduce the terms of a desired set of coupled partial differential equations. In the macroscopic limit, the distribution functions appear as polynomial expansions of the field variables, hence our LBM distribution functions are written as a polynomial expansion of the relevant fields (ρ and \mathbf{v} for instance) and the streaming vectors ($c_0 = 0$ and \mathbf{c}_a for $a = 1, 2, \dots, 8$ for the octagonal case) with arbitrary constants in front of each term. For example one might begin with

$$f_0^{eq} = \rho[k_1 + k_2 c_s^2 + k_3 v^2], \quad (3.15)$$

$$f_a^{eq} = \rho[k_4 + k_5 c_s^2 + k_6 v_i c_{a,i}] + k_7 \rho v_i v_j c_{a,i} c_{a,j} + k_8 \rho v^2 \quad (3.16)$$

and by defining the zeroth moment as the density

$$\rho = f_0^{eq} + \sum_a f_a^{eq}, \quad (3.17)$$

the first moment as the momentum density

$$\rho v_i = \sum_a f_a^{eq} c_{a,i} \quad (3.18)$$

and the second moment as the momentum density flux tensor

$$\Pi_{i,j} \equiv \rho c_s^2 \delta_{i,j} + \rho v_i v_j = \sum_a f_a^{eq} c_{a,i} c_{a,j}, \quad (3.19)$$

the distribution functions then take the form

$$f_0^{eq} = \rho [1 - 2c_s^2 - v^2] \quad (3.20)$$

and

$$f_a^{eq} = \frac{\rho}{4} [c_s^2 + v_i c_{a,i}] + \frac{\rho}{2} v_i v_j c_{a,i} c_{a,j} - \frac{\rho}{8} v^2. \quad (3.21)$$

Where c_s is the sound speed and defines the pressure $P \equiv \rho c_s^2$. These distribution functions incidentally produce a model for Eqs. (1.4) and (1.5); the Navier Stokes equations. Thus by summing Eqs. (3.8), (3.12) and (3.14) over the discrete velocity directions a (this is also known as taking the zeroth moment), we recover the macroscopic continuity equations at the three time scales. And by multiplying by our lattice vector $c_{a,i}$ and summing over a (this is also known as taking the first moment) we recover the macroscopic momentum equations for the three time scales.

With the distribution functions specified, one can readily employ the computational procedure given in Fig. (3.1) to recover the dynamic evolution of a fluid system for a set of initial conditions of interest.

CHAPTER 4

Resistive Magnetohydrodynamics

4.1 Maxwell's Equations and the MHD

Approximations

Magnetohydrodynamics begins with the approximation that the evolution of a plasma can be recovered from a single fluid type without considering the individual motion of electrons and ions. This confirms the existence of well defined quantities for the density ρ , pressure P , and momentum density $\rho\mathbf{v}$. It also places some restrictions on the relative scales of a number of parameters[21]. If we define ω as the frequency of some process we wish to consider, ν as the collisional frequency of our particles, L as the length of a structure we wish to consider, l as the length of the mean free path of our particles, U_T as the thermal velocity of our particles, and τ as the characteristic time required for a particle with velocity U_T to travel the length L then the following scaling rules apply:

$$\omega \ll \nu, \tag{4.1}$$

$$l \ll L, \quad (4.2)$$

$$\frac{U_T}{L} \sim \tau, \quad (4.3)$$

$$\omega \sim \frac{1}{\tau}. \quad (4.4)$$

The fluid acts to cancel gradients in the scalar potential ϕ such that

$$q[\mathbf{E} + \frac{1}{c}\mathbf{v} \times \mathbf{B}] = 0, \quad (4.5)$$

which can be rewritten as

$$\mathbf{E} = \frac{-\mathbf{v}}{c} \times \mathbf{B}. \quad (4.6)$$

This gives the perfectly conducting limit

$$\frac{vB}{c} \sim E. \quad (4.7)$$

Finally, we choose to only consider non-relativistic motion, which gives the limit

$$\frac{v^2}{c^2} \ll 1. \quad (4.8)$$

We can now consider Maxwell's equations in Gaussian units

$$\nabla \cdot \mathbf{E} = 4\pi\rho, \quad (4.9)$$

$$\nabla \cdot \mathbf{B} = 0, \quad (4.10)$$

$$\nabla \times \mathbf{E} = \frac{-1}{c} \frac{\partial \mathbf{B}}{\partial t}, \quad (4.11)$$

and

$$\nabla \times \mathbf{B} = \frac{4\pi}{c} \mathbf{J} + \frac{1}{c} \frac{\partial \mathbf{E}}{\partial t} \quad (4.12)$$

along with our scaling rules.

4.2 Magnetic Induction Equation

Equation (4.5) can immediately be substituted into Eq. (4.11) to yield

$$\frac{\partial \mathbf{B}}{\partial t} = \nabla \times \mathbf{v} \times \mathbf{B}, \quad (4.13)$$

or in our tensor notation

$$\partial_t B_i + \partial_j (B_i v_j - v_i B_j) = 0, \quad (4.14)$$

which is known as the magnetic induction equation or freezing in law. The freezing in law necessitates that the magnetic topology is frozen into the medium such that the magnetic field lines are never able to cross or break.

It is also worthwhile to note that the divergence of Eq. (4.14) yields

$$\partial_t (\nabla \cdot \mathbf{B}) = 0, \quad (4.15)$$

due only to the fact that the divergence of the curl is equal to zero. Eq. (4.15) explicitly states that the evolution of the divergence of the magnetic field is zero. This means that without explicitly coupling Eq. (4.10) to Eq. (4.14), an initially divergence free magnetic field (i.e. a physically realistic magnetic field) will remain so for all time. We will discuss the frustrating effects that collisions have on this condition below.

4.3 Current

Inserting Eq. (4.5) into Eq. (4.12) gives

$$\nabla \times \mathbf{B} = \frac{4\pi}{c} \mathbf{J} + \frac{1}{c^2} \frac{\partial(\mathbf{v} \times \mathbf{B})}{\partial t}. \quad (4.16)$$

The relative strength of each term can be examined by writing the cross product as a scalar product, the curl as $\frac{1}{L}$, and the time derivative as $\frac{1}{\tau}$

$$\frac{B}{L} \sim \frac{J}{c} + \frac{vB}{c^2\tau}. \quad (4.17)$$

Multiplying through by L and rewriting $\frac{L}{\tau}$ as v

$$B \sim \frac{J}{c} + \frac{v^2}{c^2} B \quad (4.18)$$

shows that the last term does not affect Eq (4.16) when the limit of Eq. (4.8) is applied. We therefore rewrite the current as

$$\frac{4\pi}{c} \mathbf{J} = \nabla \times \mathbf{B}, \quad (4.19)$$

and redefine the current such that it contains the factor of $\frac{4\pi}{c}$ and adjust its units appropriately to give

$$\mathbf{J} = \nabla \times \mathbf{B}. \quad (4.20)$$

We have retained the factors of 4π and c up to this point to satisfy the scaling arguments, but the absorption of these factors into the definition of current represents a shift to natural units.

4.4 Equation of Mass Continuity

The equation for number density conservation (known as the continuity equation) can be derived from Maxwell's equations as well as by a number of other methods. If a number density is associated with each charge element then the time derivative of Eq. (4.9) and the divergence of Eq. (4.12) can be combined and manipulated to yield a density continuity equation. Here we derive the continuity equation by a more general approach. Consider some element of volume, which has particles flowing into and out of it. The particles which flow into and out of this volume are described by

$$-\int \rho \mathbf{v} \cdot d\mathbf{S} \quad (4.21)$$

where \mathbf{S} is the surface area surrounding the volume, ρ is the number density and \mathbf{v} is the macroscopic velocity in a particular region of space. The sign is negative because the \mathbf{S} vector points out of the volume element. This particle flow can be equated to the total time rate of change in particle density in the volume element

at a given time

$$\frac{d}{dt} \int \rho dV \quad (4.22)$$

to give

$$\frac{d}{dt} \int \rho dV = - \int \rho \mathbf{v} \cdot d\mathbf{S}. \quad (4.23)$$

Applying the divergence theorem to the right hand side and applying the chain rule to the left gives

$$\int \left[\frac{\partial}{\partial t} \rho + \nabla \cdot (\rho \mathbf{v}) \right] dV = 0. \quad (4.24)$$

This rule applies to the limit of infinitesimal volume elements, thus lifting the restrictions imposed by the volumetric integral. We therefore have the continuity equation for conservation of number density

$$\frac{\partial}{\partial t} \rho + \nabla \cdot (\rho \mathbf{v}) = 0, \quad (4.25)$$

or in our tensor notation

$$\partial_t \rho + \partial_i (\rho v_i) = 0. \quad (4.26)$$

4.5 Momentum Evolution Equation

In our derivation of the momentum density equation we will proceed with a methodology similar to the derivation of the continuity equation. Consider some

element of volume, which has momentum density flowing into and out of it. The rate of change of momentum density in this region is given by

$$\frac{d}{dt} \int \rho \mathbf{v} dV. \quad (4.27)$$

We can equate this to the momentum flux flowing into the volume through the surface S

$$- \int \Pi_{i,j} d\mathbf{S}_j \quad (4.28)$$

where the momentum flux is defined as

$$\Pi_{i,j} \equiv \left(P + \frac{B^2}{2} \right) \delta_{i,j} + \rho v_i v_j - B_i B_j. \quad (4.29)$$

Again, the negative sign is due to the surface vector pointing out of the volume. Eqs. (4.27) and (4.28) can now be equated to form a conservation equation of the form

$$\frac{d}{dt} \int \rho \mathbf{v} dV + \int \Pi_{i,j} d\mathbf{S}_j = 0. \quad (4.30)$$

Applying the divergence theorem on the second term gives

$$\int [\partial_t(\rho \mathbf{v}) + \partial_j \Pi_{i,j}] dV = 0 \quad (4.31)$$

which applies to arbitrarily small volume elements. This gives the differential form of the momentum equation

$$\partial_t(\rho v_i) + \partial_j[(P + \frac{B^2}{2})\delta_{i,j} + \rho v_i v_j - B_i B_j] = 0. \quad (4.32)$$

4.6 Adding Collisional Effects to MHD

While Eqs. (4.14) and (4.32) detail the evolution of the magnetic induction, the momentum density and the exchange of kinetic and magnetic energy, they do not currently contain dissipative terms originating from particle collisions. An analysis of the classic BBGKY hierarchy[14] shows that collisions add dissipative terms of the form $\partial_i^2(\rho v_i)$ and $\partial_i^2(\rho B_i)$ to Eqs. (4.14) and (4.32)

$$\partial_t B_i + \partial_j(B_i v_j - v_i B_j) = \mu \partial_j^2 B_i, \quad (4.33)$$

$$\partial_t(\rho \mathbf{v}) + \partial_j[(P + \frac{B^2}{2})\delta_{i,j} + \rho v_i v_j - B_i B_j] = \nu \partial_j^2(\rho v_i) \quad (4.34)$$

where the resistivity μ and viscosity ν control the strength of these collisional terms. The effect of these diffusive collision terms is to dissipate the momentum and magnetic fields; inhibiting the formation of high density regions in the fields.

Eq. (4.33) no longer carries the freezing in constraint, thus allowing for the crossing and breaking of magnetic field lines in a process known as magnetic reconnection. In this process, the magnetic field lines are stretched to the point where the magnetic tension is minimized by a dynamic reorganization of the magnetic topology. During this dynamic reorganization, particles that are trapped on the

fields lines can be accelerated in a “sling shot” type fashion. This process is possibly responsible for a number of MHD phenomena, including the spontaneous ejection of masses of the sun’s corona.

Taking the divergence of Eq. (4.33) also no longer gives a static condition for the evolution of the divergence of the magnetic field

$$\frac{\partial(\nabla \cdot \mathbf{B})}{\partial t} = \mu \nabla \cdot [\nabla(\nabla \cdot \mathbf{B})]. \quad (4.35)$$

This condition means that an initially divergence free magnetic field will evolve to include divergence if it is modeled by Eq. (4.33) alone. Eq. (4.10) must be explicitly enforced to satisfy the divergence free condition of the magnetic field.

4.7 Heuristics of MHD

In the interest of symmetry between the momentum and magnetic fields, it is worthwhile to introduce the definition of vorticity

$$\omega \equiv \nabla \times \mathbf{v} \quad (4.36)$$

and to suggest the possibility of an incompressible limit in which

$$\nabla \cdot \mathbf{v} = 0. \quad (4.37)$$

The symmetry of the MHD equations can be further elucidated by re-casting the momentum and magnetic induction equations in Elsasser variables[11]; yielding an elegant and fully symmetric set of equations.

4.8 On the $\nabla \cdot \mathbf{B} = 0$ Condition

Although the condition of divergence free magnetic field was briefly discussed in sections (4.3) and (4.6), we would like to take this opportunity to examine it in the context of discrete numerical simulations of resistive MHD. The addition of a resistivity term to the magnetic induction equation destroys the implicit enforcement of $\nabla \cdot \mathbf{B} = 0$ through its lack of evolution away from zero. We are therefore left to explicitly enforce the condition in our subsequent treatment of resistive MHD.

The continuous partial differential equations

$$\partial_t B_i + \partial_j (B_i v_j - v_i B_j) = \mu \partial_i^2 (\rho B_i), \quad (4.38)$$

and

$$\partial_i B_i = 0 \quad (4.39)$$

are coupled in all spatial regions during all time. The act of discretizing space and time necessitates that these equations decouple from one another within each temporal and spatial step. The computational physicist is thus left to recouple these equations at appropriate times, such that the evolution of the field consistently obeys both equations. This re-coupling, however, comes at the price of de-localizing the numerical algorithm. A cost-benefit analysis is thus required to determine the appropriate time scale with which these equations should be re-coupled. We must also keep in mind the fact that any quantity obtained through a computer simulation is only an approximation to the exact value. This includes the approximation of zero in the $\nabla \cdot \mathbf{B} = 0$ requirement.

Given a particular choice for the time scale at which the diverging part of the

magnetic field should be filtered out, the process can be accomplished through a divergence cleansing procedure[24]. Writing the total diverging and non-diverging parts of the magnetic field as the sum of the constituent parts

$$\mathbf{B}^* \equiv \nabla \times \mathbf{A} + \nabla \phi \quad (4.40)$$

allows us to see that taking the divergence of \mathbf{B}^* leaves only the non-physical part

$$\nabla \cdot \mathbf{B}^* = \nabla \cdot (\nabla \phi) \quad (4.41)$$

A process known as the projection method[1, 6] allows us to subtract this diverging part of the magnetic field without altering the non-diverging part. To do so, we Fourier transform \mathbf{B}^* and $\nabla \cdot \mathbf{B}^*$ into wavenumber space

$$\begin{aligned} \mathbf{B}^*(\mathbf{x}) \quad F.T. &\longrightarrow \mathbf{B}^*(\mathbf{k}) \\ \nabla \cdot \mathbf{B}^*(\mathbf{x}) \quad F.T. &\longrightarrow i\mathbf{k} \cdot \mathbf{B}^*(\mathbf{k}). \end{aligned}$$

The divergence can then be multiplied by $-i\mathbf{k}$ and normalized by k^2 to give the component of the magnetic field that contributes to its divergence

$$\frac{\mathbf{k}}{k^2}(\mathbf{k} \cdot \mathbf{B}^*(\mathbf{k})),$$

which can be subtracted from \mathbf{B}^* to give the divergence free part of the magnetic field in wavenumber space

$$\mathbf{B}^*(\mathbf{k}) - \frac{\mathbf{k}}{k^2}(\mathbf{k} \cdot \mathbf{B}^*(\mathbf{k})) = \mathbf{B}(\mathbf{k}). \quad (4.42)$$

We can then inverse Fourier transform the divergence free magnetic field back into Cartesian space.

As we pointed out in the introduction, any Fourier transforming process is a global procedure that lacks an inherent parallelizability. Although considerable effort has been placed on the optimization of Fourier transforming procedures, one should exercise great care in deciding how often this cleansing procedure should be invoked.

CHAPTER 5

Lattice Boltzmann Models for 2-D Resistive MHD

The difficulty in modeling MHD using lattice Boltzmann methods arises from the existence of two distinct fields that occupy the same rank in the BBGKY hierarchy. More explicitly, the BBGKY hierarchy often specifies the zeroth moment as the density field, the first moment as the momentum density field, the second moment as the momentum density flux tensor and so on. The magnetic field however, should also arise from a moment similar to that of the momentum density field and the magnetic flux tensor should arise from a moment similar to that of the momentum density flux tensor. This means that we cannot specify the magnetic moments simply as higher moments of our distribution functions. Additionally, we must pay careful attention to the symmetry properties of the momentum density and magnetic flux tensors under interchange of the indices i and j . The momentum

density flux tensor is invariant under i, j interchange

$$\bigwedge_{i \leftrightarrow j} \Pi_{i,j} = \left(P + \frac{B^2}{2}\right) \delta_{i,j} + \rho v_i v_j - B_i B_j = \Pi_{i,j}, \quad (5.1)$$

while the magnetic flux tensor is antisymmetric under i, j interchange

$$\bigwedge_{i \leftrightarrow j} \Lambda_{i,j} = B_i v_j - v_i B_j = -\Lambda_{i,j}. \quad (5.2)$$

These interchange properties translate to similar requirements that need to be placed on the moments that produce these tensors. The moment that produces the momentum flux tensor must be symmetric under interchange of i and j and the moment that produces the magnetic flux tensor must not be symmetric under interchange of i and j . The lack of symmetry imposed on the magnetic flux tensor's moment is thus less restrictive than the antisymmetry of the tensor itself.

These interchange properties have been correctly reproduced in LBMs using two different schemes; bi-directional streaming models and two distribution function models.

5.1 A Comparison of the Square and Octagonal Streaming Lattice

Before delving into the specifics of Bi-directional Streaming and Two Distribution function LBMs, we would like to justify our use of an octagonal lattice for these LBM MHD models. The octagonal lattice consists of eight equal length streaming

vectors

$$c_{a,i} = |c| \left[\cos \frac{2\pi(a-1)}{8}, \sin \frac{2\pi(a-1)}{8} \right], a = 1 \dots 8 \quad (5.3)$$

and a zero velocity vector

$$c_{0,i} = [0, 0] \quad (5.4)$$

where the magnitude $|c|$ can be adjusted arbitrarily. The products of these streaming vectors form the tensors

$$T_i^{(1)} \equiv \sum_{a=0}^8 c_{a,i} = 0, \quad (5.5)$$

$$T_{i,j}^{(2)} \equiv \sum_{a=0}^8 c_{a,i} c_{a,j} = 4c^2 \delta_{i,j}, \quad (5.6)$$

$$T_{i,j,k}^{(3)} \equiv \sum_{a=0}^8 c_{a,i} c_{a,j} c_{a,k} = 0, \quad (5.7)$$

$$T_{i,j,k,l}^{(4)} \equiv \sum_{a=0}^8 c_{a,i} c_{a,j} c_{a,k} c_{a,l} = 4c^4 [\delta_{i,j} \delta_{k,l} + \delta_{i,k} \delta_{j,l} + \delta_{i,l} \delta_{j,k}] \quad (5.8)$$

where the odd moments are always zero due to the invariance of the lattice under any $n\frac{\pi}{4}$ rotation and the $\delta_{\alpha,\beta}$ represents the rank two Kronecker delta. By contrast,

the square streaming lattice given by

$$c_{a,i} = |c| \left[\cos \frac{2\pi(a-1)}{4}, \sin \frac{2\pi(a-1)}{4} \right], a = 1 \dots 4 \quad (5.9)$$

$$c_{0,i} = [0, 0] \quad (5.10)$$

produces the tensors

$$T_i^{(1)} \equiv \sum_{a=0}^4 c_{a,i} = 0, \quad (5.11)$$

$$T_{i,j}^{(2)} \equiv \sum_{a=0}^4 c_{a,i} c_{a,j} = 2c^2 \delta_{i,j}, \quad (5.12)$$

$$T_{i,j,k}^{(3)} \equiv \sum_{a=0}^4 c_{a,i} c_{a,j} c_{a,k} = 0, \quad (5.13)$$

$$T_{i,j,k,l}^{(4)} \equiv \sum_{a=0}^4 c_{a,i} c_{a,j} c_{a,k} c_{a,l} = 2c^4 \delta_{i,j,k,l} \quad (5.14)$$

where the odd moments are always zero due to the invariance of the lattice under any $n\frac{\pi}{2}$ rotation and the $\delta_{\alpha,\beta,\gamma,\delta}$ represents the fourth rank Kronecker delta. The reduced set of invariant rotation operators (or lower isotropy) of the square lattice result in the presence of the less isotropic fourth rank Kronecker delta. The higher isotropy of the octagonal lattice is precisely the reason that we choose it for our present simulations despite the two fold increase in information that needs to be

streamed to the neighboring cells. The octagonal lattice was initially introduced in formulations of a thermal lattice Boltzmann model (TLBM) for the Navier Stokes equations. Vahala et al.[25, 26] found that the increased isotropy of the octagonal lattice increases the numerical stability of LBMs[20]. This deduction is heuristically justified by the idea that an octagonal lattice represents a more descriptive discretization of the two dimensional velocity space and thus comes closer to sampling a true Maxwellian distribution.

A consequence of using the octagonal lattice comes from the fact that the diagonal streaming vectors do not terminate at the point of a lattice node. This can be thought of as representing a decoupling of the velocity space streaming lattice and the Cartesian space distribution function lattice. To recouple these lattices, or to connect the vector terminals with the corresponding spatial nodes, we utilize a second order Lagrange interpolation defined by

$$P(z) \equiv \sum_{\alpha=1}^n P_{\alpha}(z) \quad (5.15)$$

where the P_{α} are defined by

$$P_{\alpha}(z) \equiv \prod_{\substack{\beta=1 \\ \beta \neq \alpha}}^3 \frac{z - z_{\beta}}{z_{\alpha} - z_{\beta}} r_{\alpha}. \quad (5.16)$$

The distance between the spatial nodes in the “x” and “y” directions is $|c|$ and the distance between spatial nodes and their diagonal neighbor is $\sqrt{2c^2}$. If we define the diagonal line $y = x$, as the “z” axis and a given spatial node as lying at the zero point on the “z” axis, then the nearest diagonal vector terminals lie at $c - \sqrt{8c^2}, c - \sqrt{2c^2}$,

and c . We can therefore specify the P_α as

$$P_1(0) = \frac{(c - \sqrt{2c^2})c}{(c - \sqrt{8c^2} - c + \sqrt{2c^2})(c - \sqrt{8c^2} - c)} r_1 = \frac{1 - \sqrt{2}}{4} r_1, \quad (5.17)$$

$$P_2(0) = \frac{(c - \sqrt{8c^2})c}{(c - \sqrt{2c^2} - c + \sqrt{8c^2})(c - \sqrt{2c^2} - c)} r_2 = (\sqrt{2} - \frac{1}{2}) r_2, \quad (5.18)$$

$$P_3(0) = \frac{(c - \sqrt{8c^2})(c - \sqrt{2c^2})}{(c - c + \sqrt{8c^2})(c - c + \sqrt{2c^2})} r_3 = \frac{5 - 3\sqrt{2}}{4} r_3. \quad (5.19)$$

We can replace the $P(z)$ with the diagonal distribution functions and r_1 , r_2 and r_3 with their nearest corresponding diagonal neighbors. The streaming step from Fig. (3.1) is therefore replaced by this interpolation step. For a node location given by “ i ” and “ j ”, the four diagonal distribution functions are interpolated with

$$f_2(i, j) = P_1 f_2(i - 1, j - 1) + P_2 f_2(i, j) + P_3 f_2(i + 1, j + 1), \quad (5.20)$$

$$f_4(i, j) = P_1 f_4(i + 1, j - 1) + P_2 f_4(i, j) + P_3 f_4(i - 1, j + 1), \quad (5.21)$$

$$f_6(i, j) = P_1 f_6(i + 1, j + 1) + P_2 f_6(i, j) + P_3 f_6(i - 1, j - 1), \quad (5.22)$$

$$f_8(i, j) = P_1 f_8(i - 1, j + 1) + P_2 f_8(i, j) + P_3 f_8(i + 1, j - 1). \quad (5.23)$$

And because these interpolating polynomials are static, the procedure can be easily

incorporated into the computational procedure.

5.2 Bi-Directional Streaming Models

5.2.1 Previous Bi-Directional Streaming Models

The bi-directional streaming methodology for the hexagonal lattice was developed by Martinez et al.[18] from an earlier model by Chen et al.[8]. The model uses distribution functions with two streaming vectors embedded in them. The distribution functions are therefore streamed in the direction of the primary streaming vector given by $c_{a,i}$ and in the direction of a secondary streaming vector given by $c_{b,i}$, which can point only in one of two directions. We therefore have

$$a = 1, 2, 3, \dots$$

$$b = a + 1, a - 1 \quad (\text{mod } a).$$

Composite vectors are written as

$$d_{a,b,i} = (1 - w)c_{a,i} + wc_{b,i} \quad (5.24)$$

$$e_{a,b,i} = qc_{a,i} + rc_{b,i} \quad (5.25)$$

where the weights w , q and r will be adjusted to correctly model the macroscopic MHD equations. These composite vectors are then used in the distribution functions

such that the following moments are enforced:

$$\rho = f_0^{eq} + \sum_{a,b} f_{a,b}^{eq}, \quad (5.26)$$

$$\rho v_i = \sum_{a,b} f_{a,b}^{eq} d_{a,b,i}, \quad (5.27)$$

$$\Pi_{i,j} = \sum_{a,b} f_{a,b}^{eq} d_{a,b,i} d_{a,b,j}, \quad (5.28)$$

$$\rho B_i = \sum_{a,b} f_{a,b}^{eq} e_{a,b,i}, \quad (5.29)$$

$$\rho \Lambda_{i,j} = \sum_{a,b} f_{a,b}^{eq} e_{a,b,i} d_{a,b,j}. \quad (5.30)$$

Bi-directional streaming models have the advantage that a single distribution function is used and only a limited amount of information is transferred between lattice nodes. Their difficulties lie in the more complex tensors formed from the products of the streaming vectors when moments are taken

$$\begin{aligned} \sum_{a,b} d_{a,b,i} d_{a,b,j}, \quad \sum_{a,b} e_{a,b,i} e_{a,b,j}, \quad \sum_{a,b} d_{a,b,i} d_{a,b,j} d_{a,b,k} d_{a,b,l}, \\ \sum_{a,b} e_{a,b,i} e_{a,b,j} e_{a,b,k} e_{a,b,l}, \quad \sum_{a,b} d_{a,b,i} d_{a,b,j} e_{a,b,k} e_{a,b,l}. \end{aligned}$$

These points are best illustrated with the outline of our derivation of the octagonal

model, which will follow in the next section.

5.2.2 Octagonal Bi-Directional Streaming Model

In this section we will present an outline of the octagonal bi-directional streaming model that we have developed[16]. Because this dissertation focuses primarily on the two distribution function methodology, we will not include a detailed derivation of the Chapman-Enskog expansion procedure and the subsequent macroscopic conservation equations that are recovered from this process, but will provide enough information to give a feel for the essence of the procedure.

The octagonal lattice given by Eqs. (5.3) and (5.4) is used with the bi-directional streaming methodology. For the secondary streaming vectors we use the two vectors that are orthogonal to the primary vectors. We therefore have

$$a = 1, 2, 3, \dots, 8$$

$$b = a + 2, a - 2 \pmod{8}.$$

We need to rewrite Eq. (2.16) as a backward difference rather than a forward difference. This has no effect on the physics of the model as both forms reduce to the exact derivative in the limit of infinitesimal time steps. By exchanging $x_i + c_{n,i}\Delta t$ for x_i , $t + \Delta t$ for t , x_i for $x_i - c_{n,i}$, and t for $t - \Delta t$; Eq. (2.16) is rewritten as

$$\begin{aligned} f_n(x_i, t) - f_n(x_i - c_{n,i}\Delta t, -t\Delta t) = \\ - \frac{1}{\tau} [f_n(x_i - c_{n,i}\Delta t, -t\Delta t) - f_n^{(eq)}(x_i - c_{n,i}\Delta t, -t\Delta t)] \end{aligned} \quad (5.31)$$

We can now split the streaming step into its two streaming directions. The general

$c_{n,i}$ vectors are thus decomposed into $c_{a,i}$ and $c_{b,i}$ and we normalize each streaming direction such that a weighting factor of $\frac{1}{2}$ appears in front of each distribution function. Equation (5.31) thus becomes

$$\begin{aligned} f_{a,b}(x_i, t) - \frac{1}{2}f_{a,b}(x_i - c_{a,i}\Delta t, -t\Delta t) - \frac{1}{2}f_{a,b}(x_i - c_{b,i}\Delta t, -t\Delta t) = \\ - \frac{1}{\tau} \left[\frac{1}{2}f_{a,b}(x_i - c_{a,i}\Delta t, -t\Delta t) + \frac{1}{2}f_{a,b}(x_i - c_{b,i}\Delta t, -t\Delta t) \right. \\ \left. - \frac{1}{2}f_{a,b}^{(eq)}(x_i - c_{a,i}\Delta t, -t\Delta t) - \frac{1}{2}f_{a,b}^{(eq)}(x_i - c_{b,i}\Delta t, -t\Delta t) \right]. \end{aligned} \quad (5.32)$$

Taylor expanding Eq. (5.32) to the first order in time and space gives

$$\begin{aligned} \frac{1}{2}(\partial_t + c_{a,i}\partial_i)f_{a,b} + \frac{1}{2}(\partial_t + c_{b,i}\partial_i)f_{a,b} = \\ \frac{1}{\tau} \left[\frac{1}{2}(\partial_t + c_{a,i}\partial_i)(f_{a,b} - f_{a,b}^{(eq)}) + \frac{1}{2}(\partial_t + c_{b,i}\partial_i)(f_{a,b} - f_{a,b}^{(eq)}) \right] \end{aligned} \quad (5.33)$$

where we have retained the factor of $\frac{1}{2}$ to emphasize the weighting imposed on the streaming directions and to remind us that higher order terms in the Taylor expansion exist. The terms in Eq. (5.33) can be regrouped and written as

$$[\partial_t + \frac{1}{2}(c_{a,i} + c_{b,i})\partial_i]f_{a,b} = \frac{1}{\tau}[\partial_t + \frac{1}{2}(c_{a,i} + c_{b,i})\partial_i](f_{a,b} - f_{a,b}^{(eq)}), \quad (5.34)$$

which elucidates an obvious choice for the weighting factor in Eq. (5.24). Upon choosing $w = \frac{1}{2}$ Eq. (5.34) takes the form

$$(\partial_t + d_{a,b,i}\partial_i)f_{a,b} = \frac{1}{\tau}(\partial_t + d_{a,b,i}\partial_i)(f_{a,b} - f_{a,b}^{(eq)}). \quad (5.35)$$

Because our first composite vector takes the symmetric form

$$d_{a,b,i} = \frac{1}{2}(c_{a,i} + c_{b,i}) \quad (5.36)$$

we choose an antisymmetric form for the second vector. Setting $q = -\frac{1}{2}$ and $r = \frac{1}{2}$ gives

$$e_{a,b,i} = \frac{1}{2}(-c_{a,i} + c_{b,i}). \quad (5.37)$$

The distribution functions themselves can now be written as the equilibrium distribution function plus a perturbation

$$f_{a,b} = f_{a,b}^{(0)} + \epsilon f_{a,b}^{(1)} \quad (5.38)$$

where $f_{a,b}^{(0)} \equiv f_{a,b}^{(eq)}$. Incorporating this expansion into Eq. (5.31) gives

$$(\partial_t + d_{a,b,i}\partial_i)(f_{a,b}^{(0)} + \epsilon f_{a,b}^{(1)}) = \frac{1}{\tau}(\partial_t + d_{a,b,i}\partial_i)\epsilon f_{a,b}^{(1)}. \quad (5.39)$$

and retaining only the terms to the zeroth power of ϵ provides us with

$$\partial_t f_{a,b}^{(0)} + d_{a,b,i}\partial_i f_{a,b}^{(0)} = 0. \quad (5.40)$$

And finally, moving the streaming vector inside the partial derivative produces

$$\partial_t f_{a,b}^{(0)} + \partial_i f_{a,b}^{(0)} d_{a,b,i} = 0, \quad (5.41)$$

which we can use to recover the ideal level macroscopic MHD equations. Equation (5.40) can also be multiplied by $d_{a,b,i}$ to give

$$\partial_t f_{a,b}^{(0)} + \partial_i f_{a,b}^{(0)} d_{a,b,i} d_{a,b,j} = 0, \quad (5.42)$$

and can be multiplied by $e_{a,b,i}$ to give

$$\partial_t f_{a,b}^{(0)} + \partial_i f_{a,b}^{(0)} e_{a,b,i} d_{a,b,j} = 0, \quad (5.43)$$

The tensor relationships which are formed by summing products of the tensors over "a" and "b" are needed for a derivation of the specific form of the distribution functions. These tensor relationships are

$$\sum_{a,b} c_{a,i} c_{a,j} = \sum_{a,b} c_{b,i} c_{b,j} = 8\delta_{i,j}$$

$$\sum_{a,b} c_{a,i} c_{a,j} c_{a,k} c_{a,l} = 2(\delta_{i,j}\delta_{k,l} + \delta_{i,k}\delta_{j,l} + \delta_{i,l}\delta_{j,k})$$

$$\sum_{a,b} c_{b,i} c_{b,j} c_{b,k} c_{b,l} = 2(\delta_{i,j}\delta_{k,l} + \delta_{i,k}\delta_{j,l} + \delta_{i,l}\delta_{j,k})$$

$$\sum_{a,b} c_{a,i} c_{a,j} c_{b,k} c_{b,l} = 6\delta_{i,j}\delta_{k,l} + 2\delta_{i,k}\delta_{j,l} + 2\delta_{i,l}\delta_{j,k}$$

where all of the odd combinations of $c_{a,i}$ and $c_{b,j}$ equal zero. These tensor relationships, used with Eqs. (5.26) - (5.30), specify the equilibrium distribution functions

$$f_0^{(eq)} = \rho - 4P - 2\rho v^2 \quad (5.44)$$

$$f_{a,b}^{(eq)} = \frac{P}{4} + \frac{\rho}{4} [v_i d_{a,b,i} + B_i e_{a,b,i} + 2(v_i v_i c_{a,i} c_{b,j} - B_i B_j c_{a,i} c_{b,j}) + v_i B_j c_{a,i} c_{b,j} - B_i v_j c_{a,i} c_{b,j} + \frac{v^2}{2}] \quad (5.45)$$

where “P” is the fluid pressure and will require a closure approximation to represent it as some combination of the other fields. The closure approximation that is typically made is to define the pressure as $P = \rho c_s^2$ where c_s is the constant sound speed. More will be written on this approximation in section 5.3.2. With the distribution functions specified, Eq. (5.41) can be summed over “a” and “b” to give

$$\partial_t \sum_{a,b} f_{a,b}^{(0)} + \partial_i \sum_{a,b} f_{a,b}^{(0)} d_{a,b,i} = \partial_t \rho + \partial_i(\rho v_i) = 0, \quad (5.46)$$

which is the continuity equation. Summing Eq. (5.42) gives

$$\begin{aligned} \partial_t \sum_{a,b} f_{a,b}^{(0)} + \partial_i \sum_{a,b} f_{a,b}^{(0)} d_{a,b,i} d_{a,b,j} = \\ \partial_t(\rho v_i) + \partial_j \left[\left(\rho c_s^2 + \frac{\rho B^2}{2} \right) \delta_{i,j} + \rho v_i v_j - \rho B_i B_j \right] = 0 \end{aligned} \quad (5.47)$$

and defines our ideal momentum flux equation. Finally, Eq. (5.43) can be summed to recover

$$\partial_t \sum_{a,b} f_{a,b}^{(0)} + \partial_i \sum_{a,b} f_{a,b}^{(0)} e_{a,b,i} d_{a,b,j} = \partial_t(\rho B_i) + \partial_j(\rho B_i v_j - \rho v_i B_j) = 0, \quad (5.48)$$

which constitutes our ideal magnetic flux equation.

A full Chapman Enskog expansion of the higher order derivatives in the Taylor expansion can be used to recover the collision level MHD equations. This procedure is treated in detail in section 5.3.2, but will not be given here. The process produces the following dissipative MHD equations:

$$\partial_t \rho + \partial_i(\rho v_i) = 0, \quad (5.49)$$

$$\begin{aligned} \partial_t(\rho v_i) + \partial_j[(\rho c_s^2 + \frac{B^2}{2})\delta_{i,j} + \rho v_i v_j - B_i B_j] = \\ \nu \partial_j^2(\rho v_i) + \nu_b \partial_j \partial_i(\rho v_i) + O(\nabla^2 \mathbf{A}_n^3), \end{aligned} \quad (5.50)$$

$$\partial_t(\rho B_i) + \partial_j(\rho B_i v_j - \rho v_i B_j) = \mu \partial_j^2(\rho B_i) + \mu_b \partial_j \partial_i(\rho B_i) + O(\nabla^2 \mathbf{A}_n^3), \quad (5.51)$$

where the viscosity, bulk viscosity, resistivity, and bulk resistivity are respectively defined as

$$\nu \equiv \frac{\tau + 1}{8}, \quad (5.52)$$

$$\nu_b \equiv \frac{1}{8}[\tau(2 - c_s^2) + \frac{c_s^2}{2}], \quad (5.53)$$

$$\mu \equiv \frac{3\tau - 1}{8}, \quad (5.54)$$

$$\mu_b \equiv \frac{1 - \tau}{4}. \quad (5.55)$$

The higher order terms containing three fold combinations of the fields and two spatial derivatives are represented by $O(\nabla^2 \mathbf{A}_n^3)$.

Before discussing the advantages and disadvantages of this bi-directional streaming methodology we will present the two distribution function method and derive the model in full detail. A comparison of the two methods will then be presented in section 5.4.

5.3 Two Distribution Function Models

5.3.1 Previous Two Distribution Function Models

The two distribution function methodology for the square lattice was initially developed by Dellar[10]. The model uses a single streaming vector and the standard scalar distribution function for the density

$$\rho = f_0^{eq} + \sum_a f_a^{eq}, \quad (5.56)$$

momentum

$$\rho \mathbf{v} = \sum_a f_a^{eq} \mathbf{c}_a, \quad (5.57)$$

and momentum flux tensor

$$\Pi_{i,j} = \sum_a f_a^{eq} c_{a,i} c_{a,j}. \quad (5.58)$$

However, for the magnetic field and magnetic flux tensor a separate distribution function is used. Since a magnetic continuity equation does not exist, the magnetic field must come from the zeroth moment of the second distribution function. This necessitates that the second distribution function be a vector rather than a scalar. The zeroth moment of this vector distribution function gives the magnetic field

$$B_i = g_{0,i}^{eq} + \sum_a g_{a,i}^{eq} \quad (5.59)$$

and the first moment gives the magnetic flux tensor

$$\Lambda_{i,j} \equiv B_i v_j - v_i B_j = \sum_a g_{a,i}^{eq} c_{a,j}. \quad (5.60)$$

The generalized expansions for both of these distribution functions contain the velocity and magnetic field, which is how they influence one another. Specifically, the density and momentum density come from moments of $f_a^{(eq)}$ and are used to calculate $g_{a,i}^{(eq)}$. Conversely, the magnetic field comes from moments of $g_{a,i}^{(eq)}$ and are used to calculate $f_a^{(eq)}$.

5.3.2 Octagonal Two Distribution Function Model

We begin our derivation of the octagonal two distribution function model[17] by writing the distribution functions as generalized expansions of the octagonal lattice vectors and our macroscopic fields $\rho, v_i,$ and B_i

$$f_0^{eq} = k_1 \rho + k_2 \rho v^2 + k_3 B^2, \quad (5.61)$$

$$f_a^{eq} = k_4 \rho + k_5 \rho v_i c_{a,i} + k_6 \rho v_i v_j c_{a,i} c_{a,j} + k_7 B_i B_j c_{a,i} c_{a,j} + k_8 \rho v^2 + k_9 B^2, \quad (5.62)$$

$$g_{0,i}^{eq} = k_{10} B_i, \quad (5.63)$$

$$g_{a,i}^{eq} = k_{11} B_i + k_{12} B_i v_j c_{a,j} + k_{13} v_i B_j c_{a,j}. \quad (5.64)$$

The enforcement of Eq. (5.56) specifies the requirements

$$k_1 + 8k_4 = 1, \quad (5.65)$$

$$k_2 + 4c^2k_6 + 8k_8 = 0, \quad (5.66)$$

$$k_3 + 4c^2k_7 + 8k_9 = 0. \quad (5.67)$$

The enforcement of Eq. (5.57) specifies the requirement

$$4c^2k_5 = 1, \quad (5.68)$$

and the enforcement of Eq. (5.58) specifies the requirements

$$4c^2k_4 = \frac{P}{\rho}, \quad (5.69)$$

$$c^4k_6 + 4c^2k_8 = 0, \quad (5.70)$$

$$c^4k_7 + 4c^2k_9 = 0, \quad (5.71)$$

$$2c^4k_8 = 1, \quad (5.72)$$

$$2c^4 k_7 = -1. \quad (5.73)$$

Solving Eqs. (5.65)-(5.73) for k_1 - k_9 specifies the algebraic form for all of the expansion coefficients in Eqs. (5.61) and (5.62)

$$\begin{aligned} k_1 &= 1 - \frac{2P}{\rho c^2} & k_2 &= -\frac{1}{c^2} & k_3 &= \frac{-1}{c^2} \\ k_4 &= \frac{P}{4\rho c^2} & k_5 &= \frac{1}{4c^2} & k_6 &= \frac{1}{2c^4} \\ k_7 &= -\frac{1}{2c^4} & k_8 &= -\frac{1}{8c^2} & k_9 &= \frac{1}{4c^2}. \end{aligned}$$

Eqs. (5.61) and (5.62) thus take the form

$$f_0^{eq} = \rho - \frac{2\rho c_s^2}{c^2} - \frac{\rho}{c^2} v^2 - \frac{1}{c^2} B^2, \quad (5.74)$$

$$f_a^{eq} = \frac{\rho c_s^2}{4c^2} + \frac{\rho}{4c^2} v_i c_{a,i} + \frac{\rho}{2c^4} v_i v_j c_{a,i} c_{a,j} - \frac{\rho}{8c^2} v^2 - \frac{1}{2c^4} B_i B_j c_{a,i} c_{a,j} + \frac{1}{4c^2} B^2. \quad (5.75)$$

We have made the closure approximation for the pressure

$$\frac{P}{\rho} = c_s^2. \quad (5.76)$$

where c_s is the constant sound speed, which we are free to adjust arbitrarily.

Enforcement of Eq. (5.59) specifies the requirement

$$k_{10} + 8k_{11} = 1 \quad (5.77)$$

and enforcement of Eq. (5.60) specifies the requirements

$$4c^2 k_{12} = 1, \quad (5.78)$$

$$4c^2 k_{13} = 1. \quad (5.79)$$

If we define $k_{11} \equiv \frac{\alpha}{8}$, then the expansion coefficients in Eqs. (5.63) and (5.64) become

$$\begin{aligned} k_{10} &= 1 - \alpha, & k_{11} &= \frac{\alpha}{8} \\ k_{12} &= \frac{1}{4c_2} k_{13} = -\frac{1}{4c_2} \end{aligned}$$

Eqs. (5.63) and (5.64) thus take the form

$$g_{0,i}^{eq} = (1 - \alpha)B_i, \quad (5.80)$$

$$g_{a,i}^{eq} = \frac{\alpha}{8}B_i + \frac{1}{4c^2}(B_i v_j c_{a,j} - v_i B_j c_{a,j}) \quad (5.81)$$

where α is an arbitrary constant that will affect the viscosity.

We can now use Eqs. (5.74), (5.75), (5.80) and (5.75) to derive the macroscopic MHD equations, which this LBM simulates. Moving the lattice vectors inside the partial derivatives of Eq. (3.8)

$$\partial_b f_a^{(0)} + \partial_i f_a^{(0)} c_{a,i} = -\frac{1}{\tau} f_a^{(1)} \quad (5.82)$$

and summing over all of the lattice vector directions

$$\partial_{t_0} \sum_{a=0}^8 f_a^{(0)} + \partial_i \sum_{a=0}^8 f_a^{(0)} c_{a,i} = -\frac{1}{\tau} \sum_{a=0}^8 f_a^{(1)} \quad (5.83)$$

produces

$$\partial_{t_0} \rho + \partial_i (\rho v_i) = 0 \quad (5.84)$$

where Eq. (3.6) provides that the right hand side of Eq. (5.83) is equal to zero.

In order to reproduce the magnetic induction equation, we apply a similar process using our $g_{a,i}^{(0)}$ distribution function. This yields

$$\partial_{t_0} B_i + \partial_j (B_i v_j - v_i B_j) = 0. \quad (5.85)$$

Eq. (3.12) can also be multiplied by $c_{a,i}$

$$\partial_{t_0} f_a^{(0)} c_{a,i} + \partial_j f_a^{(0)} c_{a,i} c_{a,j} = -\frac{1}{\tau} f_a^{(1)} c_{a,i} \quad (5.86)$$

and summed over velocity space

$$\partial_{t_0} \sum_{a=0}^8 f_a^{(0)} c_{a,i} + \partial_j \sum_{a=0}^8 f_a^{(0)} c_{a,i} c_{a,j} = -\frac{1}{\tau} \sum_{a=0}^8 f_a^{(1)} c_{a,i} \quad (5.87)$$

to yield

$$\partial_{t_0} (\rho v_i) + \partial_j \left[(\rho c_s^2 + \frac{B^2}{2}) \delta_{i,j} + \rho v_i v_j - B_i B_j \right] = 0. \quad (5.88)$$

where Eq. (3.7) again provides that the left hand side of Eq. (5.87) is equal to zero.

Eqs. (5.84), (5.85) and (5.88) constitute the conservation equations at the zeroth

time scale. These equations are also known as the Euler level or ideal equations.

Employing the same method as was used above, the zeroth moment of Eq. (3.12) can be taken for the $f_a^{(0)}$ distribution function to yield

$$\partial_{t_1} \rho - \left(\tau_\nu - \frac{1}{2}\right) [\partial_{t_0}^2 \rho + 2\partial_{t_0} \partial_i (\rho v_i) + \partial_i \partial_j \Pi_{i,j}] = 0 \quad (5.89)$$

where the new subscript ν of τ indicates that this is the relaxation parameter that is associated with the $f_a^{(0)}$ distribution function. By expanding and regrouping the third term in Eq. (5.89)

$$\partial_{t_1} \rho - \left(\tau_\nu - \frac{1}{2}\right) \partial_{t_0} [\partial_{t_0} \rho + \partial_i (\rho v_i)] - \left(\tau_\nu - \frac{1}{2}\right) \partial_i [\partial_{t_0} (\rho v_i) + \partial_j \Pi_{i,j}] = 0 \quad (5.90)$$

and recognizing that the second and third terms of Eq. (5.90) are the left hand sides of Eqs. (5.84) and (5.88) respectively, we end up with

$$\partial_{t_1} \rho = 0. \quad (5.91)$$

Thus the continuity equation at the first time scale does not contribute any additional changes to the density profile.

The zeroth moment of Eq. (3.12) can also be taken for the $g_{a,i}^{(0)}$ distribution function to yield

$$\partial_{t_1} B_i - \left(\tau_\mu - \frac{1}{2}\right) [\partial_{t_0}^2 B_i + 2\partial_{t_0} \partial_j \Lambda_{i,j} + \partial_j \partial_k \sum_{a=0}^8 g_{a,i}^{(0)} c_{a,j} c_{a,k}] = 0 \quad (5.92)$$

where the subscript μ of τ indicates that this is the relaxation parameter that is associated with the $g_a^{(0)}$ distribution function. Expanding and regrouping the third

term in Eq. (5.92) leads to

$$\begin{aligned} \partial_{t_1} B_i - (\tau_\mu - \frac{1}{2}) \partial_{t_0} [\partial_{t_0} B_i + \partial_j \Lambda_{i,j}] - \\ (\tau_\mu - \frac{1}{2}) \partial_j [\partial_{t_0} \Lambda_{i,j} + \partial_k \sum_{a=0}^8 g_{a,i}^{(0)} c_{a,j} c_{a,k}] = 0. \end{aligned} \quad (5.93)$$

Equation (5.85) cancels the second term in Eq. (5.93) to give

$$\partial_{t_1} B_i - (\tau_\mu - \frac{1}{2}) \partial_j [\partial_{t_0} \Lambda_{i,j} + \partial_k \sum_{a=0}^8 g_{a,i}^{(0)} c_{a,j} c_{a,k}] = 0. \quad (5.94)$$

and we are left to define the last term in Eq. (5.94). Performing the sum over “a” gives

$$\sum_{a=0}^8 g_{a,i}^{(0)} c_{a,j} c_{a,k} = \frac{\alpha c^2}{2} B_i \delta_{j,k}, \quad (5.95)$$

which can be substituted into Eq. (5.94) with the $\Lambda_{i,j}$ tensor written out explicitly

$$\partial_{t_1} B_i - (\tau_\mu - \frac{1}{2}) \partial_j [\partial_{t_0} (B_i v_j - v_i B_j) + \partial_k \frac{\alpha c^2}{2} B_i \delta_{j,k}] = 0. \quad (5.96)$$

Applying the product rule to the temporal derivative in the second term of Eq. (5.96) gives

$$\begin{aligned} \partial_{t_1} B_i - (\tau_\mu - \frac{1}{2}) \partial_j [B_i \partial_{t_0} v_j + v_j \partial_{t_0} B_i - \\ v_i \partial_{t_0} B_j - B_j \partial_{t_0} v_i + \partial_k \frac{\alpha c^2}{2} B_i \delta_{j,k}] = 0. \end{aligned} \quad (5.97)$$

Equations (5.88) and (5.85) can be used to exchange all of the ∂_{t_0} time derivatives

for the corresponding spatial derivative. This gives

$$\begin{aligned} \partial_{t_1} B_i - (\tau_\mu - \frac{1}{2}) \partial_j [- B_i \partial_k \Pi_{j,k} - v_j \partial_k \Lambda_{i,k} + \\ v_i \partial_k \Lambda_{j,k} + B_j \partial_k \Pi_{i,k} + \partial_k \frac{\alpha c^2}{2} B_i \delta_{j,k}] = 0. \end{aligned} \quad (5.98)$$

Finally, we will rewrite Eq. (5.98) as

$$\partial_{t_1} B_i = \mu \partial_j^2 B_i + O(\nabla^2 \mathbf{A}_n^3) \quad (5.99)$$

where

$$\mu \equiv \frac{\alpha c^2 (2\tau_\mu - 1)}{4}. \quad (5.100)$$

The higher order terms with two spatial derivatives and three fold combinations of the momentum density and magnetic fields are represented by $O(\nabla^2 \mathbf{A}_n^3)$. Equation (5.99) thus constitutes our evolution equation for the magnetic field at the first time scale. The inclusion of the BGK collision term at this time scale introduces magnetic resistivity into the evolution.

In deriving the momentum flux equation at the first time scale we multiply Eq. (3.12) by $c_{a,i}$ and sum over velocity space

$$\partial_{t_1} (\rho v_i) - (\tau_\nu - \frac{1}{2}) [\partial_{t_0}^2 (\rho v_i) + 2 \partial_{t_0} \partial_j \Pi_{i,j} + \partial_j \partial_k \sum_{a=0}^8 f_a^{(0)} c_{a,i} c_{a,j} c_{a,k}] = 0. \quad (5.101)$$

Expanding and regrouping the third term in Eq. (5.101) leads to

$$\begin{aligned} \partial_{t_1} (\rho v_i) - (\tau_\nu - \frac{1}{2}) \partial_{t_0} [\partial_{t_0} (\rho v_i) + \partial_j \Pi_{i,j}] - \\ (\tau_\nu - \frac{1}{2}) \partial_j [\partial_{t_0} \Pi_{i,j} + \partial_k \sum_{a=0}^8 f_a^{(0)} c_{a,i} c_{a,j} c_{a,k}] = 0. \end{aligned} \quad (5.102)$$

Equation (5.88) cancels the second term in Eq. (5.102) to give

$$\partial_{t_1}(\rho v_i) - (\tau_\nu - \frac{1}{2})\partial_j[\partial_{t_0}\Pi_{i,j} + \partial_k \sum_{a=0}^8 f_a^{(0)} c_{a,i} c_{a,j} c_{a,k}] = 0. \quad (5.103)$$

and we are left to define the last term in Eq. (5.103). Performing the sum over “a” involves the rank four tensor, giving a slightly more complex expression than we have dealt with above

$$\sum_{a=0}^8 f_a^{(0)} c_{a,i} c_{a,j} c_{a,k} = \frac{\rho c^2}{4} (v_l \delta_{i,j} \delta_{k,l} + v_l \delta_{i,k} \delta_{j,l} + v_l \delta_{i,l} \delta_{j,k}), \quad (5.104)$$

which can be substituted into Eq. (5.103) with the $\Pi_{i,j}$ tensor written out explicitly

$$\begin{aligned} \partial_{t_1}(\rho v_i) - (\tau_\nu - \frac{1}{2})\partial_j \{ \partial_{t_0} [(\rho c_s^2 + \frac{B^2}{2}) \delta_{i,j} + \rho v_i v_j - B_i B_j] + \\ \partial_k \frac{\rho c^2}{4} (v_l \delta_{i,j} \delta_{k,l} + v_l \delta_{i,k} \delta_{j,l} + v_l \delta_{i,l} \delta_{j,k}) \} = 0. \end{aligned} \quad (5.105)$$

Applying the product rule to the temporal derivative in the second term of Eq. (5.105), distributing ∂_j and enforcing the Kronecker deltas gives

$$\begin{aligned} \partial_{t_1}(\rho v_i) - (\tau_\nu - \frac{1}{2}) \{ c_s^2 \partial_i \partial_{t_0} \rho + \partial_j B_i \partial_{t_0} B_i + \\ \partial_j v_i \partial_{t_0}(\rho v_j) + \partial_j v_j \partial_{t_0}(\rho v_i) - \partial_j B_i \partial_{t_0} B_j - \\ \partial_j B_j \partial_{t_0} B_i + \frac{c^2}{4} [\partial_i \partial_k (\rho v_k) + \partial_i \partial_j (\rho v_j) + \partial_j^2 (\rho v_i)] \} = 0. \end{aligned} \quad (5.106)$$

Equations (5.84), (5.88) and (5.85) can be used to exchange all of the ∂_{t_0} time

derivatives for the corresponding spatial derivative. This gives

$$\begin{aligned} \partial_{t_1}(\rho v_i) + (\tau_\nu - \frac{1}{2})\{c_s^2 \partial_i \partial_l(\rho v_l) + \partial_j B_i \partial_l \Lambda_{i,l} + \\ \partial_j v_i \partial_l \Pi_{j,l} + \partial_j v_j \partial_l \Pi_{i,l} - \partial_j B_i \partial_l \Lambda_{j,l} - \\ \partial_j B_j \partial_l \Lambda_{i,l} - \frac{c^2}{4}[\partial_i \partial_k(\rho v_i) + \partial_i \partial_j(\rho v_i) + \partial_j^2(\rho v_i)]\} = 0. \end{aligned} \quad (5.107)$$

Again, the higher order terms with three fold combinations of the momentum density and magnetic fields will be represented by $O(\nabla^3 \mathbf{A}_n^3)$. The $\Pi_{i,j}$ tensor, however, does contribute a pressure term which will be retained for further analysis. Equation (5.107) is thus rewritten as

$$\begin{aligned} \partial_{t_1}(\rho v_i) + (\tau_\nu - \frac{1}{2})\{c_s^2 \partial_i \partial_l(\rho v_l) + c_s^2 \partial_j v_i \partial_j \rho + c_s^2 \partial_j v_j \partial_i \rho - \\ \frac{c^2}{4}[\partial_i \partial_k(\rho v_i) + \partial_i \partial_j(\rho v_i) + \partial_j^2(\rho v_i)]\} = O(\nabla^3 \mathbf{A}_n^3). \end{aligned} \quad (5.108)$$

The second term of Eq. (5.108) can be combined with the fifth and sixth terms and the coefficients can be rewritten to give

$$\begin{aligned} \partial_{t_1}(\rho v_i) = \nu \partial_j^2(\rho v_i) + \nu_b \partial_j \partial_i(\rho v_i) + \\ (\frac{1}{2} - \tau_\nu) c_s^2 (\partial_j v_i \partial_j \rho + c_s^2 \partial_j v_j \partial_i \rho) + O(\nabla^2 \mathbf{A}_n^3) \end{aligned} \quad (5.109)$$

where

$$\nu \equiv \frac{c^2(2\tau_\nu - 1)}{8} \quad (5.110)$$

and

$$\nu_b \equiv (\frac{c^2}{2} - c_s^2)(\tau_\nu - \frac{1}{2}). \quad (5.111)$$

Equation (5.109) constitutes our evolution equation for the momentum density field at the first time scale. The BGK collision approximation introduces a viscosity and bulk viscosity term which tend to dissipate the momentum density field. Additionally, we wish only to consider those problems which use an initially uniform density field. This provides a near incompressible limit in which $\nabla\rho \approx 0$. Thus the $\nabla\rho$ terms can be eliminated from Eq. (5.109) and we rewrite it as

$$\partial_{t_1}(\rho v_i) = \nu \partial_j^2(\rho v_i) + \nu_b \partial_j \partial_i(\rho v_i) + O(\nabla^2 \mathbf{A}_n^3) \quad (5.112)$$

Finally, the total time evolution is truncated such that we do not include small perturbations of the fields due to the higher order time scales. We can therefore add Eqs. (5.84) and (5.91) to produce the total time evolution of the density field

$$\partial_t \rho + \partial_i(\rho v_i) = 0. \quad (5.113)$$

Also adding Eqs. (5.88) and (5.109) produces

$$\begin{aligned} \partial_t(\rho v_i) + \partial_j \left[\left(\rho c_s^2 + \frac{B^2}{2} \right) \delta_{i,j} + \rho v_i v_j - B_i B_j \right] = \\ \nu \partial_j^2(\rho v_i) + \nu_b \partial_j \partial_i(\rho v_i) + O(\nabla^3 \mathbf{A}_n^3) \end{aligned} \quad (5.114)$$

and adding Eqs. (5.85) and (5.99) gives

$$\partial_t B_i + \partial_j (B_i v_j - v_i B_j) = \mu \partial_j^2 B_i + O(\nabla^3 \mathbf{A}_n^3). \quad (5.115)$$

While this model contains some additional terms due to spurious third order nonlinear derivatives, higher order inaccuracies are expected in any finite difference numerical modeling procedure. Because these higher order derivatives grow small

very quickly for small gradients in the fields, they did not introduce significant errors in the simulations of two dimensional resistive MHD that are presented in chapter 6.

5.4 Advantages of Two Distribution Function

Models

It is worthwhile to briefly juxtapose the bi-directional streaming and two distribution function methodologies. This will elucidate our choice in using the latter method in most of our recent simulations. From the standpoint of computational efficiency, the two distribution function method exchanges more information between lattice nodes than the Martinez et al.[18] reduced bi-directional streaming model and less information than the Chen et al.[8] full bi-directional streaming model. Specifically, our octagonal formulation of the reduced bi-directional streaming model advects 16 distribution functions to its neighboring cells, our octagonal two function model advects 24 distribution functions and a fully bi-directional streaming octagonal model would advect 64 distribution functions. The motivation behind using the two distribution function methodology lies first in the ability to independently control the viscosity and resistivity terms, whereas in the bi-directional methodology the viscosity and resistivity are controlled by a single relaxation constant.

Next, the form of the transport coefficients themselves are inherently lower in the two distribution function models than those produced by the bi-directional models. Achieving values for the viscosity and resistivity which approach the regions which are of interest to physicists studying astrophysical and tokamak plasmas has typically been met with some difficulty. These lower transport coefficients have

Model	Viscosity	Resistivity
Square: Bi-Stream	$\frac{\tau+1}{6}$	$\frac{3\tau-1}{6}$
Hexagonal: Bi-Stream	$\frac{3\tau}{16}$	$\frac{9\tau-4}{16}$
Octagonal: Bi-Stream	$\frac{\tau+1}{8}$	$\frac{2\tau+1}{16}$
Octagonal: 2 Functions	$\frac{2\tau_\nu-1}{8}$	$\frac{\alpha(2\tau_\mu-1)}{4}$

Table 5.1: *A comparison of the transport coefficients for square, hexagonal and octagonal bi-directional streaming models and for the octagonal two distribution function model. For a given value of τ in the region $\frac{1}{2} < \tau < 1$ the octagonal two distribution function model gives the lowest value for both the viscosity and resistivity.*

allowed us to run simulations at higher Reynolds and magnetic Reynolds numbers than has previously been reported for LBMs. Table 5.1 shows a comparison of the transport coefficients for our octagonal bi-directional streaming and two distribution function models along with those of the square and hexagonal Martinez et al.[18] models where the vector length “c” has been set to 1 for all of the models. Numerical stability constraints require that τ be larger than $\frac{1}{2}$ for all of the models and values of τ greater than 1 are generally too dissipative to be of interest to the plasma physics community.

Another advantage in the two distribution function method comes from the fact that fewer constraints are imposed on the distribution functions. This results in a free parameter “ α ” in the resistivity, which can be adjusted arbitrarily.

Finally, the bi-directional streaming modeling procedure introduces a bulk resistivity term, which is undesirable. This term represents the transport order divergence in magnetic field and thus introduces more error in the magnetic induction equation than the corresponding two distribution function model. For these reasons, we chose to focus most of our computational effort on the two distribution function method after we had developed both models.

CHAPTER 6

Simulations of 2-D Resistive Magnetohydrodynamics

6.1 Dimensionless Parameters

In our simulations of resistive MHD it is useful to define a set of dimensionless parameters, which can be used to compare the results we obtain with previously published results. It will also be useful because we may wish to compare LBM simulations which use different numbers of grid points and different initial velocity and magnetic fields with one another. A dimensional analysis of Eqs. (4.34) and (4.33) reveal that the viscosity and resistivity parameters carry units of $\frac{\text{length}^2}{\text{time}}$. The Reynolds and magnetic Reynolds numbers are typically defined as the inverse of the viscosity and resistivity, respectively. In order to make the Reynolds numbers dimensionless we must multiply by the length scale of the LBM model (i.e. the number of grid points along one dimension of a 2-D square box) and the magnitude

of the initial field

$$Re \equiv \frac{v_0 \cdot xsize}{\nu} \quad (6.1)$$

$$Rm \equiv \frac{B_0 \cdot xsize}{\mu} \quad (6.2)$$

where “*xsize*” represents the number of grid points in one dimension. In two dimensional rectangular simulations with different numbers of grid points in each dimension the square root of the total area $\sqrt{xsize \cdot ysize}$, should be used.

A dimensionless time scale can also be defined for the evolution of the velocity and magnetic topologies. For this dimensionless time scale we simply use the length scale of the LBM and the magnitude of the initial velocity field such that

$$t_v = \frac{v_0}{xsize} t_{LBM}. \quad (6.3)$$

Previous authors[18, 27] have used this single dimensionless time scale to gauge the evolution of both the magnetic and velocity fields. While this method is consistent in the context of a pure fluid dynamics paradigm, it is only consistent in the MHD paradigm because they consistently set the initial magnetic field equal to the initial velocity field $v_0 = B_0$. This single time scale, however, is not useful in examining initial conditions which contain an initially large magnetic field and an initially small velocity field. In these cases, much of the evolution is governed by the strength of the magnetic field. We therefore define a dimensionless magnetic time scale that is

analogous to its velocity field counterpart

$$t_m = \frac{B_0}{xsize} t_{LBM}. \quad (6.4)$$

a self consistent total dimensionless time scale is thus defined by

$$t_t = \sqrt{t_v^2 + t_m^2}. \quad (6.5)$$

This total time scale serves as a much more useful gauge for the total evolution of the velocity and magnetic fields and is essential in tracking the exchange of kinetic and magnetic energies as a function of time. It should be noted that this time scale reduces to the velocity field time scale if B_0 is set to zero and to the magnetic field time scale if v_0 is set to zero.

6.2 The Orszag-Tang Vortex Model

The Orszag-Tang vortex model[19] provides a useful set of periodic initial conditions for testing the reliability of our model. It consists of large scale variations of the velocity and magnetic fields, which readily decay into thin small scale sheets containing large field gradients. These initial conditions are also useful because they do not require any randomly excited modes to force the system to evolve to a turbulent state, thus providing a reproducible system. Most notable, the decay process contains many of the phenomena of interest to plasma physicists including magnetic reconnection and the formation of current sheets. Biskamp and Welter[5, 3, 4] generalized the Orszag-Tang vortex by adding arbitrary phase shifts. The initial

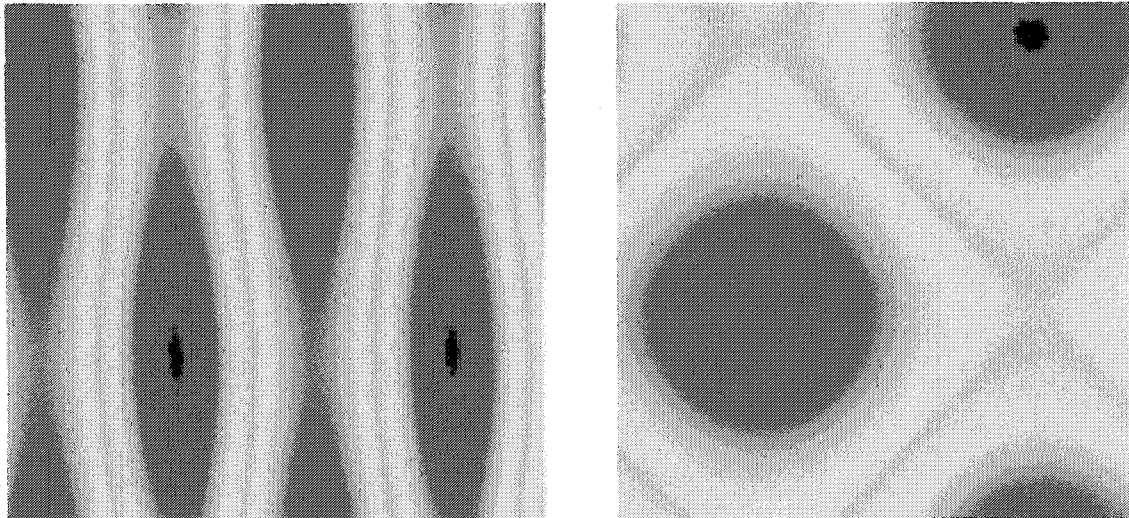


Figure 6.1: *The initial current(left) and vorticity(right) for the Orszag-Tang vortex.*

velocity field profile is

$$\mathbf{v}(x, y) = \mathbf{v}_0[\sin(y + a_1)\hat{i} + \sin(x + a_2)\hat{j}] \quad (6.6)$$

and the initial magnetic field profile is

$$\mathbf{B}(x, y) = \mathbf{B}_0[\sin(y + a_3)\hat{i} + \sin(2x + a_4)\hat{j}] \quad (6.7)$$

where the phase shifts a_n are set arbitrarily. The divergence of both of the initial fields is zero. The curl of the two dimensional momentum density and magnetic fields, which lie in the x-y plane, produce the vorticity and current respectively. These fields are useful as output parameters because they have components, which lie only in the z direction. This aids the visualization of our data considerably as most of the interesting evolution can be viewed with plots of the (essentially scalar)

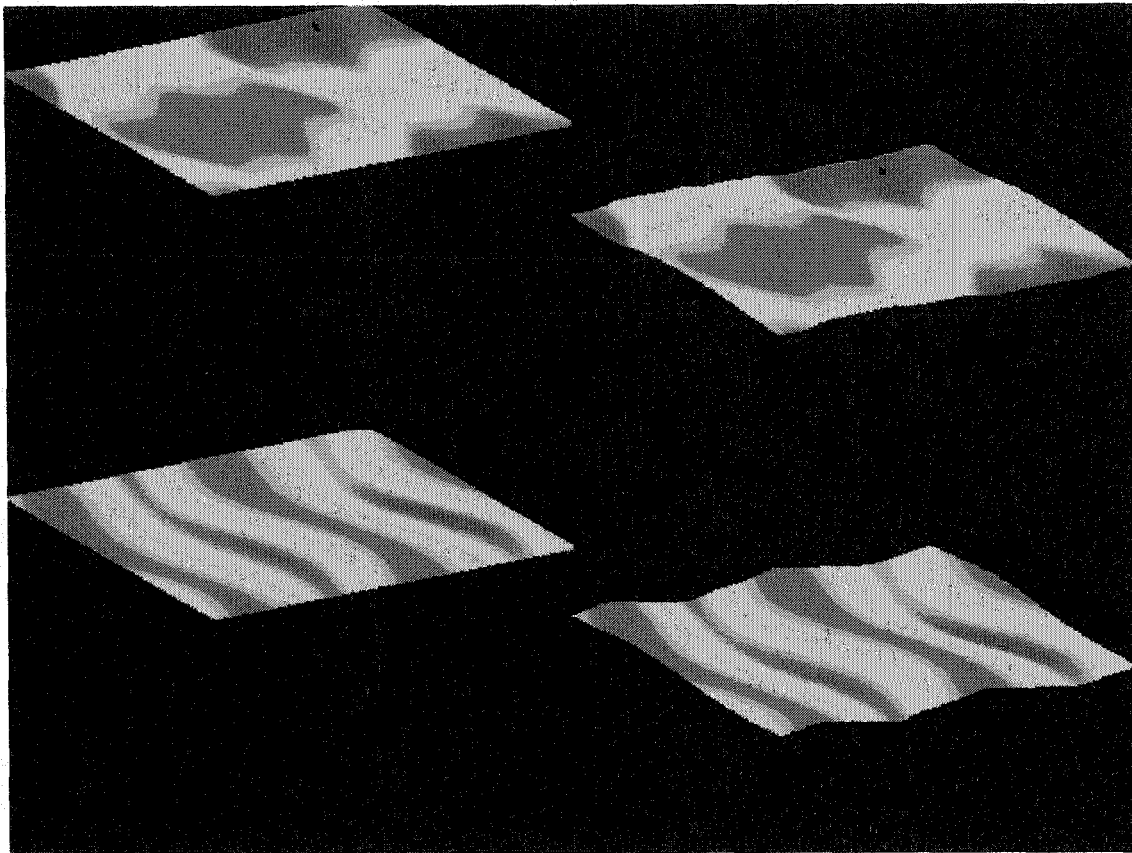


Figure 6.2: *Two dimensional projection and three dimensional surface plots of the vorticity (top) and current (bottom) profiles after 400 LBM time steps. The feedback between the velocity and magnetic fields have begun to alter the initial shapes.*

vorticity and current in the x-y plane. The initial vorticity is thus

$$\boldsymbol{\omega} = \nabla \times \mathbf{v} = v_0(\cos(x + a_2) - \cos(y + a_1))\hat{\mathbf{k}} \quad (6.8)$$

and the initial current is

$$\mathbf{J} = \nabla \times \mathbf{B} = B_0(2 \cos(2x + a_4) - \cos(y + a_3))\hat{\mathbf{k}} \quad (6.9)$$

The current and vorticity fields are shown in Fig. (6.1) for $a_1 = .5$, $a_2 = 1.4$,

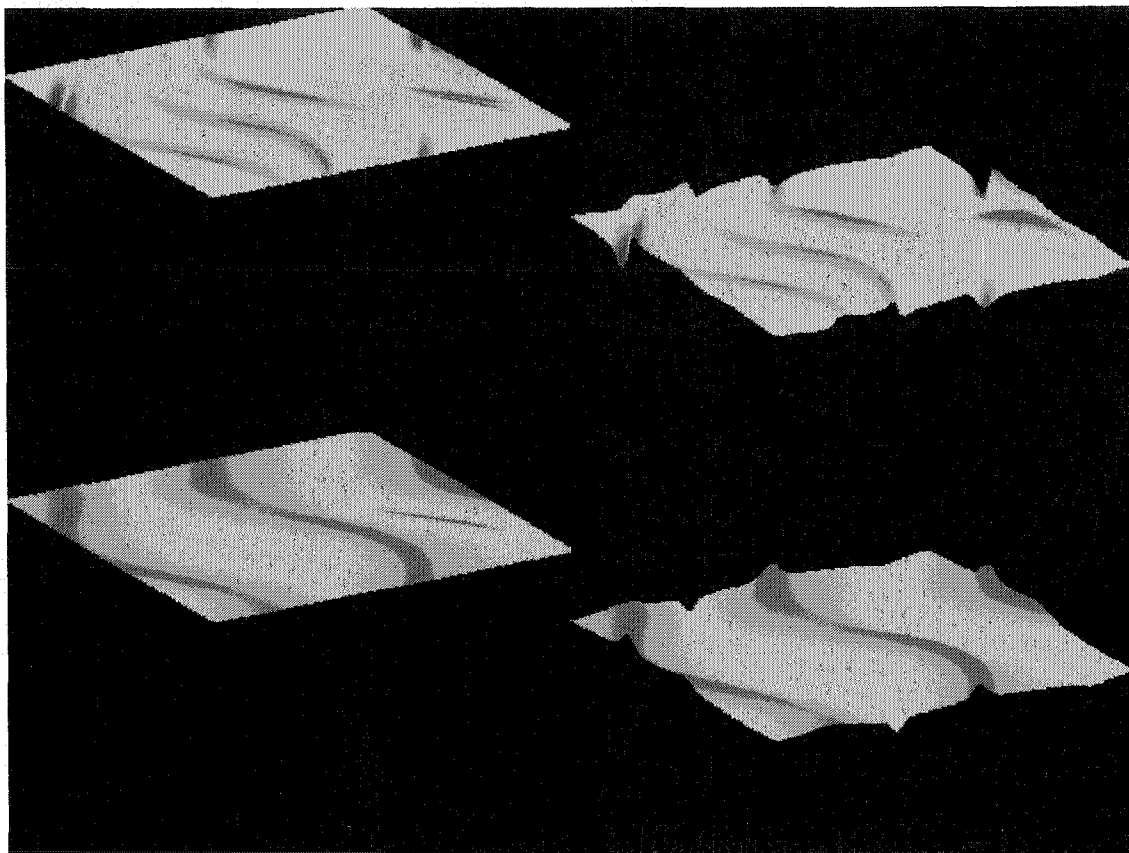


Figure 6.3: *The vorticity (top) and current (bottom) profiles after 800 LBM time steps. Both profiles have begun to decay into thin current and vorticity sheets where the majority of the energy is concentrated.*

$a_3 = 4.1$ and $a_4 = 2.3$. The two large varying layers present in the current profile move into and out of the page while the two large vorticity regions rotate in opposite directions.

For our first simulation of the Orszag-Tang vortex the initial velocity and magnetic fields were set to $v_0 = B_0 = .05$. The relaxation parameters were set to $\tau_\nu = \tau_\mu = 1$ and the free magnetic parameter was set to $\alpha = .5$. A spatial grid containing 512 nodes in the “x” and “y” directions was used. This gives an initial Reynolds and magnetic Reynolds number of $Re = Rm = 204.8$.

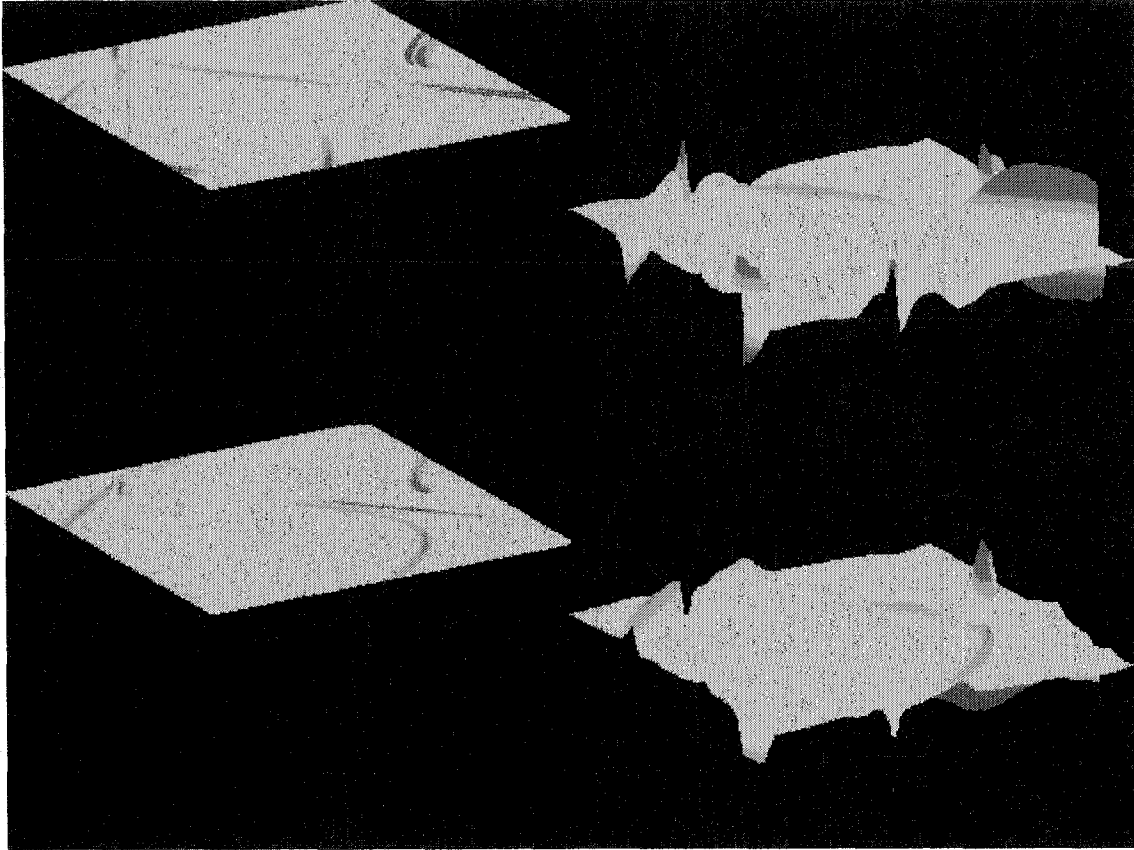


Figure 6.4: *The vorticity (top) and current (bottom) profiles after 1600 LBM time steps. The current and vorticity sheets are have thinned and increased in magnitude.*

Figure (6.2) shows the field profile after 400 LBM time steps. A plot of the two dimensional projection of the three dimensional surface of the vorticity appears in the top left region and a three dimensional surface plot of the vorticity appears in the top right. Two dimensional projection and three dimensional surface plots of the current appear in the bottom left and bottom right, respectively. The vorticity regions have begun to impose a rotational effect on the current sheets, which is especially apparent in the regions where the oppositely rotating vorticity regions meet. Here, the current sheets are beginning to tear apart. The current sheets have also distorted the vorticity structures as is evident in the sheet like sub-structures

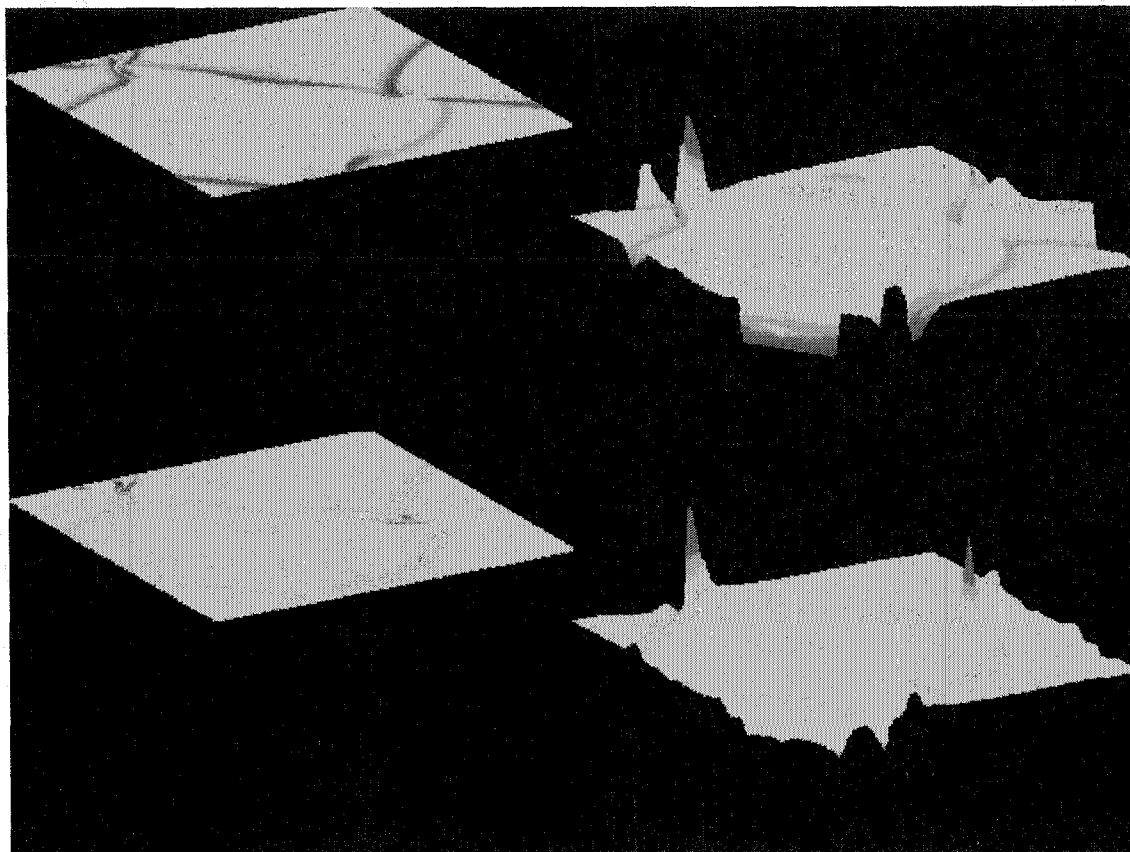


Figure 6.5: *The vorticity (top) and current (bottom) profiles after 3000 LBM time steps. The current and vorticity sheets continue to increase in amplitude.*

contained in each vorticity region.

The field profiles after 800 LBM time steps are shown in Fig. (6.3). The initially large current and vorticity profiles have begun to decay into thin current and vorticity sheets. These thin sheets contain the majority of the magnetic and kinetic energy of the profile.

Figure (6.4) shows the field profiles after 1600 LBM time steps. The current and vorticity sheets have become thinner but have increased in magnitude. The positive and negative current sheets on the right side have collided and torn apart such that they no longer span the entire periodic domain in the “y” direction. The

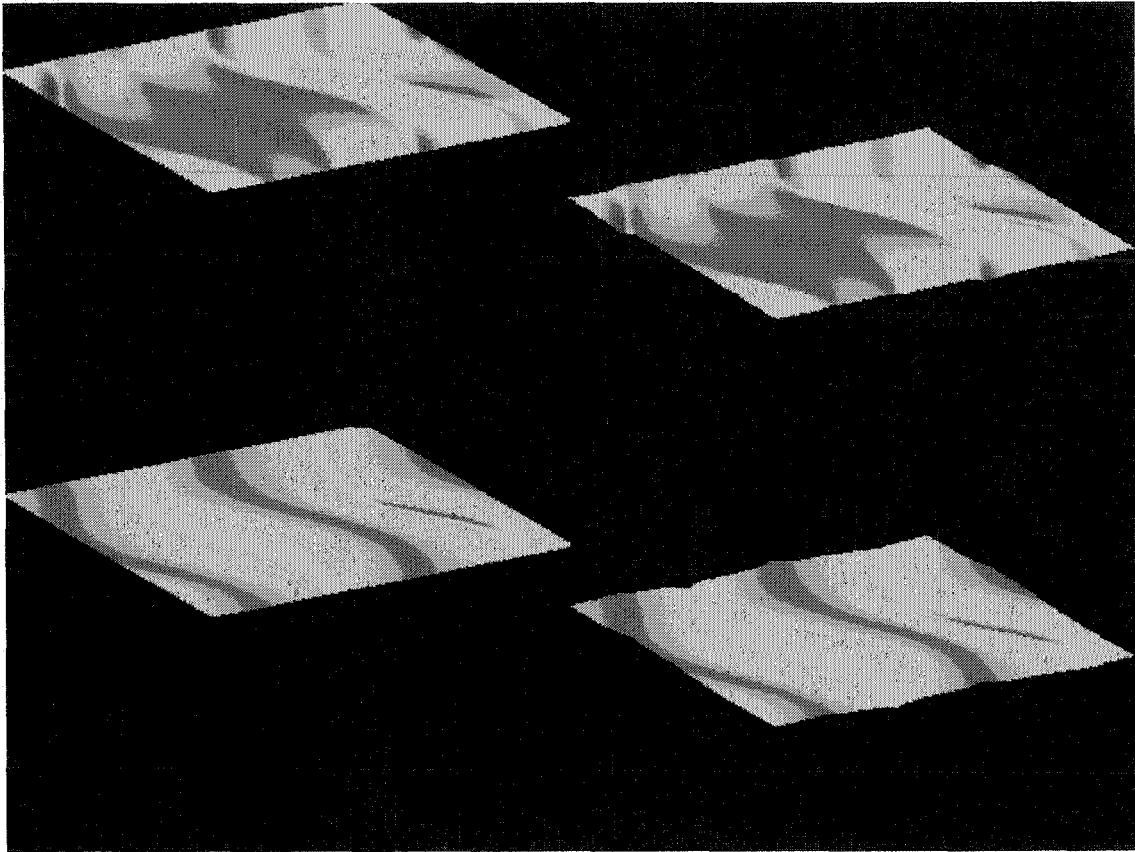


Figure 6.6: *The vorticity (top) and current (bottom) profiles after 600 LBM time steps. The current and vorticity have begun to interact with one another.*

viscosity and resistivity terms in the momentum density and magnetic induction equations have begun to globally dissipate energy. This is evident in the global change in background intensity of both the vorticity and current.

Finally, Fig. (6.5) shows the field profiles after 3000 LBM time steps. The current and vorticity sheets have grown in magnitude. A comparison of the current and vorticity profiles reveals that the sharpest current sheets appear in regions where positive and negative vorticity sheets have merged. This is particularly apparent in the upper left and lower right corners of the profile.

It is now worthwhile to examine a simulation, which uses larger values for the

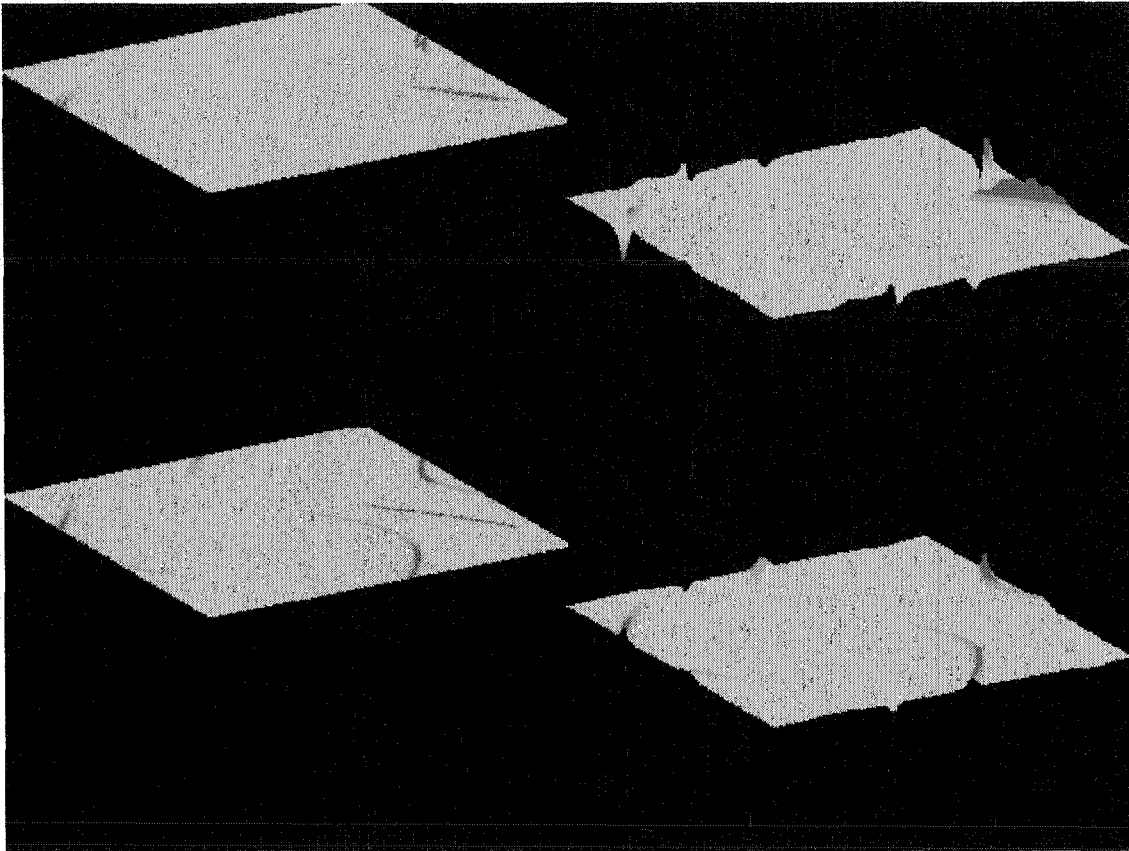


Figure 6.7: *The vorticity (top) and current (bottom) profiles after 1000 LBM time steps. The large scale initial fields have decayed to form thin sheets.*

Reynolds and magnetic Reynolds numbers but, uses a similar set of initial conditions. For this simulation we also use a grid with 512 nodes in the “x” and “y” directions and we set the initial fields to $v_0 = B_0 = .05$. However, the relaxation constants were set to $\tau_\nu = \tau_\mu = .788675$ to give an initial Reynolds and magnetic Reynolds number of $Re = Rm = 354.72$. The increase in these values should encourage a more turbulent evolution of the system.

Figure (6.6) shows the profile of the current and vorticity fields after 600 LBM time steps. The current has begun to impose a sheet like structure within the regions of large vorticity. The vorticity has also begun to rotate and tear the current sheets.

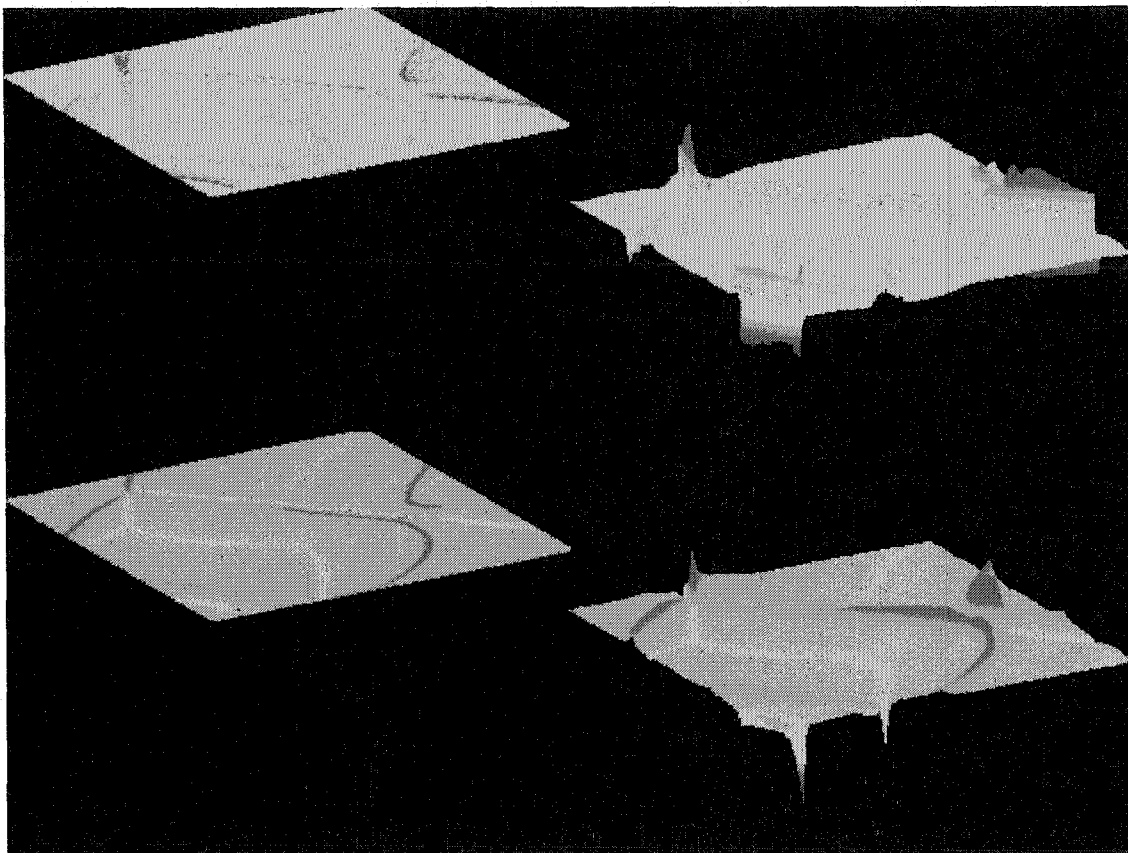


Figure 6.8: *The vorticity (top) and current (bottom) profiles after 2000 LBM time steps. A number of wispy filaments of current and vorticity have developed.*

The profile of the current and vorticity after 1000 LBM time steps is plotted in Fig. (6.7). The large scale initial conditions have decayed to form thin sheets of current and vorticity. Because of the large Reynolds and magnetic Reynolds numbers, these sheets are localized to thinner regions of space than the previous simulation. Figure (6.8) shows the current and vorticity profiles after 2000 LBM time steps. This turbulent profile contains a number of wispy current filaments. As was explained previously, the regions where positive and negative vorticity sheets converge correspond to high intensity current sheets. The field profiles after 3000 LBM time steps are shown in Fig. (6.9). This plot particularly illustrates the

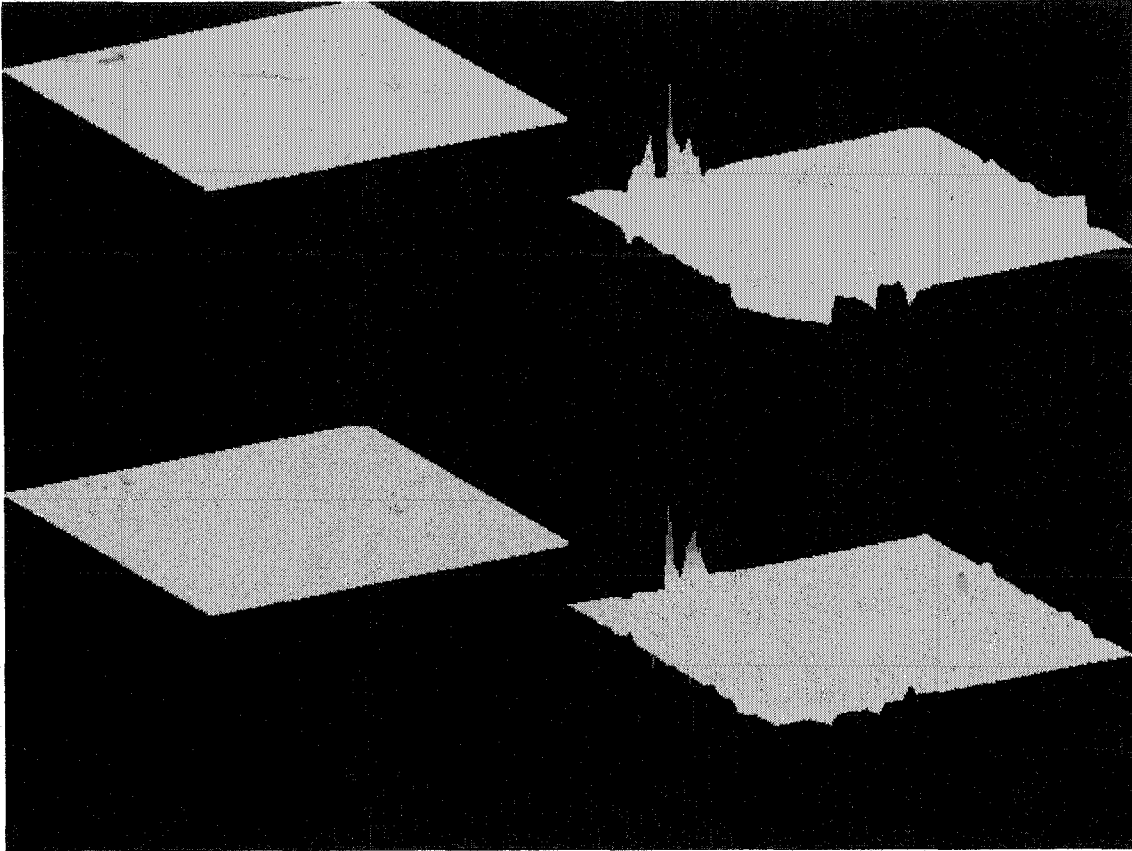


Figure 6.9: *The vorticity (top) and current (bottom) profiles after 3000 LBM time steps. The lower viscosity and resistivity results in a more turbulent profile.*

effect of large Reynolds and magnetic Reynolds numbers in the sporadic intensity of the current sheets along their length wise direction. As we would expect, the low viscosity and resistivity terms result in smaller scale turbulent structures in the overall evolution of our field profiles.

6.3 Modified Orszag-Tang Vortex

We will now look at a slightly modified version of the Orszag-Tang vortex. For this simulation we increase the wavenumber of the “y” component of the magnetic

field by a factor of two in order to create more current sheets. This change is made in order to increase the number of dynamically coalescing and reconnecting magnetic field lines. The initial velocity field remains the same as in our previous simulations

$$\mathbf{v}(x, y) = \mathbf{v}_0[\sin(y + .5)\hat{i} + \sin(x + 1.4)\hat{j}] \quad (6.10)$$

and the initial magnetic field profile becomes

$$\mathbf{B}(x, y) = \mathbf{B}_0[\sin(y + 4.1)\hat{i} + \sin(4x + 2.3)\hat{j}]. \quad (6.11)$$

For this simulation we use an array containing 512 grid points in both the “x” and “y” directions and the initial fields are set to $v_0 = B_0 = .05$. The relaxation parameters were set to $\tau_\nu = \tau_\mu = .9$ and the free resistivity parameter was set to $\alpha = .5$ to give Reynolds and magnetic Reynolds numbers of $Re = Rm = 256$. The initial profile of the vorticity and current is shown in Fig. (6.10). The current profile now contains eight varying current sheets and the vorticity profile remains unchanged.

The current and vorticity fields after 600 LBM time steps are plotted in Fig. (6.11). The two large vorticity regions have begun to rotate and tear the current sheets which have thinned and gained in intensity. The sheet like structures that the current layers have imposed on the large initial vorticity regions indicate the interaction between the velocity and magnetic fields. Figure (6.12) shows the current and vorticity profiles after 1200 LBM time steps. Several high intensity current sheets have formed in the regions where positive and negative vorticity sheets have coalesced. On the left side of the vorticity profile two sets of vorticity sheets have

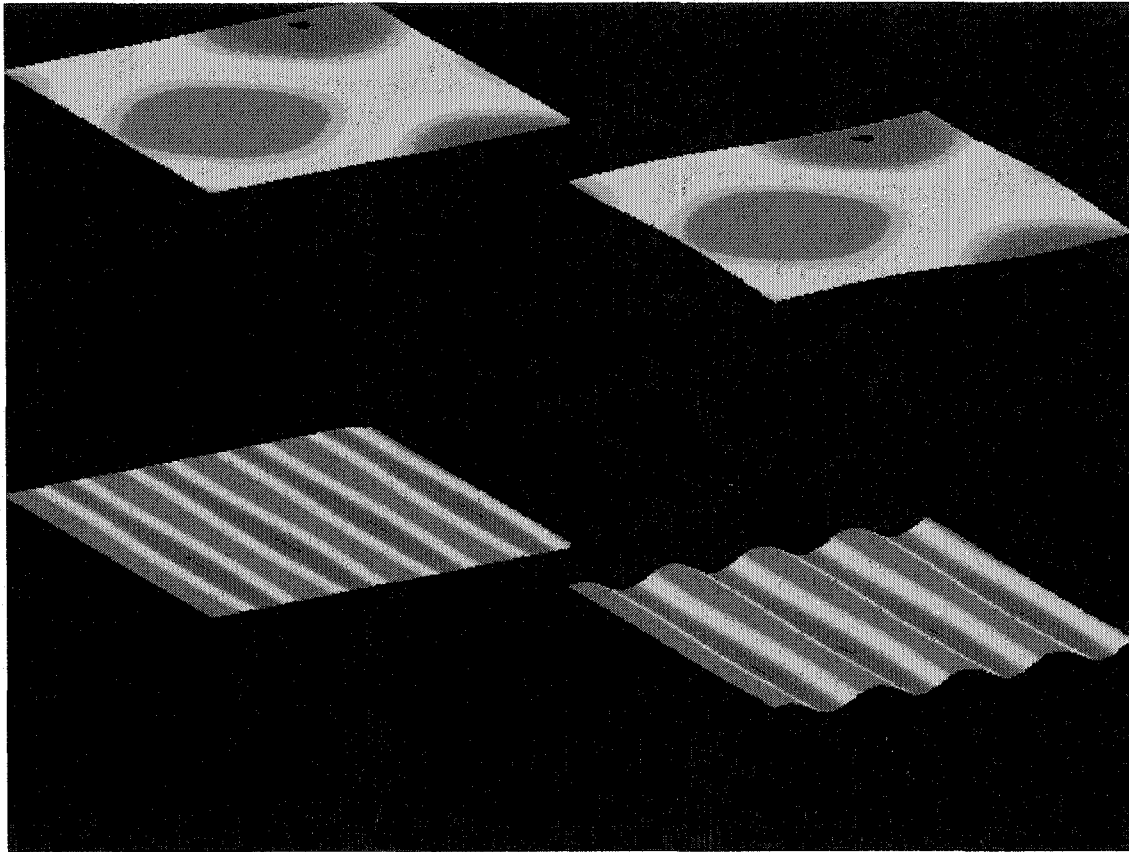


Figure 6.10: *The initial vorticity (top) and current (bottom) profiles of the modified Orszag-Tang vortex. The number of current sheets, which dominate the evolution have increased by a factor of two.*

merged to form forked vorticity layers. The current and vorticity profiles after 2000 LBM time steps is shown in Fig. (6.13). The current contains similar forked layers where current sheets have merged. Two vorticity sheets rotating in opposite directions are still evident in the upper left region of the graph. This region corresponds to an intense current sheet.

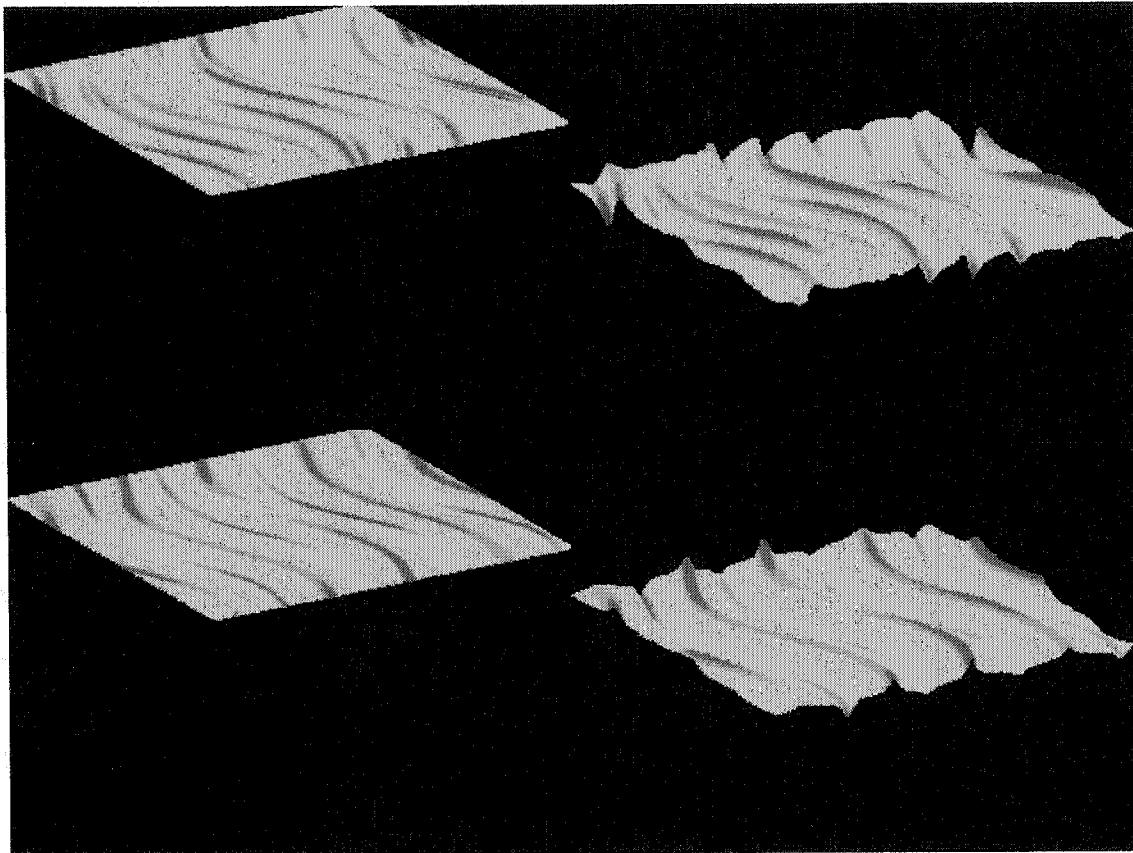


Figure 6.11: *The vorticity (top) and current (bottom) profiles after 600 LBM time steps.*

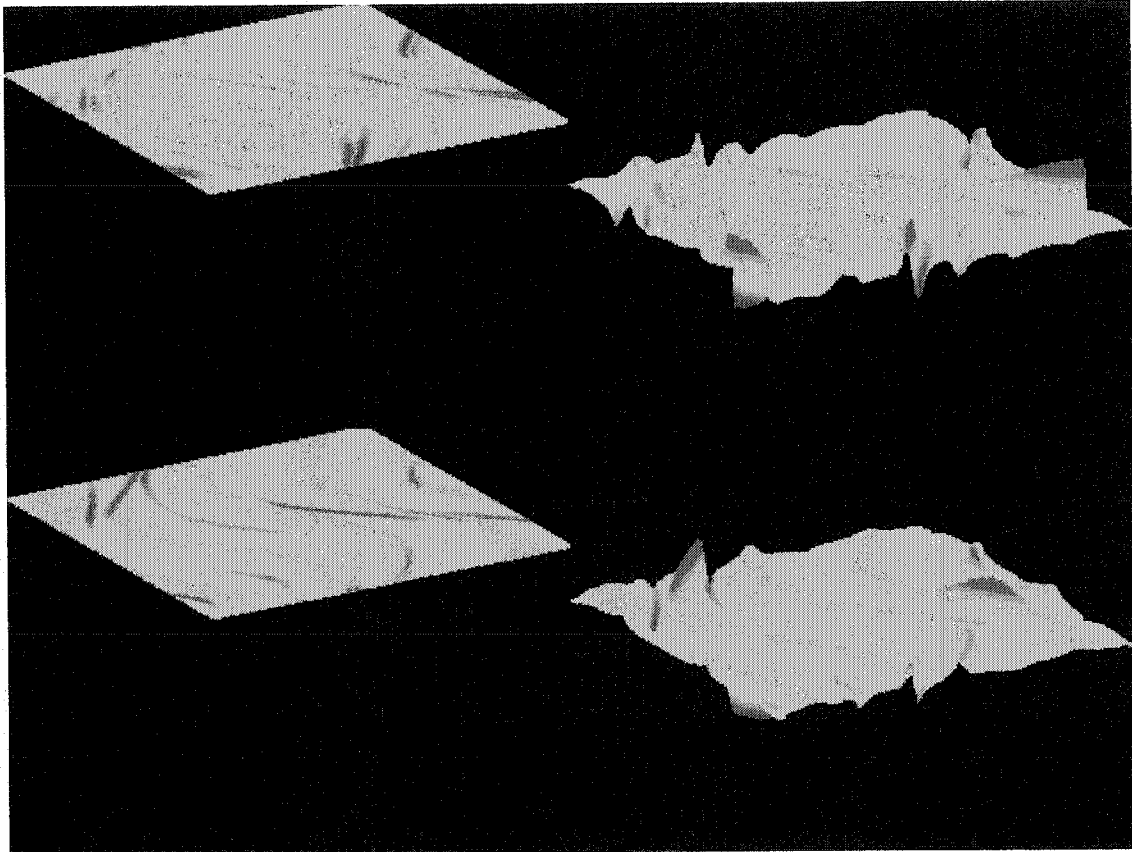


Figure 6.12: *The vorticity (top) and current (bottom) profiles after 1200 LBM time steps.*

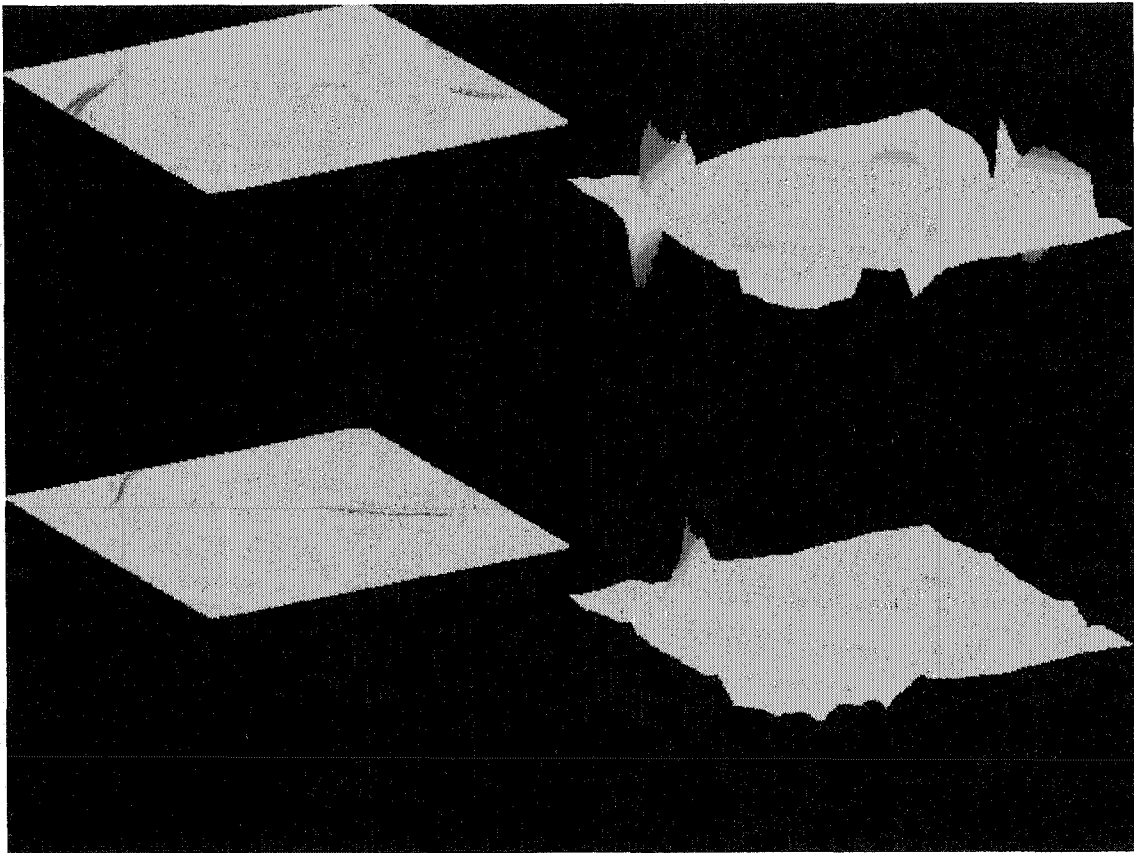


Figure 6.13: *The vorticity (top) and current (bottom) profiles after 2000 LBM time steps.*

CHAPTER 7

Non-Uniform Grid Lattice

Boltzmann Models

7.1 The Need for Non-Uniform Grid Lattice

Boltzmann Models

The desire to implement spatial grids which contain a non-uniform density of lattice nodes originates from the desire to model large scale phenomena without losing resolution in a particular region of interest. This region of interest could contain, for instance, a velocity shock or a very thin current sheet where most of the energy of the large scale structure is located. The incorporation of non-uniform spatial grids thus allows the computational physicist to focus her attention around this region while also resolving the surrounding larger scale structures. In the large scale, these structures can be viewed as discontinuities, which are not able to be effectively treated at that scale. The process of refining the grid in the region around this local discontinuity then allows for effective treatment of the structure



Figure 7.1: *This pictorial representation of a one dimensional non-uniform grid contains a refined region where the coarse grid is split into four spatial sub-steps. This refined region would normally be placed around a region of space where large gradients in the field exist.*

such that it is no longer discontinuous in the fine scale. Figure (7.1) shows a one dimensional non-uniform grid with four refined spatial steps nested in between the coarse grid.

I will illustrate the need for this refinement process with a lattice Boltzmann model of the one dimensional Burger's equation. Burger's equation is of interest because it is the one dimensional incompressible analogue to the viscous Navier Stokes momentum equation and displays most of the notable features of hydrodynamic turbulence. Incompressibility requires that the gradient of the density and pressure in Eq. (1.5) be set to zero. We must require, however, that the velocity field still contain a diverging component. These restrictions essentially void Eq. (1.4). We also make the additional constraint that the density in Eq. (1.5) is constant in time. These constraints gives an equation of the form

$$\rho_0 \partial_t v_i + \rho_0 v_j \partial_j v_i = \nu \rho_0 \partial_j^2 v_i, \quad (7.1)$$

which can immediately be divided by ρ to give

$$\partial_t v_i + \partial_j \left(\frac{1}{2} v_i v_j \right) = \nu \partial_j^2 v_i. \quad (7.2)$$

If we restrict the velocity field to only those components that lie along the "x" axis and allow it only to depend on the position along the "x" axis, then the vector

notation degenerates to

$$\partial_t v(x) + v(x)\partial_x v(x) = \nu \partial_x^2 v(x) \quad (7.3)$$

and forms the one dimensional Burger's equation.

7.1.1 Derivation of the LBM for Burger's Equation

The LBM for Burger's equation was first created by Yan et al.[28] The simplest version of this model uses two streaming vectors; c_+ and c_- of equal length. We can therefore begin with a general set of distribution functions associated with forward streaming, backward streaming and no streaming (due to the vector of length zero). These general distribution functions, written as expansions of the macroscopic velocity field with arbitrary constants in front of them, take the form

$$f_0^{(eq)} = k_1 v + k_2 v^2 + k_3 v^3 \quad (7.4)$$

$$f_+^{(eq)} = k_4 v + k_5 v^2 + k_6 v^3 \quad (7.5)$$

$$f_-^{(eq)} = k_7 v + k_8 v^2 + k_9 v^3 \quad (7.6)$$

By rewriting Eq. (7.3) as

$$\partial_t v(x) + \partial_x \left[\frac{1}{2} v(x)^2 \right] = \nu \partial_x^2 v(x) \quad (7.7)$$

and keeping Eq. (3.8) from the Chapman Enskog expansion procedure in mind, we enforce the following moments:

$$u = \sum_a f_a^{(eq)} \quad (7.8)$$

$$\frac{1}{2}u^2 = \sum_a f_a^{(eq)} c_a \quad (7.9)$$

$$\frac{1}{3}u^3 + \lambda u = \sum_a f_a^{(eq)} c_a^2 \quad (7.10)$$

where λ is an arbitrary constant that will appear in the viscosity term. The enforcement of Eq. (7.8) specifies

$$k_1 + k_4 + k_7 = 1, \quad (7.11)$$

$$k_2 + k_5 + k_8 = 0, \quad (7.12)$$

$$k_3 + k_6 + k_9 = 0. \quad (7.13)$$

The enforcement of Eq. (7.9) specifies

$$k_4 - k_7 = 0, \quad (7.14)$$

$$k_5 - k_8 = \frac{1}{2|c|}, \quad (7.15)$$

$$k_6 - k_9 = 0. \quad (7.16)$$

The enforcement of Eq. (7.10) specifies

$$k_4 + k_7 = \frac{\lambda}{c^2}, \quad (7.17)$$

$$k_5 + k_8 = 0, \quad (7.18)$$

$$k_6 + k_9 = \frac{1}{3c^2}. \quad (7.19)$$

Solving Eqs. (7.11)-(7.19) for the constants k_1 - k_9 gives

$$\begin{array}{lll} k_1 = 1 & k_2 = -\frac{\lambda}{c^2} & k_3 = \frac{-1}{3c^2} \\ k_4 = \frac{\lambda}{2c^2} & k_5 = \frac{1}{4c} & k_6 = \frac{1}{6c^2} \\ k_7 = \frac{\lambda}{2c^2} & k_8 = -\frac{1}{4c} & k_9 = \frac{1}{6c^2} \end{array}$$

and the general distribution functions defined in Eqs. (7.4)-(7.6) become

$$f_0^{(eq)} = v - \frac{\lambda v}{c^2} - \frac{v^3}{3c^2} \quad (7.20)$$

$$f_+^{(eq)} = \frac{\lambda v}{2c^2} + \frac{v^2}{4c} + \frac{v^3}{6c^2} \quad (7.21)$$

$$f_-^{(eq)} = \frac{\lambda v}{2c^2} - \frac{v^2}{4c} + \frac{v^3}{6c^2} \quad (7.22)$$

The lattice vectors in Eq. (3.8) can now be moved inside the partial derivatives and summing over “a” produces

$$\partial_{t_0} v + \partial_x \left(\frac{1}{2} v^2 \right) = 0, \quad (7.23)$$

which constitutes Burger’s equation at the zeroth time scale. We can also perform a similar process on Eq. (3.12) to recover

$$\partial_{t_1} v - \left(\tau - \frac{1}{2} \right) \left[\partial_{t_0}^2 v + 2\partial_{t_0} \partial_x \left(\frac{1}{2} v^2 \right) + \partial_x^2 \left(\lambda v + \frac{v^3}{3} \right) \right] = 0. \quad (7.24)$$

Equation (7.23) can be used to cancel the second and part of the third term in Eq. (7.24) to give

$$\partial_{t_1} v - \left(\tau - \frac{1}{2} \right) \left[\partial_{t_0} \partial_x \left(\frac{1}{2} v^2 \right) + \partial_x^2 \left(\lambda v + \frac{v^3}{3} \right) \right] = 0 \quad (7.25)$$

and employing the chain rule on the last term produces

$$\partial_{t_1} v - \left(\tau - \frac{1}{2} \right) \left[\partial_x v \partial_{t_0} v + \lambda \partial_x^2 v + \partial_x v^2 \partial_x v \right] = 0. \quad (7.26)$$

Equation (7.23) can again be used to exchange the temporal derivative in the first term for the spatial derivative term and Eq. (7.26) becomes

$$\partial_{t_1} v - \left(\tau - \frac{1}{2} \right) \left[-\partial_x v \partial_x \left(\frac{1}{2} v^2 \right) + \lambda \partial_x^2 v + \partial_x v^2 \partial_x v \right] = 0 \quad (7.27)$$

and the first and third terms immediately cancel to give

$$\partial_{t_1} v = \nu \partial_x^2 v. \quad (7.28)$$

where the viscosity is defined as

$$\nu \equiv \lambda \left(\tau - \frac{1}{2} \right). \quad (7.29)$$

As is expected, this transport order evolution equation introduces the dissipative term, which originates from particle collisions. Finally, Eqs. (7.23) and (7.28) can be added to produce Eq. (7.3); the complete Burger's equation with spurious terms due only to the higher order time scale evolution.

7.1.2 Uniform Grid Simulation of Burger's Equation

The simplest non-trivial initial condition one can impose on the velocity profile consists of a sinusoidal wave that spans the entire periodic domain

$$v(x, t_0) = \sin\left(2\pi \frac{x_i}{xsize}\right) \quad i = 0, 1, 2, \dots, xsize - 1 \quad (7.30)$$

where “*xsize*” is the total number of grid points and x_i is a discrete point positioned along the “*x*” axis. As the positive part of the sine wave propagates to the right and the negative part propagates to the left the region of negative slope steepens to form a shock in the middle of the profile. Figure (7.2) shows the initial velocity profile and the subsequent profiles after 1000 and 3000 LBM time steps. The parameters for this simulation are $v_0 = 1$, $\tau = .5375$, and $\lambda = \frac{25}{3}$. This gives a viscosity of $\nu = .1172$ and a dimensionless Reynolds number of $Re = 5120$. Because only

LBM Simulation of Burger's Equation

$v(x)$ vs. x on a uniform grid with 600 nodes

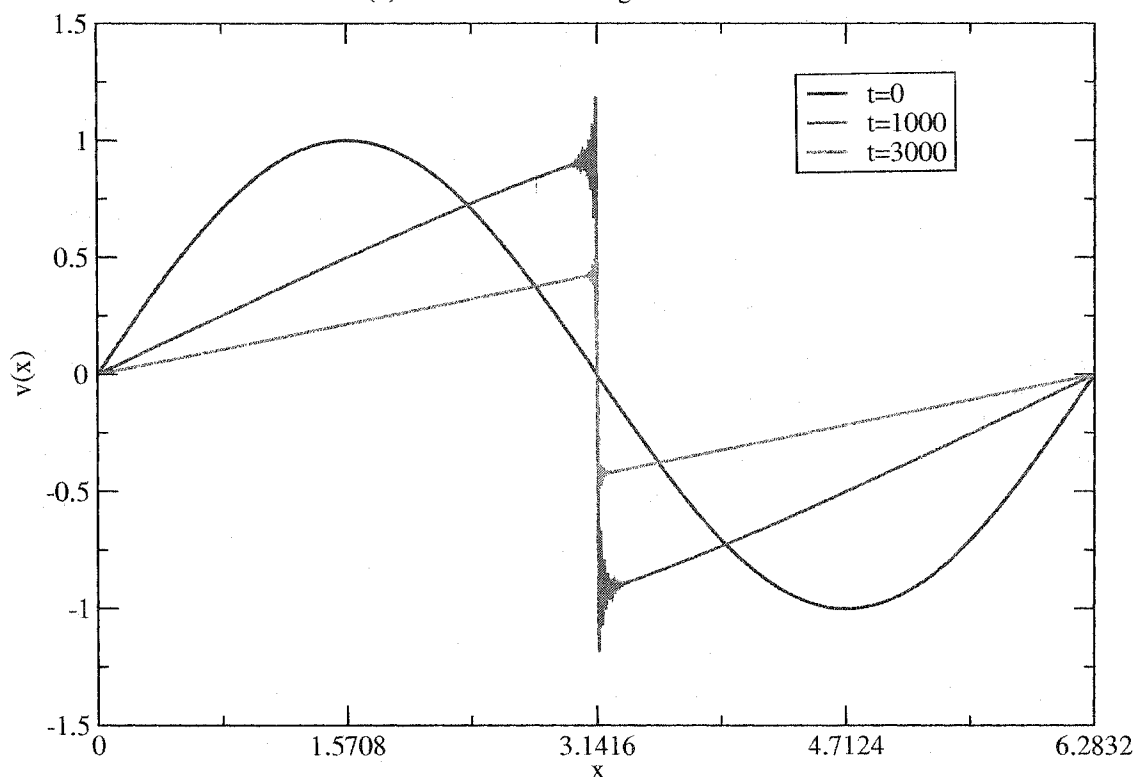


Figure 7.2: As the shock front steepens, numerical oscillations adjacent to the shock are apparent.

600 grid points are used, the profile develops numerical oscillations in the region adjacent to the shock. This is a common error seen in all finite difference modeling schemes and can only be resolved by introducing numerical diffusion, lowering the Reynolds number or by running the simulation on a finer spatial grid. As we wish to investigate phenomena that occurs for large values of the Reynolds number, the first two choices are undesirable. We therefore need to refine the grid in order to eliminate the numerical oscillations. Figure (7.3) shows the simulation performed with the same Reynolds number, but with 4800 grid points. The parameters for this simulation are $v_0 = 1$, $\tau = .8$, and $\lambda = \frac{25}{3}$. This gives a viscosity of $\nu = .9375$

LBM Simulation of Burger's Equation

$v(x)$ vs. x on a uniform grid with 4800 nodes

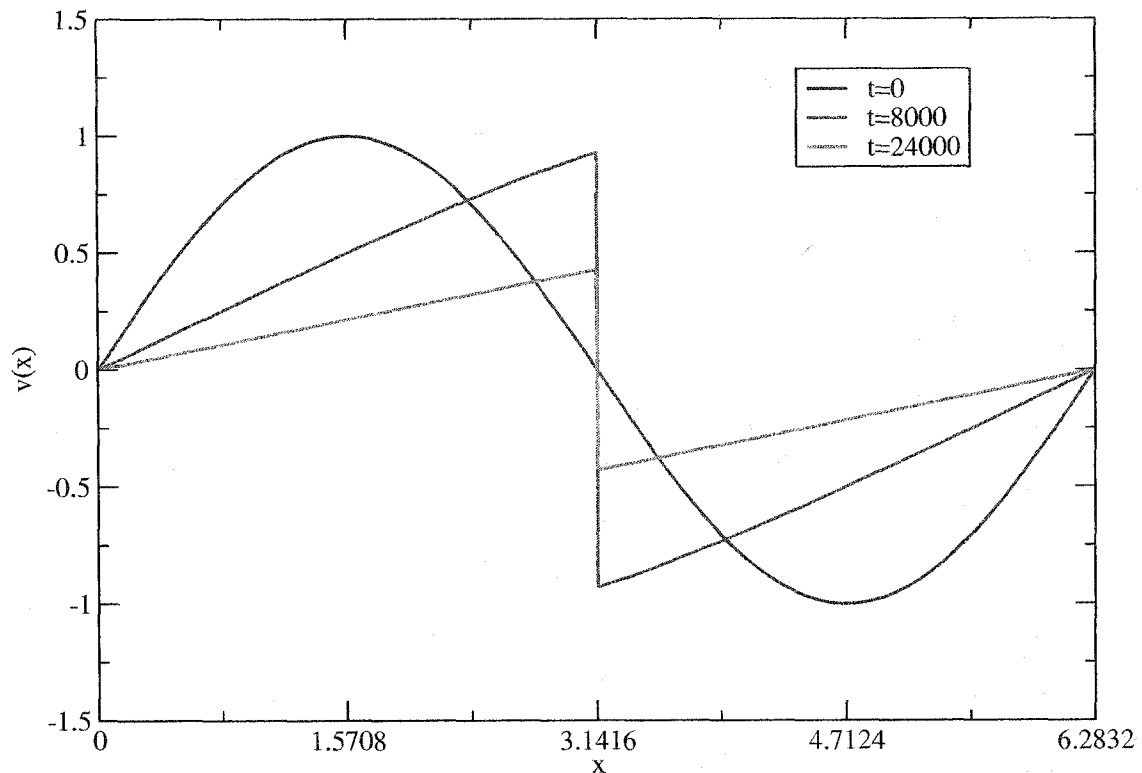


Figure 7.3: *The numerical oscillations are eliminated on a uniform grid by increasing the number of grid points. The viscosity was altered in order to preserve the same Reynolds number so this simulation represents an 64 fold increase in computational expenditure over the 600 grid point simulation.*

and a dimensionless Reynolds number of $Re = 5120$. Eight time steps from this simulation correspond to one time step in the 600 node simulation in Fig. (7.2). The numerical oscillations are clearly no longer visible when we use this level of spatial refinement. A crucial issue in assessing the computational efficiency of this global refinement procedure comes from the inherent link between the LBM time steps and the LBM spatial steps. An increase in the grid size by a factor of eight requires that we decrease the initial velocity by a factor of eight in order to retain the same Reynolds number for a given value of viscosity. The LBM time steps

are thus decreased by a factor of 64 and the grid load has increased by a factor of eight. This translates to a 512 fold total increase in the computational effort. In general, this process of increasing the grid size by some factor “ w ” without altering the viscosity increases the computational effort by w^3 . In cases requiring a lot of refinement we may therefore choose to alter the value for the viscosity along with the grid size. If the grid size and the viscosity are the only parameters that are altered, the computational effort will only scale like w^2 as the time steps still decrease by a factor of eight. One drawback in this obvious choice comes from the numerical stability constraints imposed on τ , which must typically be set to a value between one half and one.

Rather than refining the spatial grid globally over the entire spatial profile, refinement in a specific region involves only a small fraction of the computational increase of either of the methods presented above. In the 600 node simulation in Fig. (7.2), for instance, the 100 grid points in the region containing the shock can be refined by a factor of eight to give a total increase in computational effort of $w = 64 \cdot \frac{100}{600} = 10.67$. In comparison to the 512 and 64 fold increase presented in the previous paragraph, this represents a significant improvement in the computational expenditure. We will therefore present the derivations of two methods for accomplishing this non-uniform refinement in sections 7.2 and 7.3.

7.2 Unmatched Node Non-Uniform Grid

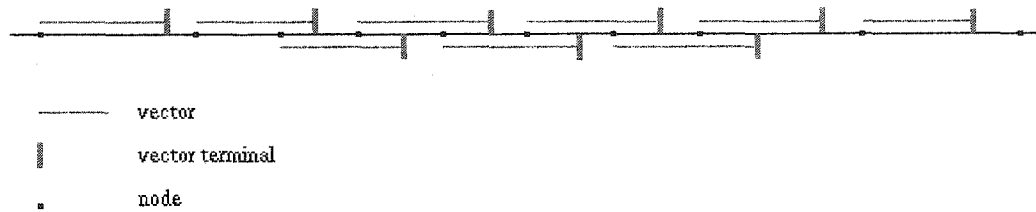


Figure 7.4: To prevent a decoupling of the coarse and fine grids, we use vectors that do not terminate at any of the nodes. 3rd order interpolation is used to connect the nodes with the vector terminals.

LBM

7.2.1 Development of the Unmatched Node Model

In developing a non-uniform grid LBM we first chose to draw from our experience with the octagonal lattice and apply it to the one dimensional model. In the octagonal LBM, the issue of the streaming vectors not terminating at the sites of nodes of the distribution functions was viewed as a decoupling of the velocity space streaming lattice and the Cartesian distribution function lattice. A similar decoupling can occur in one dimensional streaming if we refine the spatial lattice in a given region. A coupled model would refine the length of the streaming vectors so that the spatial step divided by the time step gives the vector length $c_a = \frac{\Delta x}{\Delta t}$, where Δx is the distance between lattice nodes. If however, the streaming lattice is decoupled from the spatial lattice we can define the streaming vectors as functions of an independent spatial step that will be denoted by δx . Hence the streaming

vector is written as

$$c_u = \frac{\delta x}{\Delta t} \neq \frac{\Delta x}{\Delta t}. \quad (7.31)$$

We are now free to create a spatial lattice with any type of variation in the density of grid points across the spatial regime. Continuing with the simulation of Burger's equation from section 7.1.2, we define a region around the shock, which has a spatial refinement factor of $\frac{\Delta x}{\Delta x_f} = 2$, where Δx_f is the spatial step between nodes on the refined grid. This means that the region adjacent to the shock contains twice the density of grid points. Additionally, we define the streaming length to be $\frac{3}{4}\delta x = \Delta x$. Figure (7.4) shows a depiction of this spatial grid and the streaming vectors in the region of refinement. Notice that all of the vector terminals sit at points where no spatial nodes exist. This was done so that the nested grid points in the refined region exchange information with the regular grid points. Consider for instance, the effect that a vector with length $2\delta x = \Delta x$ would have on the exchanged information. The nested grid points would only transfer streamed information to other nested grid points and the coarse grid points would only transfer information to other coarse grid points.

This unmatched node method requires the use of an interpolation procedure at every spatial location to connect the streaming vector terminals to the spatial nodes. We use a third order Lagrange interpolation similar to the second order Lagrange interpolation outlined in section 5.1. The difference is that we now use four grid points in the interpolation procedure to achieve third order accuracy. Because Eqs. (5.15) and (5.16) provide the interpolation polynomials to any order of accuracy, we will not derive the polynomials again here.

Using this methodology, the viscosity is independent of any refinement proce-

ture. We must only alter our definition of the Reynolds number to preserve a self consistent ratio of the dissipative term to the nonlinear terms in Burger's equation. Defining a refinement factor $m \equiv \frac{\Delta x}{\Delta x_f}$, the Reynolds number is

$$Re \equiv \frac{v_0 \cdot (xsize + \frac{xsize_f}{m})}{\nu} \quad (7.32)$$

where “*xsize*” is the number of coarse grid points, “*m*” is the refinement factor, and *xsize_f* is the number of fine grid points. With these definitions in place, the computational process progresses in the manner outlined in Fig (3.1). The only difference lies in the interpolation procedure used in the streaming step.

7.2.2 Testing the Unmatched Node Model with the 1-D Burger's Equation

A good test of the benefits gained by the unmatched node LBM consists of comparing it against a standard LBM for the same number of total grid points. Figure (7.5) shows such a comparison for simulations containing 600 grid points. The standard LBM uniformly distributes the points over the periodic regime while the unmatched procedure places 300 grid points in the inner $\frac{1}{3}$ of the plot and spreads the remaining 300 grid points over the outer regions. The simulation was run for 2000 LBM time steps with an initial velocity of $v_0 = 1$. The relaxation constant was set to $\tau = .52$ and the free parameter was set to $\lambda = \frac{25}{3}$. This gives a viscosity of $\nu = .1667$, and a Reynolds number of $Re = 3600$. The velocity field profile is plotted for $t=0$, $t=1000$, and $t=2000$. The numerical oscillations have clearly decreased in the unmatched node LBM. They also do not span as far of a distance from each side of the shock front. The impressive aspect of this plot comes from the fact that

A Comparison of Uniform and Non-Uniform Grid LBMs

$v(x)$ vs. x , both simulations use 600 grid points

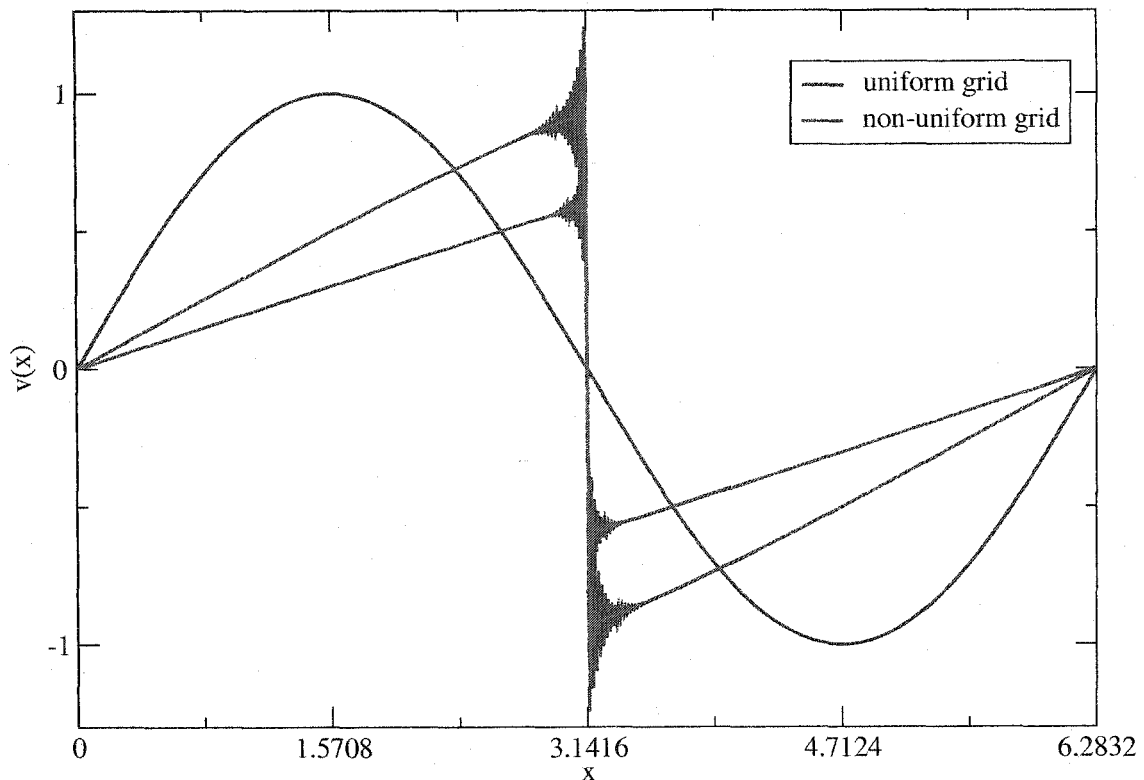


Figure 7.5: A comparison of simulations of Burger's equation for a simple sine function using a uniform (blue) and non-uniform (red) LBM. Both models use 600 grid points, but the non-uniform unmatched node model has the grid points distributed more densely in the region of the shock. The decrease in numerical oscillations is clearly visible.

arrays of the same length were used in each case. Figure (7.6) shows the region adjacent to the upper left half of the shock front in greater detail. Only the $t=1000$ and $t=2000$ velocity profiles are shown in this high resolution view.

One difficulty in this unmatched node LBM comes from the interpolation procedure and its static nature. In order to achieve higher levels of refinement in the non-uniform grid, one needs to calculate new interpolating polynomials to connect the streaming vectors to the nodes. For this reason, we decided it would be pru-

A Comparison of Uniform and Non-Uniform Grid LBMs

$v(x)$ vs. x , both simulations use 600 grid points

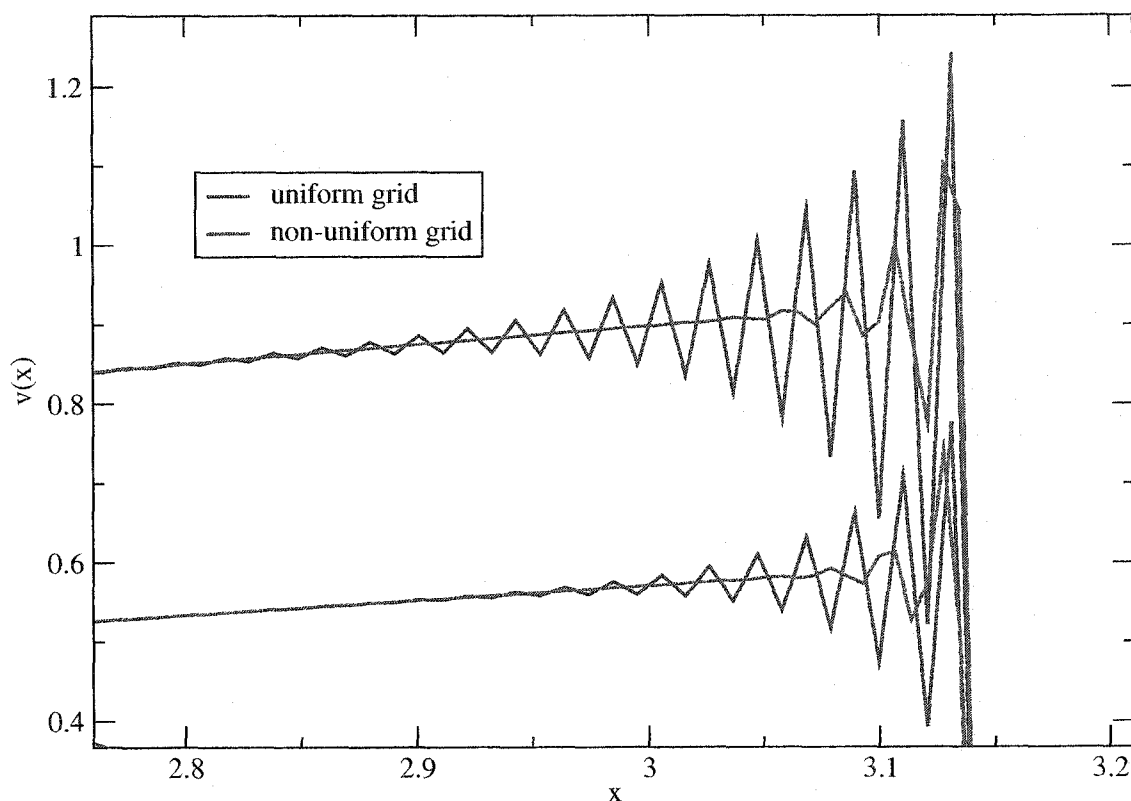


Figure 7.6: A zoomed in view of the plot in Fig. (7.5) in the region of the upper left shock front. The oscillations are not as large or as pervasive in the non-uniform unmatched node LBM.

dent to investigate an alternative approach to non-uniform LBMs. This alternative approach is presented in section 7.3.

7.3 Non-Uniform Grid LBM Using Coupled

Streaming and Spatial Lattices

7.3.1 Developing the Coupled Lattice Model

Another method for non-uniformly refining the grid involves preserving the coupling between the streaming vectors and the spatial grid. The method was initially presented by Filippova et al.[12, 13] and was derived in detail by Yu et al. [30]. It will allow us to designate a refinement factor, which can easily be altered to preserve small gradients of the fields (relative to the grid density) across regions containing strong shocks. The refinement factor is given by

$$m \equiv \frac{\Delta x_c}{\Delta x_f} \quad (7.33)$$

where Δx_c is the spatial step in the coarse grid and Δx_f is the spatial step in the fine grid. Preserving the coupling between the streaming vectors and the spatial lattice requires that the lattice vectors be defined as

$$c_{a,i} \equiv \frac{\Delta x_c}{\Delta t_c} = \frac{\Delta x_f}{\Delta t_f}. \quad (7.34)$$

This necessitates that the time evolution on the fine grid also evolve in fractional increments of the coarse grid time steps. Thus we have a dual definition for the refinement factor

$$m \equiv \frac{\Delta t_c}{\Delta t_f}. \quad (7.35)$$

This refined temporal and spatial stepping requires that the transfer of information between the coarse and fine grids be handled very carefully. In particular,

we begin with the global dimensionless Reynolds number

$$Re = \frac{v_0 \cdot xsize}{\nu_c} \quad (7.36)$$

where the global grid size is defined as $xsize = xsize_c + \frac{xsize_f}{m}$. The local Reynolds number in the coarse regions can then be defined as

$$Re_c = \frac{v_0 \cdot xsize \cdot \Delta x_c}{\nu_c \Delta x_c} \quad (7.37)$$

and the local Reynolds number in the refined regions is defined as

$$Re_f = \frac{v_0 \cdot xsize \cdot \Delta x_c}{\nu_f \Delta x_f}. \quad (7.38)$$

Because these Reynolds numbers must be identical for the same initial fields we define the viscosity in the coarse region as a function of the viscosity in the coarse region. Setting Re_f equal to Re_c and solving for ν_f gives

$$\nu_f = \frac{\Delta x_c}{\Delta x_f} \nu_c = m \nu_c. \quad (7.39)$$

Since a factor of $\tau - \frac{1}{2}$ always appears in the viscosity terms, we can satisfy Eq. (7.39) by defining the relaxation constant in the fine grid as a function of the relaxation constant in the coarse grid

$$\tau_f = \frac{1}{2} + m \left(\tau_c - \frac{1}{2} \right) \quad (7.40)$$

It is useful to include two overlapping points at each interface between the fine and coarse grids so that the fine distribution functions can be correlated to coarse

distribution functions and vice versa. These overlapping points are depicted in Fig (7.1). To proceed with a derivation of the relationship between the coarse and fine grids we need to reconsider the lattice Boltzmann equation

$$f_a(x_i + c_{a,i}\Delta t, t + \Delta t) - f_a(x_i, t) = -\frac{1}{\tau}(f_a - f_a^{(eq)}). \quad (7.41)$$

The second term on the left hand side of Eq. (7.41) can be moved to the right hand side and Eq. (7.41) can be rewritten as

$$f_a(x_i + c_{a,i}\Delta t, t + \Delta t) = f_a(x_i, t) - \frac{1}{\tau}(f_a - f_a^{(eq)}). \quad (7.42)$$

Equation (7.42) can now be split into the collision step

$$\tilde{f}_a(x_i, t) = f_a(x_i, t) - \frac{1}{\tau}(f_a - f_a^{(eq)}), \quad (7.43)$$

and the streaming step

$$f_a(x_i + c_{a,i}\Delta t, t + \Delta t) = \tilde{f}_a(x_i, t), \quad (7.44)$$

where \tilde{f}_a represents the post collision state of the distribution function. We can now write the distribution function as the equilibrium distribution function plus the non-equilibrium parts of the distribution function

$$f_a = f_a^{(eq)} + f_a^{(neq)}. \quad (7.45)$$

Conservation of the zeroth moment of the equilibrium distribution function (whether

this defines the velocity or magnetic field) requires that

$$\sum_a f_a^{(neq)} = 0. \quad (7.46)$$

We can also define the deviatoric stress which, is formed from the first moment of the distribution function. For a vector distribution function this takes the form

$$\left(1 - \frac{1}{2\tau}\right) \sum_a f_a^{(neq)} (c_{a,j} - \frac{1}{2}c_{a,j}\delta_{i,j}) \equiv T_{i,j}, \quad (7.47)$$

and for scalar distribution functions this reduces to

$$\left(1 - \frac{1}{2\tau}\right) \sum_a f_a^{(neq)} \frac{1}{2}c_{a,i} \equiv T_i. \quad (7.48)$$

Equation (7.45) can now be substituted into Eq. (7.43) to give

$$\tilde{f}_a(x_i, t) = \left(1 - \frac{1}{\tau}\right) (f_a^{(eq)}(x_i, t) + f_a^{(neq)}(x_i, t)) + \frac{1}{\tau} f_a^{(eq)}. \quad (7.49)$$

Canceling one of the $f_a^{(eq)}$ terms and multiplying the remaining $f_a^{(neq)}$ terms by $\frac{\tau}{\tau}$ gives

$$\tilde{f}_a(x_i, t) = f_a^{(eq)}(x_i, t) + \frac{\tau - 1}{\tau} f_a^{(neq)}(x_i, t). \quad (7.50)$$

We can now make a distinction between the fine and coarse distribution functions and rewrite Eq. (7.50) for each of the grids

$$\tilde{f}_a^{(c)}(x_i, t) = f_a^{(eq,c)}(x_i, t) + \frac{\tau_c - 1}{\tau_c} f_a^{(neq,c)}(x_i, t), \quad (7.51)$$

$$\tilde{f}_a^{(f)}(x_i, t) = f_a^{(eq,f)}(x_i, t) + \frac{\tau_f - 1}{\tau_f} f_a^{(neq,f)}(x_i, t). \quad (7.52)$$

The zeroth moments of the fine and coarse distribution functions are required to be continuous across the interface between the coarse and fine grids, which specifies

$$f_a^{(eq,c)} = f_a^{(eq,f)}. \quad (7.53)$$

The deviatoric stresses are also required to be continuous across the interface between the coarse and fine grids, $T_{i,j}^c = T_{i,j}^f$. This specifies

$$\left(1 - \frac{1}{2\tau_c}\right) \sum_a f_{a,i}^{(neq,c)} (c_{a,j} - \frac{1}{2} c_{a,j} \delta_{i,j}) = \left(1 - \frac{1}{2\tau_f}\right) \sum_a f_{a,i}^{(neq,f)} (c_{a,j} - \frac{1}{2} c_{a,j} \delta_{i,j}) \quad (7.54)$$

which reduces to

$$\left(1 - \frac{1}{2\tau_c}\right) f_{a,i}^{(neq,c)} = \left(1 - \frac{1}{2\tau_f}\right) f_{a,i}^{(neq,f)}, \quad (7.55)$$

because the streaming vectors on the fine and coarse grids are the same. Solving Eq. (7.54) for $f_{a,i}^{(neq,c)}$

$$f_a^{(neq,c)} = \frac{\tau_f - \frac{1}{2}\tau_c}{\tau_c - \frac{1}{2}\tau_f} f_a^{(neq,f)}, \quad (7.56)$$

and substituting Eq. (7.40) into the first fraction gives

$$f_i^{(neq,c)} = m \frac{\tau_c}{\tau_f} f_a^{(neq,f)}. \quad (7.57)$$

Equations (7.53) and (7.57) can now be used to eliminate the $f_a^{(eq,c)}$ and $f_a^{(neq,c)}$

terms from the right hand side of Eq. (7.51)

$$\tilde{f}_a^{(c)} = f_a^{(eq,f)} + m \frac{\tau_c - 1}{\tau_f} f_a^{(neq,f)}, \quad (7.58)$$

and Eq. (7.52) can finally be used to eliminate $f_a^{(neq,f)}$

$$\tilde{f}_a^{(c)} = f_a^{(eq,f)} + m \frac{\tau_c - 1}{\tau_f - 1} (\tilde{f}_a^{(f)} - f_a^{(eq,f)}). \quad (7.59)$$

Similarly, Eqs. (7.53) and (7.57) can be used to eliminate the $f_a^{(eq)}$ and $f_a^{(neq,f)}$ terms from the right hand side of Eq. (7.52). This gives us

$$\tilde{f}_a^{(f)} = f_a^{(eq,c)} + \frac{\tau_f - 1}{m\tau_c} f_a^{(neq,c)}, \quad (7.60)$$

and using (7.51) to eliminate $f_a^{(neq,c)}$ produces

$$\tilde{f}_a^{(f)} = f_a^{(eq,c)} + \frac{1}{m} \frac{\tau_f - 1}{\tau_c - 1} (\tilde{f}_a^{(c)} - f_a^{(eq,c)}). \quad (7.61)$$

We have now defined all of the equations that govern our computational procedure. Eqs. (7.51) and (7.52) govern the collision step on the fine and coarse grids where as Eqs. (7.59) and (7.61) govern the collision step at the two points at the interface of the fine and coarse boundary. The streaming steps are then given by Eq. (7.44) for both the fine and coarse grids. It is pedagogically useful to show the computational procedure for this new non-uniform grid LBM. Figure (7.7) shows a flow chart of the computational procedure, which is useful to compare against Fig. (3.1). The key difference in the computational procedures lie in the collision steps that occur at the boundary interfaces and in the fractional time stepping that

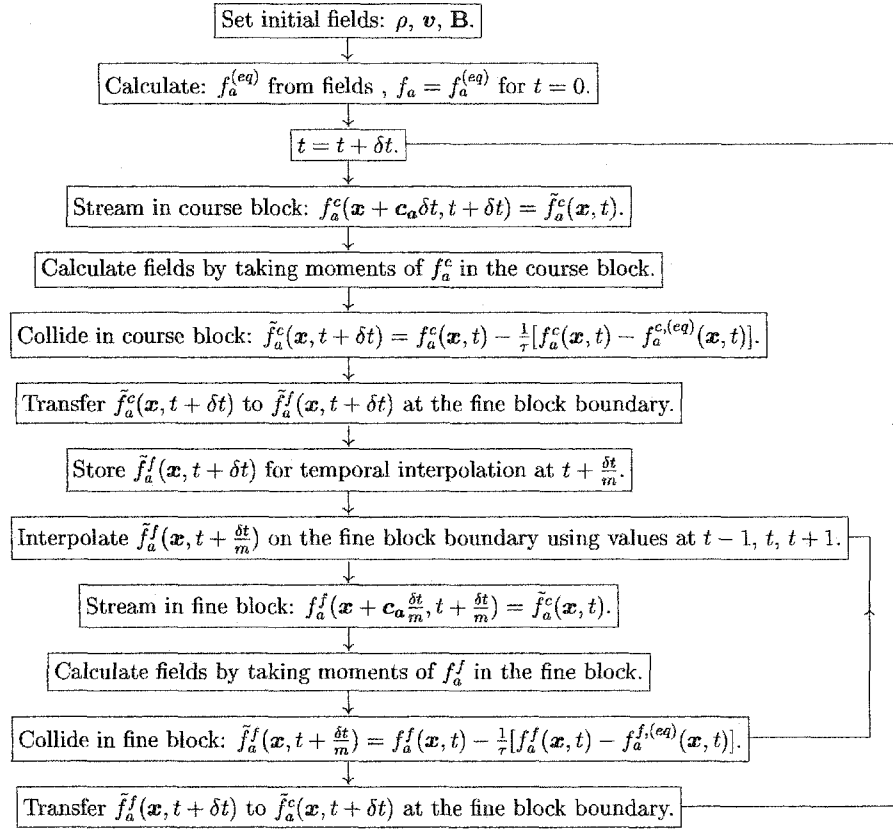


Figure 7.7: A flow chart of the computational procedure of the non-uniform grid LBM with coupled streaming and spatial lattices. Fractional time evolution occurs on the fine grid and additional collision steps are used to exchange information between the coarse and fine grids.

occurs on the fine grid. As was explained previously, "m" time steps on the fine grid correspond to one time step on the coarse grid. The only additional issue which needs to be explained is the temporal interpolation that now needs to occur at the interface when a coarse grid distribution function is being transferred to a fine distribution function. A temporal interpolation is needed because the coarse grid does not contain streaming information for the fractional time steps, which are needed for evolution on the fine grid. For this interface point, we simply interpolate $f_a^c(t + \frac{1}{m})$ from f_a^c at $t = t - 1, t = t$ and $t = t + 1$. This constitutes a second

order Lagrange interpolation, which was derived in detail previously. During the first time step however, the distribution function at $t = t - 1$ is not available, so a simple average (or first order Lagrange interpolation) between the $t = 0$ and $t = 1$ is used.

7.3.2 Testing the Coupled Lattice Model

We will again test the benefits gained by this coupled lattice unmatched node LBM by comparing it against a standard LBM for the same number of total grid points. Figure (7.8) shows such a comparison for simulations containing 600 grid points. The standard LBM uniformly distributes the points over the periodic regime while the coupled lattice unmatched procedure places 300 grid points in the inner $\frac{1}{5}$ of the plot and spreads the remaining 300 grid points over the outer regions. The refinement factor was thus set to $m = 4$ to accommodate this distribution. 600 LBM time steps on the uniform grid correspond to 375 LBM time steps on the non-uniform grid and both correspond to one dimensionless time step. Both simulations were run for 4 dimensionless time steps with an initial velocity of $v_0 = 1$. For the uniform grid simulation, the relaxation constant was set to $\tau = .52$ and the free parameter was set to $\lambda = \frac{25}{3}$. This gives a viscosity of $\nu = .1667$, and a Reynolds number of $Re = 3600$. For the non-uniform grid simulation, the relaxation constant was set to $\tau = .5125$ and the free parameter was set to $\lambda = \frac{25}{3}$. This gives a viscosity of $\nu = .1042$, and a Reynolds number of $Re = 3600$. The velocity field profile in dimensionless time steps is plotted for $t=0$, $t=2$, and $t=4$. The numerical oscillations no longer occur in the coupled unmatched node LBM. While the coupled non-uniform grid simulation does represent a 56% increase in computational expenditure, this does not compare to the 1600% increase in computational expenditure that a uniform grid LBM would

need to achieve the same resolution. Figure (7.9) shows the region adjacent to the upper left half of the shock front in greater detail. Only the $t=2$ and $t=4$ velocity profiles are shown in this high resolution view.

The coupled streaming and spatial lattice non-uniform grid LBM produces a robust methodology for simulating one dimensional fluid flow. It allows us to refine the grid in the regions where large gradients in the fields develop thus decreasing the field gradients with respect to the grid density. This process achieves higher numerical accuracy resulting in the elimination of numerical oscillations around shock fronts. In particular, the coupled lattice methodology has the advantage of allowing for arbitrarily large levels of refinement in regions containing shocks that can not be adequately resolved by a two fold refinement factor.

A Comparison of Uniform and Non-Uniform Grid LBMs

$v(x)$ vs. x , both simulations use 600 grid points

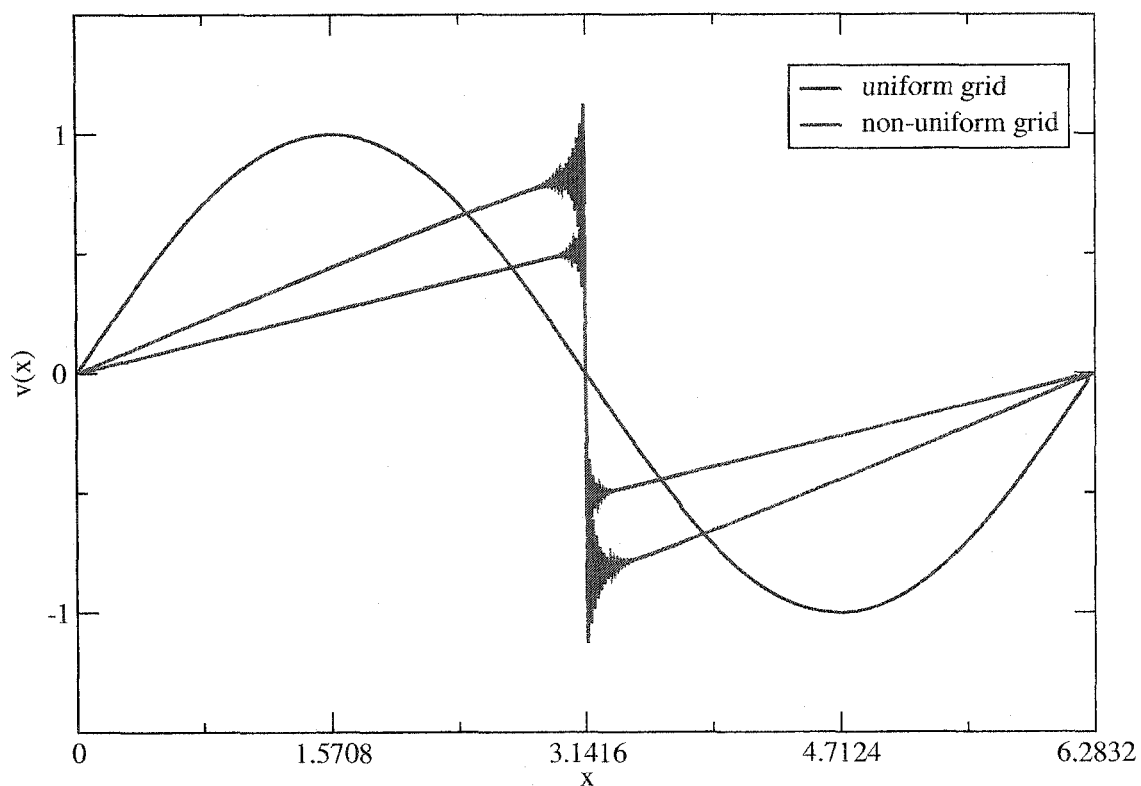


Figure 7.8: A comparison of simulations of Burger's equation for a simple sine function using a uniform (blue) and coupled non-uniform (red) LBM. Both models use 600 grid points, but the non-uniform unmatched node model has the grid points distributed more densely in the region of the shock. No numerical oscillations are visible in the coupled non-uniform grid simulation.

A Comparison of Uniform and Non-Uniform Grid LBM's

$v(x)$ vs. x , both simulations use 600 grid points

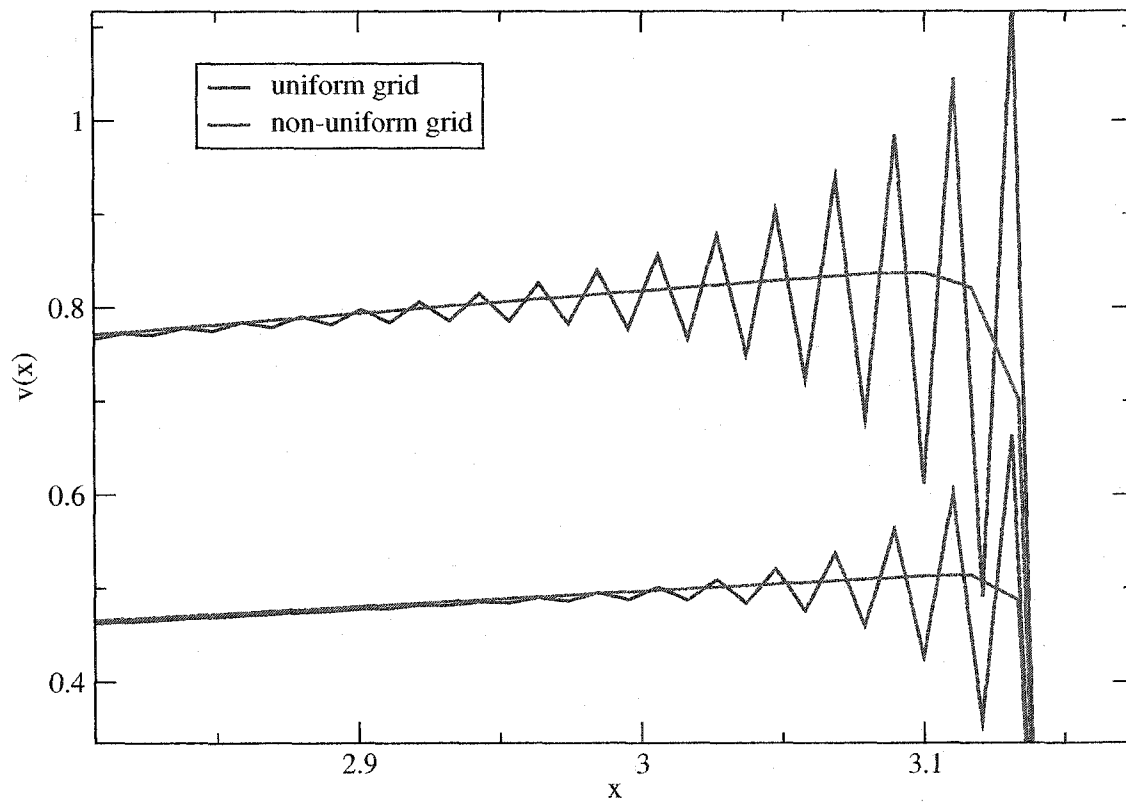


Figure 7.9: A zoomed in view of the plot in Fig. (7.3.2) in the region of the upper left shock front. The oscillations do not appear in the coupled non-uniform unmatched node LBM.

CHAPTER 8

Lattice Boltzmann Model For 1-D Resistive MHD

8.1 Derivation of the One Dimensional Resistive MHD Equations

Some fascinating results can be obtained from the resistive MHD equations when they are recast in a one dimensional framework. Their one dimensional form bear strong resemblance to Burger's equation. So much so, that the one dimensional resistive MHD problem is sometimes referred to as the magnetized Burger's equations. We can proceed with a derivation of these equations in a manner similar to that which was used to derive Burger's equation.

In deriving this set of one dimensional dissipative equations, which retain most of the essential features of MHD turbulence[29], we begin with a set of dissipative

MHD equations

$$\partial_t \rho + \nabla \cdot (\rho \mathbf{v}) = 0 \quad (8.1)$$

$$\partial_t (\rho \mathbf{v}) + \nabla P + (\mathbf{v} \cdot \nabla)(\rho \mathbf{v}) + \mathbf{v}[\nabla \cdot (\rho \mathbf{v})] + \mathbf{B} \times (\nabla \times \mathbf{B}) = \nu \nabla^2 (\rho \mathbf{v}) \quad (8.2)$$

$$\partial_t \mathbf{B} - \nabla \times (\mathbf{v} \times \mathbf{B}) = \mu \nabla^2 \mathbf{B} \quad (8.3)$$

We can apply the product rule to the time derivative in Eq. (8.2) to recover

$$\begin{aligned} \rho \partial_t \mathbf{v} + \mathbf{v} \partial_t \rho + \nabla P + (\mathbf{v} \cdot \nabla)(\rho \mathbf{v}) + \mathbf{v}[\nabla \cdot (\rho \mathbf{v})] + \\ \mathbf{B} \times (\nabla \times \mathbf{B}) = \nu \nabla^2 (\rho \mathbf{v}). \end{aligned} \quad (8.4)$$

The second and fifth terms in Eq. (8.4) constitute Eq. (8.1) multiplied by \mathbf{v} and therefore equal zero. Equation (8.4) is then rewritten as

$$\rho \partial_t \mathbf{v} + \nabla P + (\mathbf{v} \cdot \nabla)(\rho \mathbf{v}) + \mathbf{B} \times (\nabla \times \mathbf{B}) = \nu \nabla^2 (\rho \mathbf{v}). \quad (8.5)$$

The following restrictions can be placed on the density, velocity, and magnetic fields of Eqs. (8.1), (8.5) and (8.3):

(1) Gradients of the density field are significantly smaller than gradients in the velocity and magnetic fields.

(2) The velocity field contains only those components, which lie along the “x” axis and is a function only of position along the “x” axis and time.

(3) The magnetic field contains only those components, which are orthogonal to the “x” axis and is a function only of the position along the “x” axis and time.

(4) The closure approximation $P = \rho c_s^2$ is made.

Condition (1) specifies that small gradients formed from the evolution of the continuity equation will not significantly effect the momentum and magnetic induction equations. We will therefore ignore the continuity equation as it is not needed to achieve a closed set of momentum and magnetic induction equations. Condition (1) and (4) require that the pressure be devoid of gradients. Hence the second term in Eq. (8.5) becomes zero. Also, the density can be moved outside of the partial derivatives in Eq. (8.5). By enforcing conditions (2) and (3), Eq. (8.2) becomes

$$\rho_0 \partial_t v_x + B_y \partial_x B_y + B_z \partial_x B_z + \rho_0 v_x \partial_x v_x = \nu \rho_0 \partial_x^2 v_x, \quad (8.6)$$

which can be divided by ρ_0 to give

$$\partial_t v_x + \frac{1}{\rho_0} B_y \partial_x B_y + \frac{1}{\rho_0} B_z \partial_x B_z + v_x \partial_x v_x = \nu \partial_x^2 v_x. \quad (8.7)$$

Finally, we can apply the inverse chain rule to recover

$$\partial_t v_x + \frac{1}{2\rho_0} \partial_x (B_y^2) + \frac{1}{2\rho_0} \partial_x (B_z^2) + \frac{1}{2} \partial_x (v_x^2) = \nu \partial_x^2 v_x. \quad (8.8)$$

Conditions (2) and (3) can be enforced on Eq. (8.3) and we can divide by $\sqrt{\rho_0}$ to give

$$\frac{1}{\sqrt{\rho_0}} \partial_t B_y + \frac{1}{\sqrt{\rho_0}} \partial_x (v_x B_y) = \frac{1}{\sqrt{\rho_0}} \mu \partial_x^2 B_y, \quad (8.9)$$

$$\frac{1}{\sqrt{\rho_0}} \partial_t B_z + \frac{1}{\sqrt{\rho_0}} \partial_x (v_x B_z) = \frac{1}{\sqrt{\rho_0}} \mu \partial_x^2 B_z. \quad (8.10)$$

The factor of $\frac{1}{\sqrt{\rho_0}}$ can be absorbed into the definition of B_x and B_y and Eqs. (8.8), (8.9) and (8.10) become

$$\partial_t v_x + \frac{1}{2} \partial_x (B_y^2) + \frac{1}{2} \partial_x (B_z^2) + \frac{1}{2} \partial_x (v_x^2) = \nu \partial_x^2 v_x, \quad (8.11)$$

$$\partial_t B_y + \partial_x (v_x B_y) = \mu \partial_x^2 B_y, \quad (8.12)$$

$$\partial_t B_z + \partial_x (v_x B_z) = \mu \partial_x^2 B_z. \quad (8.13)$$

Equations (8.11), (8.12) and (8.13) form a closed set of one dimensional equations for the velocity and magnetic field. It should be noted that in the limit of no magnetic field, our system reduces to Burger's equation. Further, a self consistent magnetic feedback pressure now contributes to the evolution of the velocity field, an effect that is obviously missing from Burger's equation.

8.2 Derivation of the Lattice Boltzmann

Model for 1-D Resistive MHD

We begin the derivation of the LBM for one dimensional resistive MHD with a general set of distribution functions formed from an expansion of powers of the fields v_x , B_y and B_z . The magnetic field will be written in its vector form B_i , where it is understood that it is comprised only of \hat{j} and \hat{k} components. The velocity field will simply be written as "v", where it is understood that it consists only of an \hat{i}

component. The general distribution functions are

$$f_0^{(eq)} = k_1 v + k_2 v^2 + k_3 B^2, \quad (8.14)$$

$$f_+^{(eq)} = k_4 v + k_5 v^2 + k_6 B^2, \quad (8.15)$$

$$f_-^{(eq)} = k_7 v + k_8 v^2 + k_9 B^2, \quad (8.16)$$

$$g_{0,i}^{(eq)} = k_{10} B_i + k_{11} v B_i, \quad (8.17)$$

$$g_{+,i}^{(eq)} = k_{12} B_i + k_{13} v B_i, \quad (8.18)$$

$$g_{-,i}^{(eq)} = k_{14} B_i + k_{15} v B_i, \quad (8.19)$$

where $g_{a,i}^{(eq)}$ is a vector distribution function as it was in the two dimensional model. We can use Eq. (3.8) to identify the appropriate definitions of the moments of these distribution functions

$$v_x = \sum_a f_a^{eq}, \quad (8.20)$$

$$\frac{v^2}{2} + \frac{B^2}{2} = \sum_a f_a^{eq} c_a, \quad (8.21)$$

$$\alpha v = \sum_a f_a^{(eq)} c_a^2, \quad (8.22)$$

$$B_i = \sum_a g_{a,i}^{eq}, \quad (8.23)$$

$$v B_i = \sum_a g_{a,i}^{eq} c_a, \quad (8.24)$$

$$\beta B_i = \sum_a g_{a,i}^{(eq)} c_a^2, \quad (8.25)$$

where α and β are arbitrary constants that will control the viscosity and resistivity, respectively. The enforcement of Eq. (8.20) on Eqs. (8.14), (8.15) and (8.16) provides us with

$$k_1 + k_4 + k_7 = 1, \quad (8.26)$$

$$k_2 + k_5 + k_8 = 0, \quad (8.27)$$

$$k_3 + k_6 + k_9 = 0. \quad (8.28)$$

Equation (8.21) also contains Eqs. (8.14), (8.15) and (8.16) to produce

$$k_4 - k_7 = 0, \quad (8.29)$$

$$k_5 - k_8 = \frac{1}{2|c|}, \quad (8.30)$$

$$k_6 - k_9 = \frac{1}{2|c|}. \quad (8.31)$$

Finally, Eq. (8.22) acts on Eqs. (8.14), (8.15) and (8.16) to produce

$$k_4 + k_7 = \frac{\alpha}{c^2}, \quad (8.32)$$

$$k_5 + k_8 = 0, \quad (8.33)$$

$$k_6 + k_9 = 0. \quad (8.34)$$

Solving Eqs. (8.26)-(8.34) for the constants k_1 - k_9 gives

$$\begin{array}{lll} k_1 = 1 - \frac{\alpha v}{2c^2} & k_2 = 0 & k_3 = 0 \\ k_4 = \frac{\alpha}{2c^2} & k_5 = \frac{1}{4c} & k_6 = \frac{1}{4c} \\ k_7 = \frac{\alpha}{2c^2} & k_8 = -\frac{1}{4c} & k_9 = -\frac{1}{4c} \end{array}$$

and the general distribution functions defined in Eqs. (8.14)-(8.16) become

$$f_0^{(eq)} = v - \frac{\alpha v}{c^2}, \quad (8.35)$$

$$f_+^{(eq)} = \frac{\alpha v}{2c^2} + \frac{v^2}{4c} + \frac{B_i^2}{4c}, \quad (8.36)$$

$$f_-^{(eq)} = \frac{\alpha v}{2c^2} - \frac{v^2}{4c} - \frac{B_i^2}{4c}. \quad (8.37)$$

The enforcement of Eq. (8.23) on Eqs. (8.17), (8.18) and (8.19) provides us with

$$k_{10} + k_{12} + k_{14} = 1, \quad (8.38)$$

$$k_{11} + k_{13} + k_{15} = 0. \quad (8.39)$$

Applying Eq. (8.24) to Eqs. (8.17), (8.18) and (8.19) gives

$$k_{12} - k_{14} = 0, \quad (8.40)$$

$$k_{13} - k_{15} = \frac{1}{|c|}. \quad (8.41)$$

And, Eq. (8.25) constrains Eqs. (8.17), (8.18) and (8.19) to produce

$$k_{12} + k_{14} = \frac{\beta}{c^2}, \quad (8.42)$$

$$k_{13} + k_{15} = 0. \quad (8.43)$$

Solving Eqs. (8.38)-(8.43) for the constants k_{10} - k_{15} gives

$$\begin{aligned} k_{10} &= 1 - \frac{\beta}{c^2} & k_{11} &= 0 \\ k_{12} &= \frac{\beta}{2c^2} & k_{13} &= \frac{1}{2c} \\ k_{14} &= \frac{\beta}{2c^2} & k_{15} &= -\frac{1}{2c} \end{aligned}$$

and the general distribution functions defined in Eqs. (8.14)-(8.16) become

$$g_{0,i}^{(eq)} = B_i - \frac{\beta B_i}{c^2}, \quad (8.44)$$

$$g_{+,i}^{(eq)} = \frac{\beta B_i}{2c^2} + \frac{v B_i}{2c}, \quad (8.45)$$

$$g_{-,i}^{(eq)} = \frac{\beta B_i}{2c^2} - \frac{v B_i}{2c}. \quad (8.46)$$

Eq. (3.8) can now be applied to both distribution functions in the standard way. Moving the lattice vectors inside the partial derivatives and summing over “a” produces

$$\partial_{t_0} v + \frac{1}{2} \partial_x (v^2 + B_i^2) = 0, \quad (8.47)$$

$$\partial_{t_0} B_i + \partial_x (v B_i) = 0, \quad (8.48)$$

which constitute the one dimensional MHD equations at the zeroth inviscid time scale. We can also move the lattice vectors inside the partial derivatives of Eq.

(3.12) and apply it to both distribution functions. Summing over “a” gives

$$\partial_{t_1} v - \left(\tau - \frac{1}{2}\right) [\partial_{t_0}^2 v + \partial_{t_0} \partial_x (v^2 + B_i^2) + \alpha \partial_x^2 v] = 0, \quad (8.49)$$

$$\partial_{t_1} B_i - \left(\tau - \frac{1}{2}\right) [\partial_{t_0}^2 B_i + 2\partial_{t_0} \partial_x (v B_i) + \beta \partial_x^2 B_i] = 0. \quad (8.50)$$

Equations (8.47) and (8.48) can be used to cancel the second term and half of the third term in Eqs. (8.49) and (8.50) to give

$$\partial_{t_1} v - \left(\tau - \frac{1}{2}\right) \left[\frac{1}{2} \partial_{t_0} \partial_x (v^2 + B_i^2) + \alpha \partial_x^2 v\right] = 0, \quad (8.51)$$

$$\partial_{t_1} B_i - \left(\tau - \frac{1}{2}\right) [\partial_{t_0} \partial_x (v B_i) + \beta \partial_x^2 B_i] = 0 \quad (8.52)$$

and employing the chain and product rules on the second term in both Eq. (8.51) and (8.52) produces

$$\partial_{t_1} v - \left(\tau - \frac{1}{2}\right) [\partial_x v \partial_{t_0} v + \partial_x B_i \partial_{t_0} B_i + \alpha \partial_x^2 v] = 0, \quad (8.53)$$

$$\partial_{t_1} B_i - \left(\tau - \frac{1}{2}\right) [\partial_x v \partial_{t_0} B_i + \partial_x B_i \partial_{t_0} v + \beta \partial_x^2 B_i] = 0. \quad (8.54)$$

Equations (8.47) and (8.48) can again be used to exchange the temporal derivatives in the first and second terms for the spatial derivative terms and Eqs. (8.53) and

(8.53) become

$$\partial_{t_1} v - \left(\tau - \frac{1}{2}\right) \left[-\frac{1}{2} \partial_x v \partial_x (v^2 + B^2) - \partial_x B_i \partial_x (v B_i) + \alpha \partial_x^2 v\right] = 0, \quad (8.55)$$

$$\partial_{t_1} B_i - \left(\tau - \frac{1}{2}\right) \left[-\partial_x v \partial_x (v B_i) - \frac{1}{2} \partial_x B_i \partial_x (v^2 + B_i^2) + \beta \partial_x^2 B_i\right] = 0. \quad (8.56)$$

Finally, we recast Eqs. (8.55) and (8.56) in the form

$$\partial_{t_1} v = \nu \partial_x^2 v + O(\partial_x^2 \mathbf{A}^3), \quad (8.57)$$

$$\partial_{t_1} B_i = \mu \partial_x^2 B_i + O(\partial_x^2 \mathbf{A}^3) \quad (8.58)$$

where the viscosity and resistivity are defined by

$$\nu \equiv \alpha \left(\tau - \frac{1}{2}\right), \quad (8.59)$$

$$\mu \equiv \beta \left(\tau - \frac{1}{2}\right) \quad (8.60)$$

and the higher order terms containing two spatial derivatives and three fold combinations of the fields are represented by $O(\partial_x^2 \mathbf{A}^3)$. The addition of Eqs. (8.47) and (8.57) produce Eq. (8.11) and the addition of Eqs. (8.48) and (8.58) produce Eq. (8.13). The existence of two fields adds some spurious non-linear cubic terms as we also saw in the two dimensional MHD models, but these terms remain small for small local gradients in the fields. This is a particularly good approximation for

non-uniform grid models as the gradients are significantly reduced (relative to the number of lattice nodes) by the refinement procedures.

CHAPTER 9

Simulations of 1-D Resistive MHD Using Uniform and Non-Uniform Grid LBMs

9.1 Comparison of MHD and Burgers Turbulence

We will begin our simulations of one dimensional resistive MHD by extending the simple sinusoidal profile that we have used for Burger's equation to one which includes a magnetic field. In general, the presence of a magnetic field allows for the transfer of energy between the velocity and magnetic fields. This transfer of energy is most apparent in the regions where strong shocks develop.

Figure (9.1) shows the initial profile for a simulation which adds small sinusoidal oscillations in the magnetic fields to the standard sinusoidal velocity profile. This

Initial Profile of Fields for 1-D MHD

$v_z(z)$, $B_x(z)$, and $B_y(z)$ vs. z

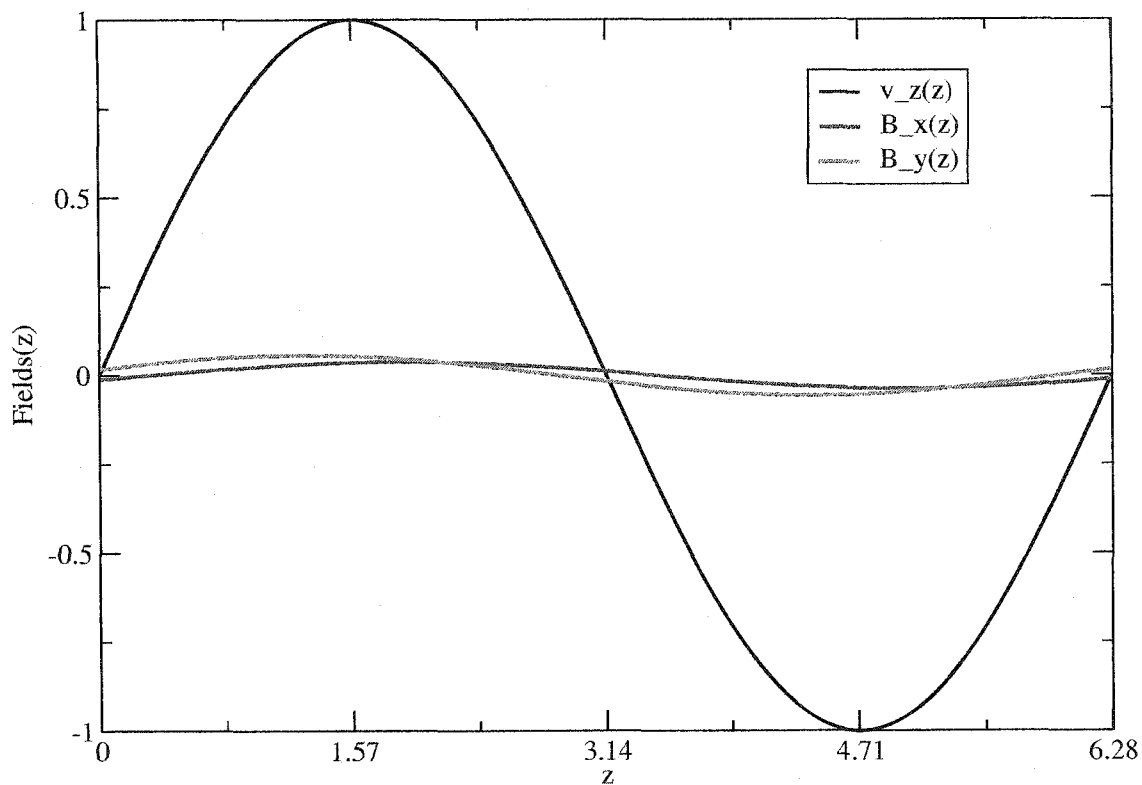


Figure 9.1: *Initial profile of the 1-D MHD simulation. Most of the initial energy lies in the velocity field.*

simulation used an initial field profile given by

$$v_z(z) = v_0 \sin\left(\frac{z}{2\pi}\right) \quad (9.1)$$

$$B_x(z) = B_{x,0} \sin\left(\frac{z}{2\pi} - .3\right) \quad (9.2)$$

$$B_y(z) = B_{y,0} \sin\left(\frac{z}{2\pi} + .3\right) \quad (9.3)$$

where the initial velocity was set to $v_0 = 1$ and the initial magnetic fields were set to $B_{x,0} = .038$ and $B_{y,0} = .057$. The simulation was run on a non-uniform grid with 1281 nodes spanning the region from 0 to $\frac{5\pi}{8}$, 6144 nodes spanning the region from $\frac{5\pi}{8}$ to $\frac{11\pi}{8}$, and 1281 nodes spanning the region from $\frac{11\pi}{8}$ to 2π . The middle region thus contains a refinement factor of $m = 4$. The relaxation constants were set to $\tau_\nu = \tau_\mu = .6$ and the free parameters were set to $\alpha = \beta = \frac{25}{3}$. This gives a viscosity and resistivity of $\nu = \mu = .8333$, which gives a Reynolds number of $R = 4915.2$ and a magnetic Reynolds number of $R_m = 336.71$. The simulation was run for 18,000 LBM time steps.

Figure (9.2) shows the evolution of the velocity profile after 1000, 2000, and 3000 LBM time steps. The velocity profile matches that of Burger's equation almost exactly (so much so that it was not worthwhile to plot both evolutions here). The differences are not apparent because most of the total energy of the system is still contained in the velocity profile and hence the magnetic field is only weakly affecting the velocity field evolution.

Figures (9.3) and (9.4) show the evolution of the magnetic fields during the same time period. The initial sinusoidal profiles are distorted as the shock front in the velocity field steepens. They contain the majority of their energy in the regions immediately adjacent to the front of the left and right shock. The initial differences between B_x and B_y become less apparent as the simulation progresses. Specifically, the symmetry of the velocity field about $z = \pi$ imposes itself on the magnetic fields such that they become mirror images of each other. We therefore have the approximate relation $B_x(z - \pi) \approx -B_y(\pi - z)$, due to the asymmetry of the initial velocity field about π and its overwhelmingly large magnitude as compared to the initial magnetic fields.

Figure (9.5) shows a comparison of the 1-D MHD and Burger's equation velocity

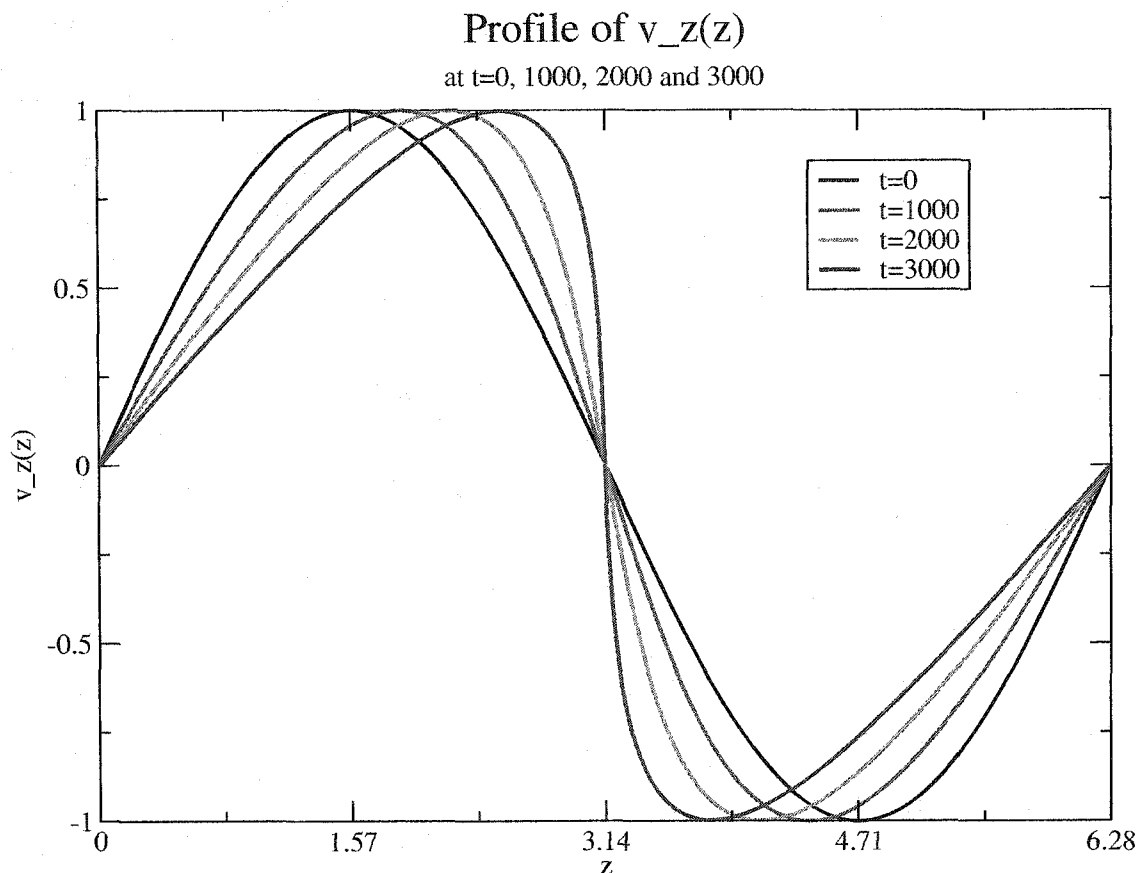


Figure 9.2: *The early evolution of the velocity field closely resembles that of Burger's equation. The magnetic field does not yet contain enough energy to influence the velocity profile.*

profiles. The parameters for the Burger's simulation are exactly the same as the parameters for the velocity component of the MHD simulation. The velocity field profiles after 4000, 8000, and 12000 LBM time steps show that enough energy has been transferred to the magnetic fields for it to alter the velocity field. In particular, the shock fronts are slightly less steep and a small sub-structure appears in the region between the large front of each shock. Figure (9.6) shows the region around the left shock front in greater detail. The sub-structure decays away over time and then re-appears in the final stages of the simulation due to the interactions between the

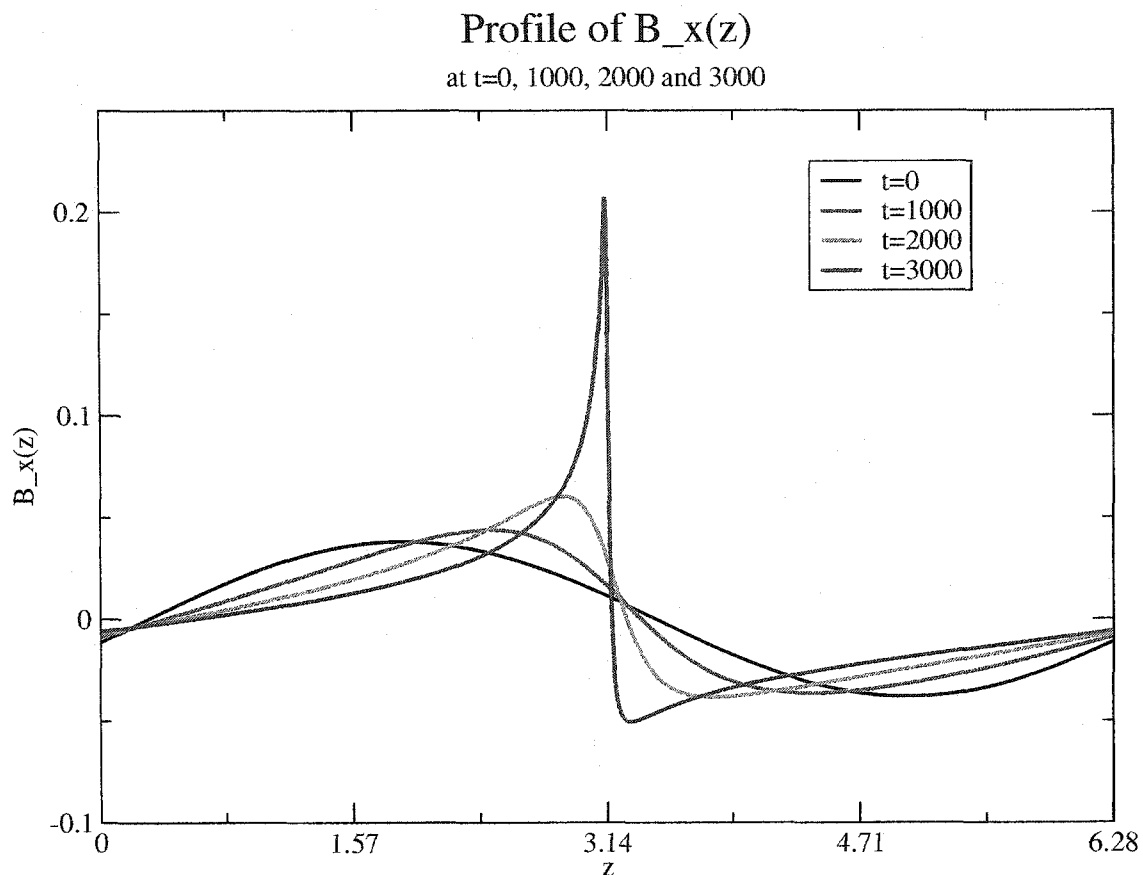


Figure 9.3: *Early evolution of the “x” component of the magnetic field. As the velocity shock forms, the magnetic profile is distorted by the transfer of kinetic to magnetic energy.*

velocity and magnetic fields. The most remarkable difference between the Burger’s and MHD velocity profiles lies in the interaction between the left and right shock. In the Burger’s simulation, the shock fronts collide and the total energy is dissipated by the viscous term, whereas the velocity shock fronts do not collide in the MHD simulation. Rather, they transfer energy to the magnetic profiles and dissipation occurs via the collision of the velocity shocks with the magnetic structures. It is thus the magnetic fields, which mediate the dissipation of the kinetic energy of the velocity shocks. For simulations with lower Reynolds and magnetic Reynolds

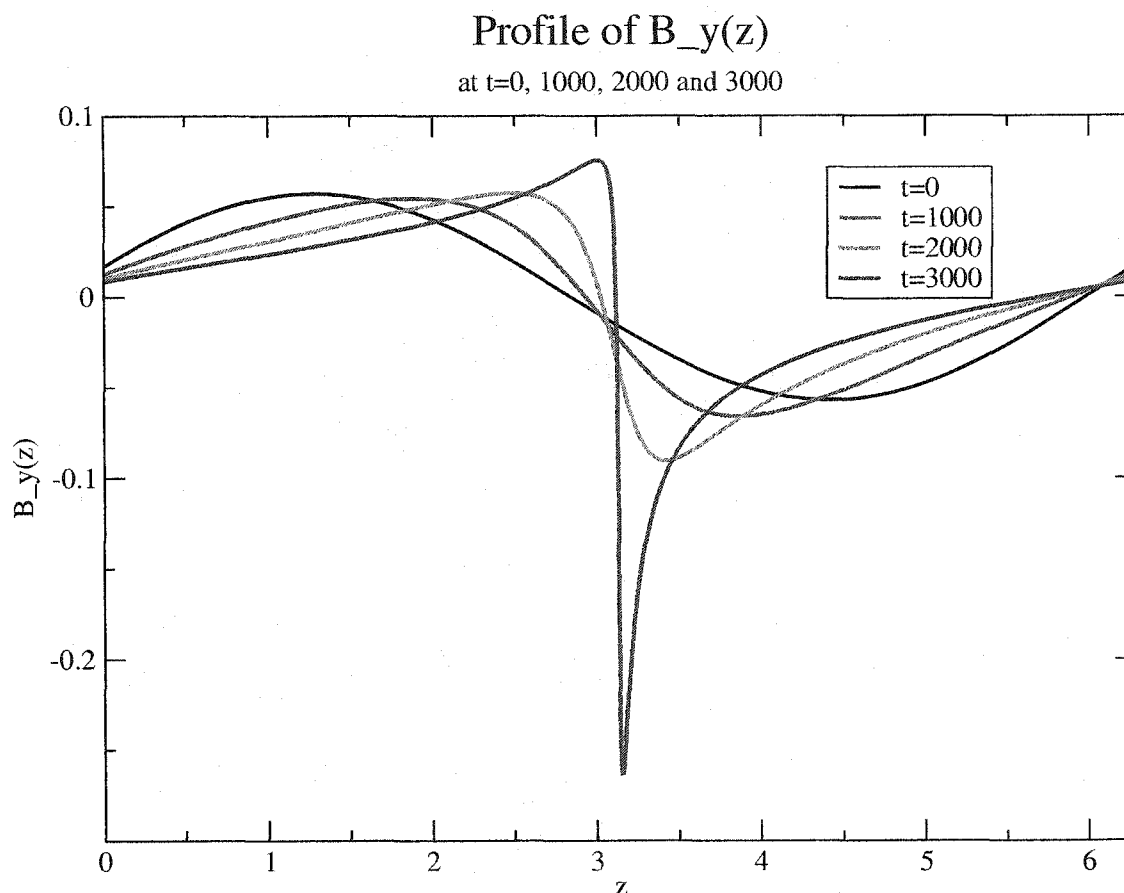


Figure 9.4: *Early evolution of the “y” component of the magnetic field. Although the magnetic energy is increasing in time, it does not yet significantly alter the velocity profile.*

numbers this mediative effect is less pronounced as will be shown in section 9.2.

Figures (9.7) and (9.8) show the magnetic fields after 3000, 3500, 4000 and 4500 LBM time steps. The formation of the shock in the velocity field has caused large growth in the magnetic field profiles in the regions adjacent to each shock front. This turbulent process results in an exponential increase in the magnetic energy up to a saturation point which occurs after roughly 4500 LBM time steps. Figure (9.9) shows the final profile of the velocity and magnetic fields after 18000 LBM time steps with the region of the shock shown in greater detail in Fig. (9.10). One can

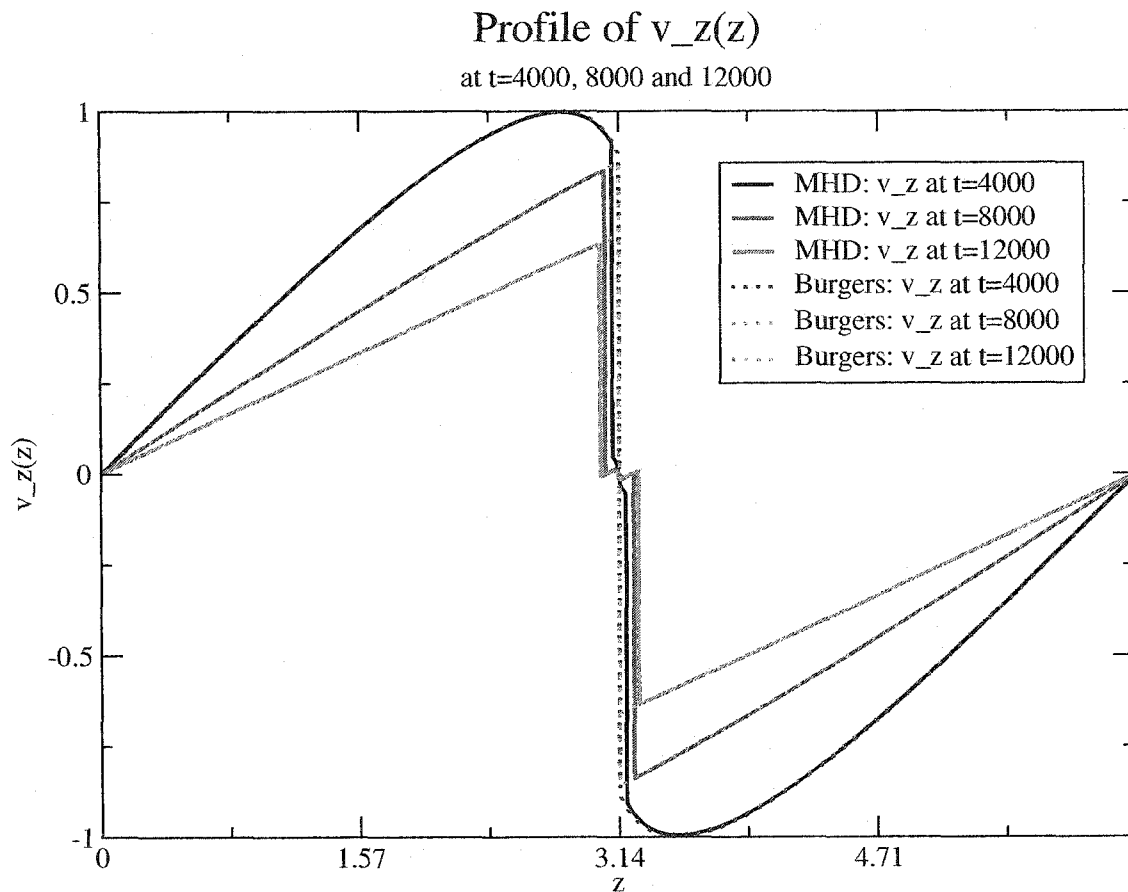


Figure 9.5: A comparison of the velocity profiles for 1-D MHD and the equivalent Burger's equation simulation. Differences between the profiles are apparent at these later stages of the evolution.

see that the magnitude of the total magnetic field, given by $|\mathbf{B}| = \sqrt{B_x^2 + B_y^2}$ is now greater than the magnitude of the velocity field in the region of the shock fronts. The anti-symmetric relationship between B_x and B_y is still apparent, providing evidence of the large initial velocity's domination of the turbulent evolution process.

Finally, Fig. (9.11) shows the temporal decay of the kinetic, magnetic and total energies. These energies were obtained from the integral over wave number space of

Blow up of the Profile of $v_z(z)$

at $t=4000, 8000$ and 12000

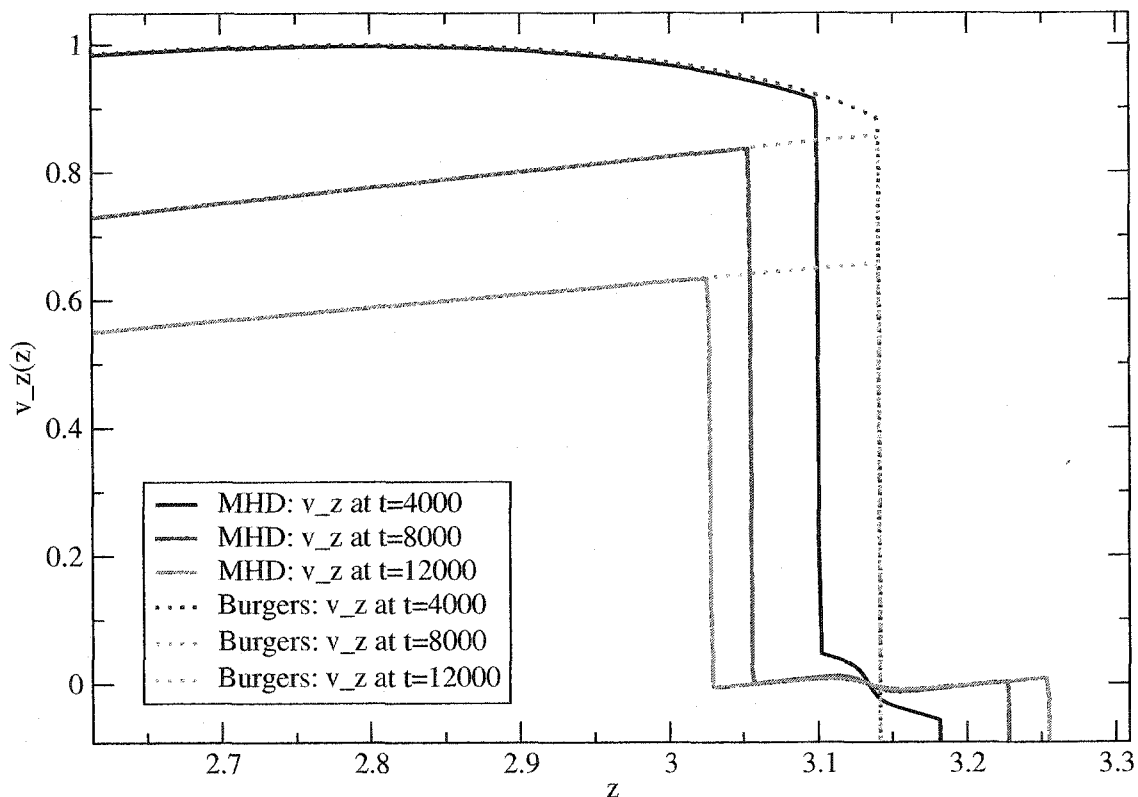


Figure 9.6: A magnified view of the comparison between 1-D MHD and Burger's simulations. The dotted lines show the steep shock front of Burger's equation compared to the sub-structure, which is apparent in the region between the MHD shock fronts.

the Fourier transformed fields

$$E_K(t) = \frac{1}{2} \int v(k, t)^2 dk, \quad (9.4)$$

$$E_M(t) = \frac{1}{2} \int (B_x(k, t)^2 + B_y(k, t)^2) dk, \quad (9.5)$$

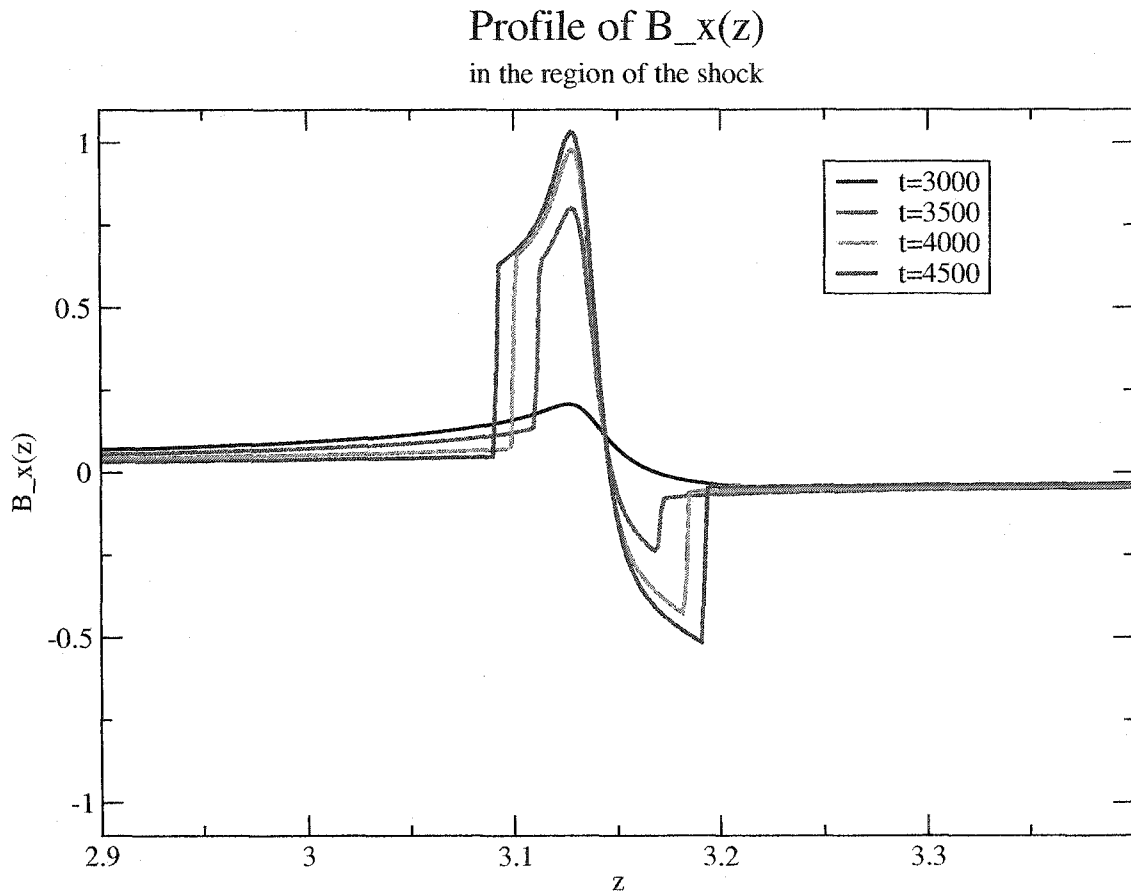


Figure 9.7: A plot of the later stage evolution of the “x” component of the magnetic field. The magnetic energy increases exponentially and begins to influence the velocity field significantly.

$$E_T(t) = E_K(t) + E_M \quad (9.6)$$

and are not conserved due to the presence of the dissipative terms in the velocity and magnetic induction equations. During the initial formation of the velocity shock (from roughly $t = 3000$ to $t = 4500$) the turbulent reorganization results in exponential increase in the magnetic energy. This exponential increase has traditionally been examined from the standpoint of current density in two and three

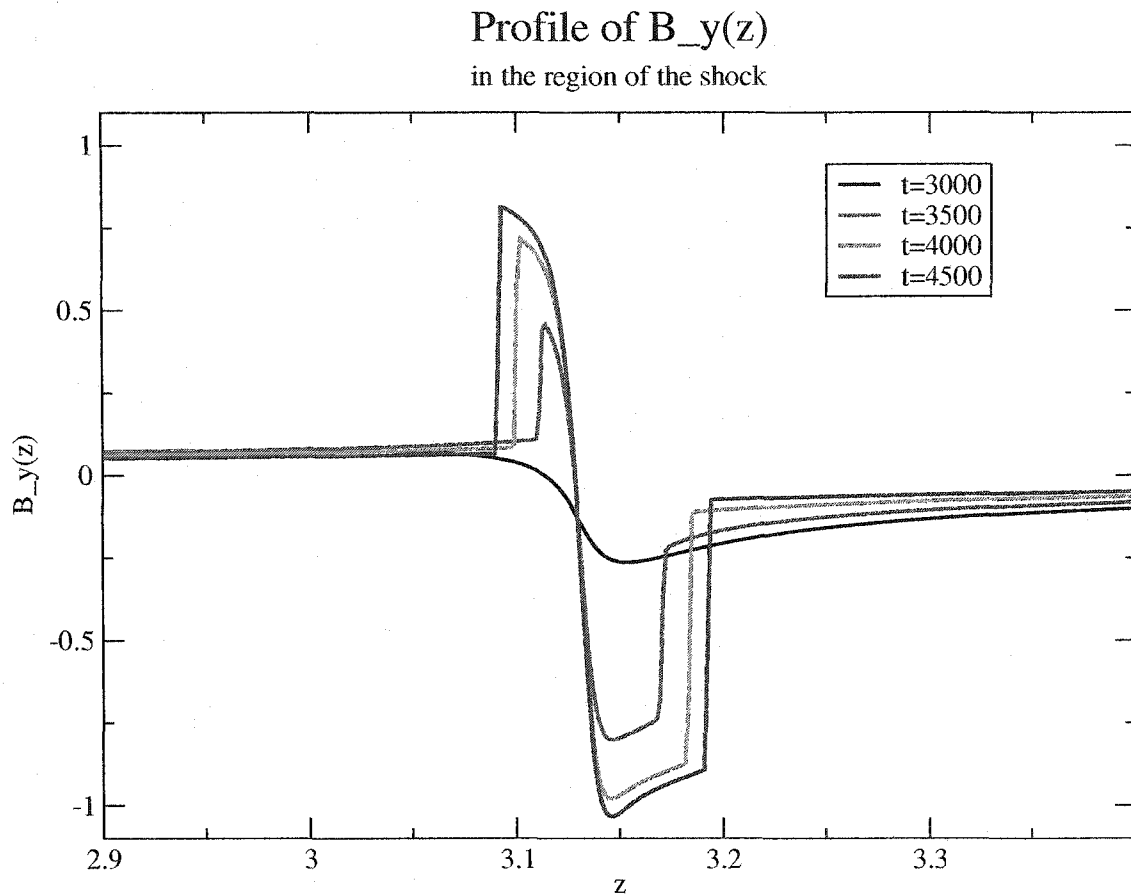


Figure 9.8: A plot of the later stage evolution of the “y” component of the magnetic field. A quasi anti-symmetry about $z = \pi$ is apparent between the “x” and “y” components of the magnetic field.

dimensional simulations. After the formation of the velocity shock the magnetic energy levels off. This is due to the conversion of kinetic to magnetic energy, which is roughly matched by the dissipation of magnetic energy. The kinetic and total energies quickly dissipate after the formation of the velocity shock.

Our examination of this simple sinusoidal velocity and magnetic field profile illustrates the striking differences that occur when magnetic phenomena is added to a simple fluid equation. In particular, the dissipation and interaction of the fields

Profile of Fields After 18000 LBM Time Steps

$v_z(z)$, $B_x(z)$ and $B_y(z)$ vs. z

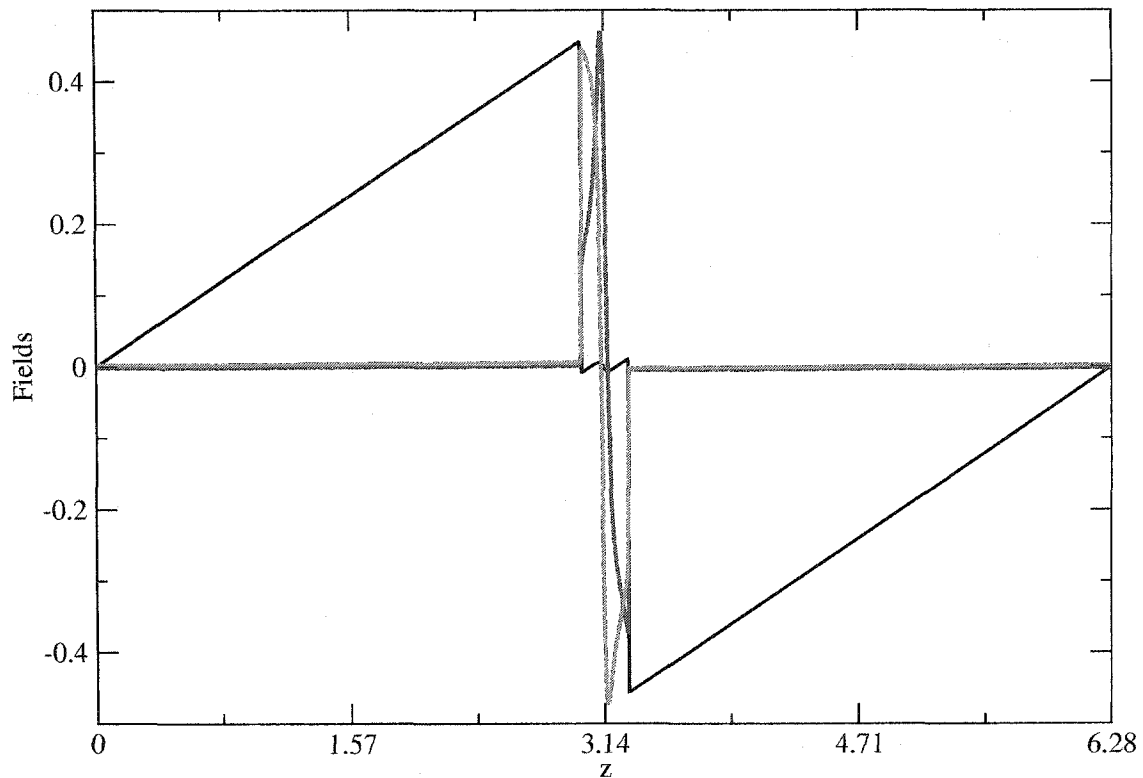


Figure 9.9: *The profile of the velocity and magnetic fields after 18000 LBM time steps. The exponential increase in magnetic energy during the formation of the velocity shock results in large magnetic structures around the shock fronts.*

become significantly more complex. The general character of the velocity field is to evolve toward sawtooth shapes while the magnetic fields evolve toward step like shapes.

Profile of Fields After 18000 LBM Time Steps

$v_z(z)$, $B_x(z)$ and $B_y(z)$ vs. z

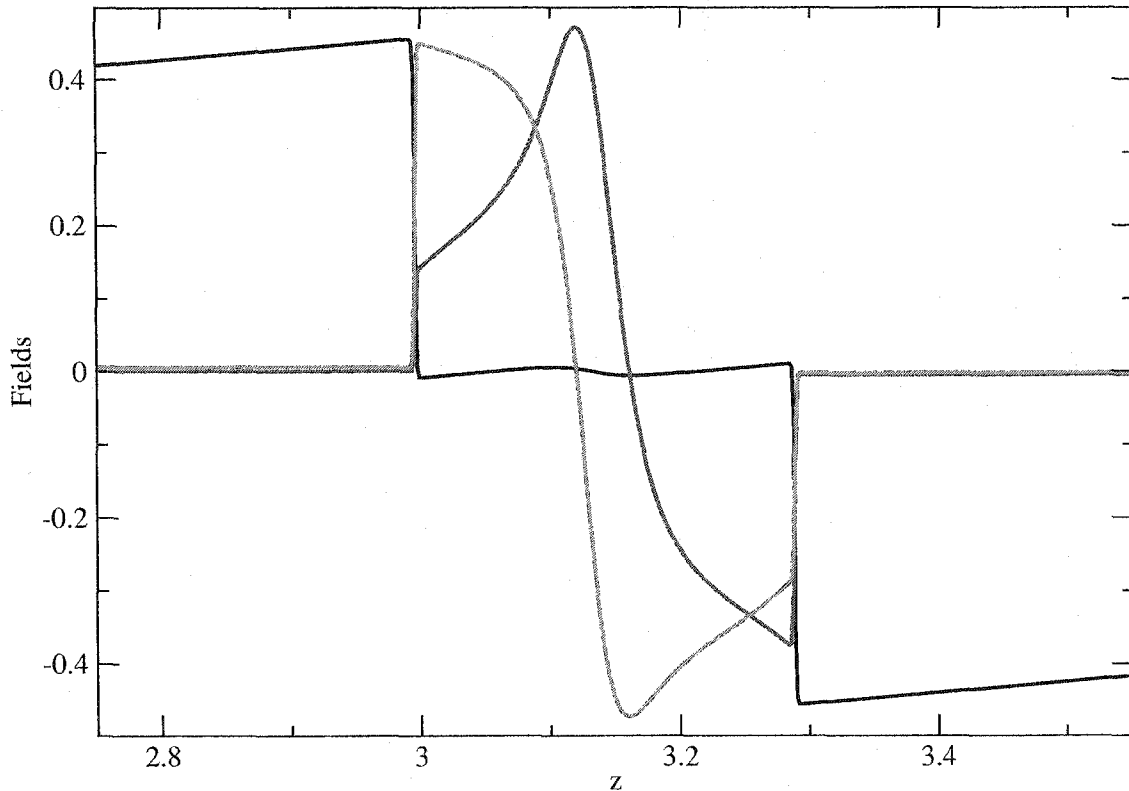


Figure 9.10: A magnified view of the final profile of the fields. The magnetic fields continue to display an anti-symmetry about $z = \pi$. The interaction of the velocity shocks are mediated by this magnetically dominated central region.

9.2 A 1-D MHD Simulation Using Gaussian Wave Packets

As a second step in examining the turbulence of one dimensional resistive MHD we can consider a more complex initial profile, which is characterized by Gaussian wave packets. It is also interesting to use an initial field distribution which contains a comparable amount of magnetic and kinetic energy. For this simulation we have

Temporal Decay of the Energies

kinetic, magnetic and total energy vs. time

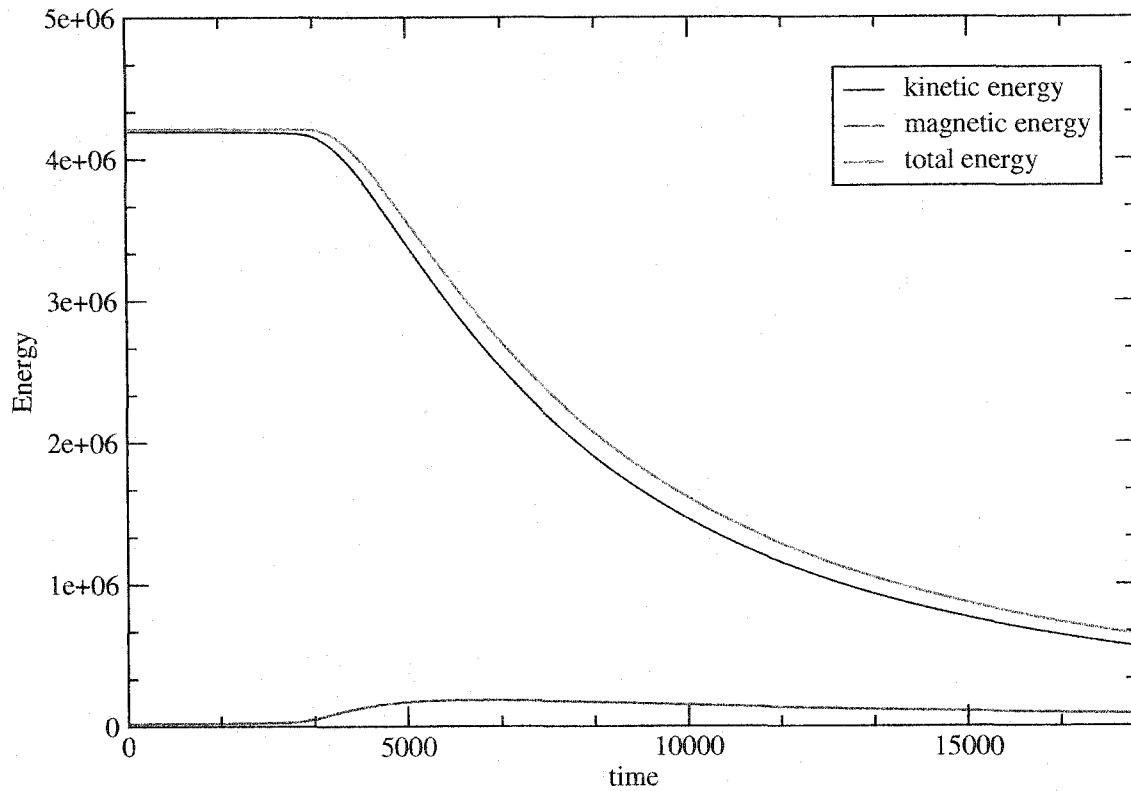


Figure 9.11: *The temporal evolution of the kinetic, magnetic, and total energies. The magnetic energy increases exponentially during the formation of the velocity shock and then levels off due to dissipative effects. The kinetic and total energy dissipation is apparent.*

chosen the initial profile

$$v(z) = v_0 * \exp[-4.0(z - \pi)^2] \cos(20z), \quad (9.7)$$

$$B_x(z) = B_{x,0} * \exp[-5.0(z - \pi)^2] \sin(15z - .30), \quad (9.8)$$

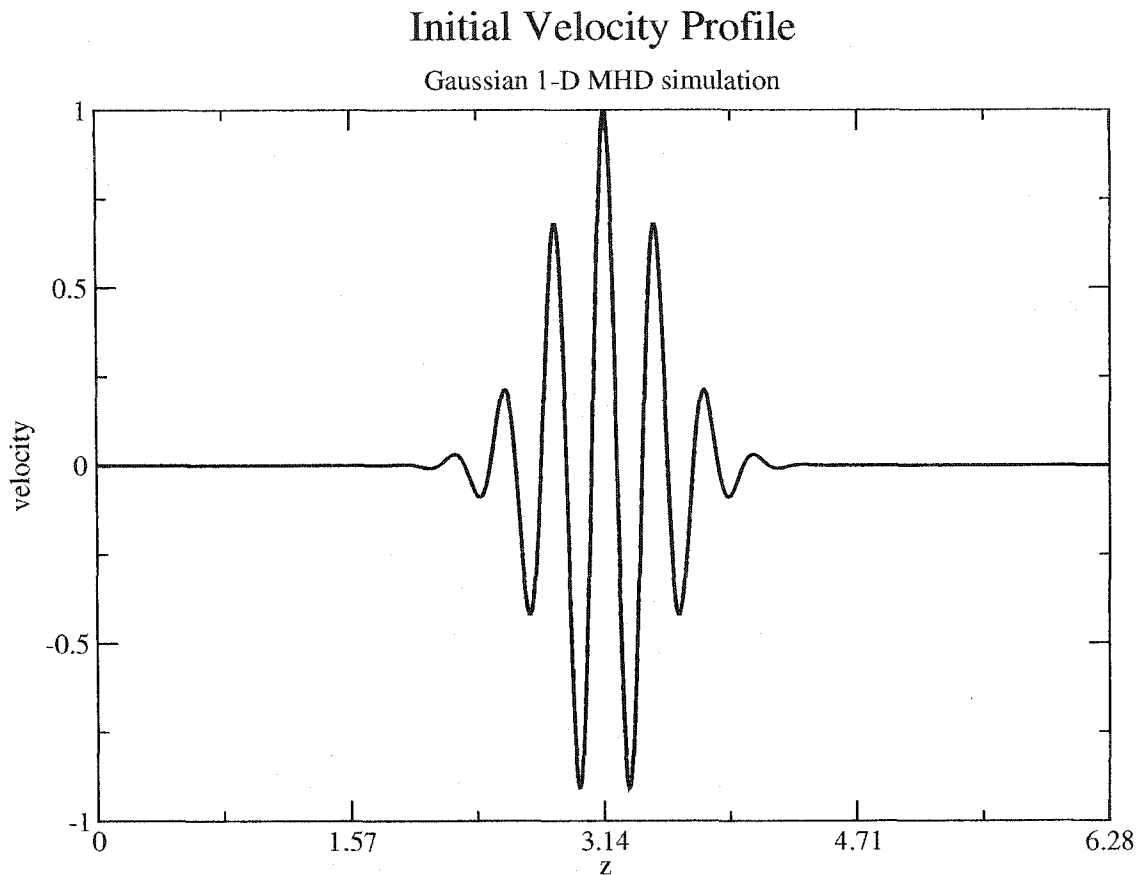


Figure 9.12: *The initial velocity profile for the Gaussian wave packet simulation.*

$$B_y(z) = B_{y,0} * \exp[-4.1(z - \pi)^2] \sin(10z + .68) \quad (9.9)$$

where the phase shifts in the trigonometric functions were chosen arbitrarily. The initial velocity profile is shown in Fig. (9.12) and the initial magnetic field profile is shown in Fig. (9.13). This simulation was run using $v_0 = 1$, $B_{x,0} = .5$ and $B_{y,0} = .6$. Roughly $\frac{2}{3}$ of the total energy is contained in the velocity profile and $\frac{1}{3}$ is contained in the magnetic field profile. The relaxation constants were set to $\tau_\nu = \tau_\mu = .55$ and the dissipative parameters were set to $\alpha = \beta = \frac{25}{3}$ to give a viscosity and resistivity of $\nu = \mu = .4167$. A non-uniform grid was used with 1025 nodes spanning the

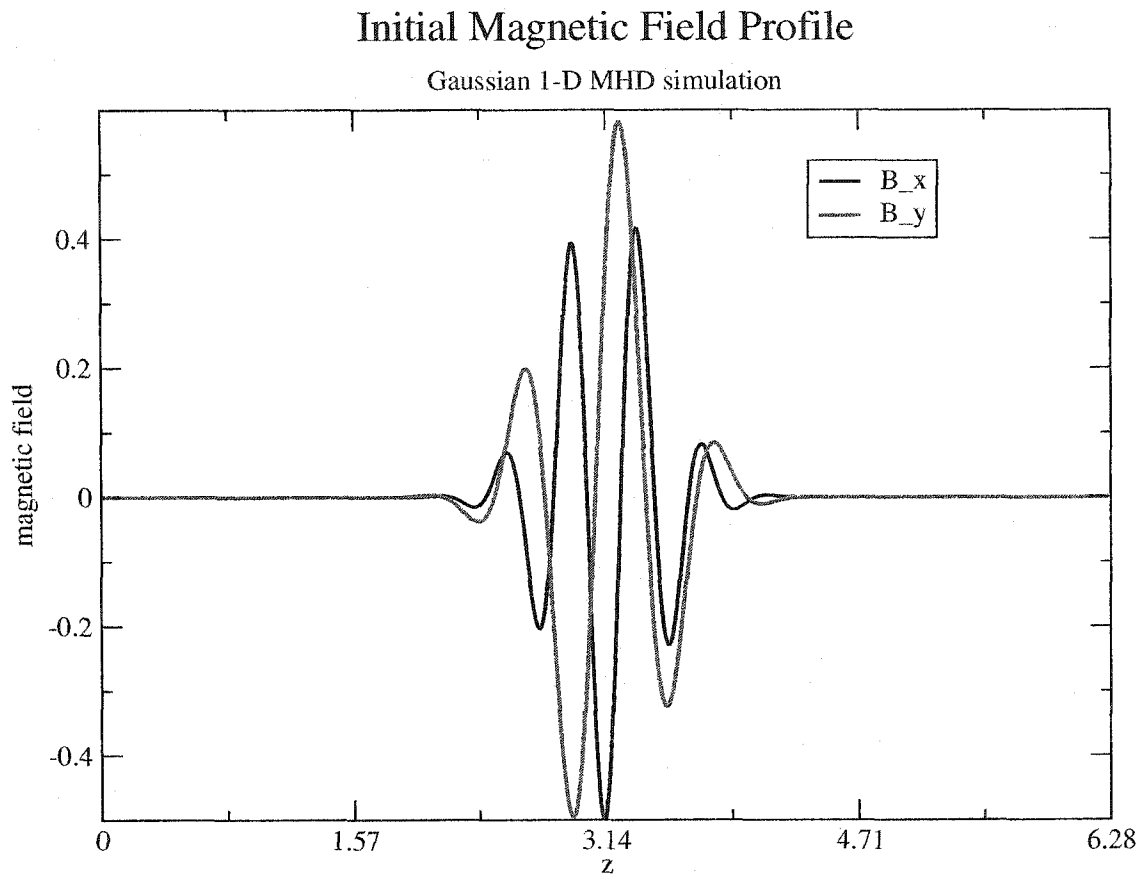


Figure 9.13: *The initial magnetic field profile for the Gaussian wave packet simulation. The magnetic field contains roughly $\frac{1}{2}$ of the energy that the velocity profile contains.*

region from 0 to $\frac{\pi}{2}$, 8192 nodes spanning the region from $\frac{\pi}{2}$ to $\frac{3\pi}{2}$, and 1025 nodes spanning the region from $\frac{3\pi}{2}$ to 2π . The central region hence uses a refinement factor of $m = 4$. The resulting Reynolds number is $R = 9830.4$ and the magnetic Reynolds number is $R_m = 7677.8$. The simulation was run for 1440 LBM time steps.

Figure (9.14) shows the velocity profile after 640 LBM time steps. The large Reynolds and magnetic Reynolds numbers result in the formation of sawtooth like shapes, which are steeper than those in the simulation presented in section 9.1. These saw teeth, however, are still not as pronounced as Burger's simulations as the magnetic field still imposes a mediative effect on coalescing velocity shock fronts.

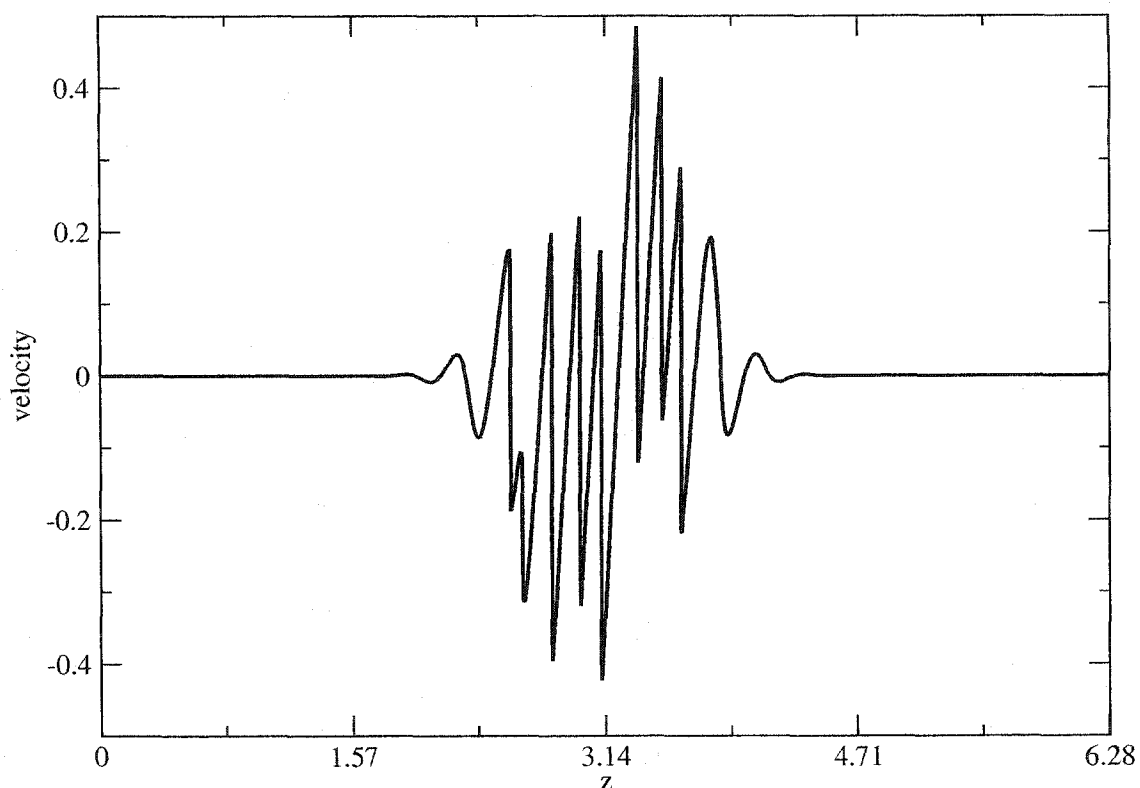
Velocity vs. z at $t=640$ 

Figure 9.14: *The velocity profile after 640 LBM time steps. The velocity profile has formed characteristic sawtooth shapes.*

Figure (9.15) and (9.16) show the “x” and “y” components of the magnetic field, respectively after 640 LBM time steps. The magnetic profiles have evolved to form step like shapes with spikes in the regions where the velocity shock fronts have coalesced. These spikes indicate the continued existence of a mediative effect between the magnetic field and coalescing shock fronts, although it occurs at a very small spatial scale due to the high Reynolds and magnetic Reynolds numbers.

A plot of the kinetic, magnetic and total energy is shown in Fig. (9.17). Much of the kinetic energy is initially transferred to magnetic energy as sawtooth shocks form. During this period, the magnetic energy increases exponentially, a characteristic of

B_x vs. z at $t=640$

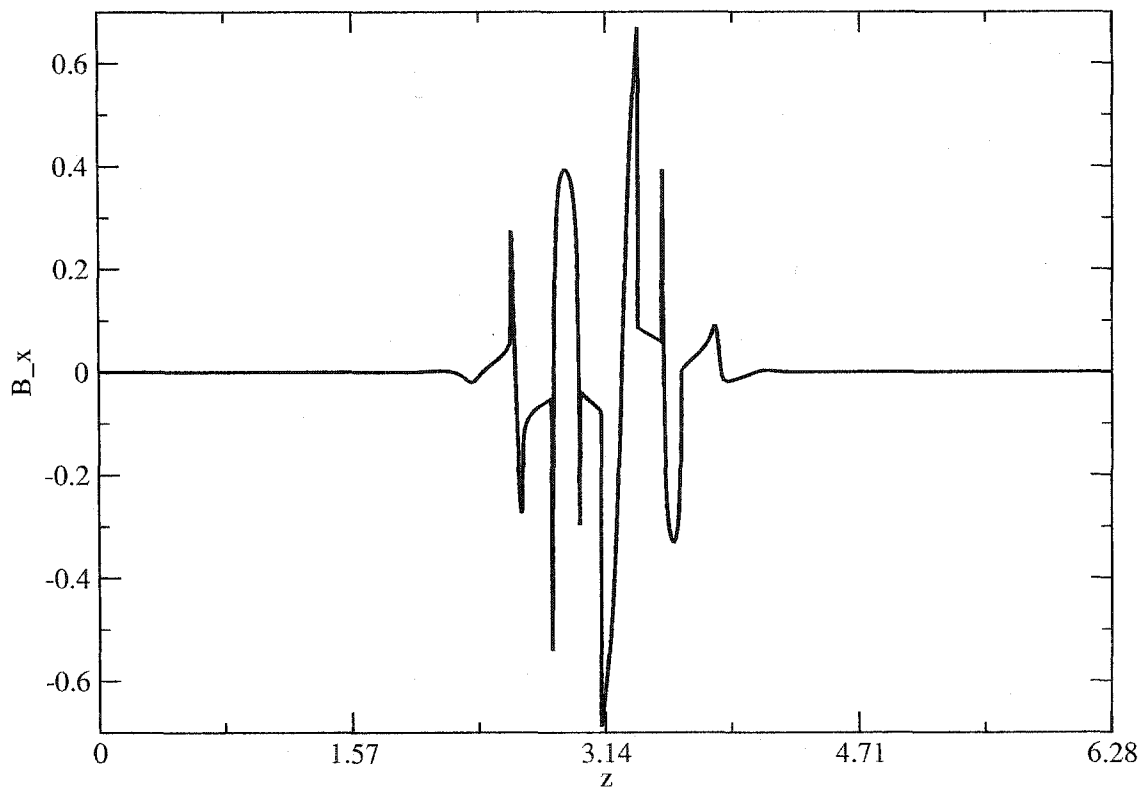


Figure 9.15: The profile of the “ x ” component of the magnetic field after 640 LBM time steps. The profile has formed characteristic step like shapes with spikes in the regions where velocity shock fronts have coalesced.

the formation of thin current sheets. The total energy does not begin to decay until a limit in the exponential increase in magnetic energy is reached after roughly 160 LBM time steps. From this point on, the majority of the total energy of the system is contained in the magnetic field. During the period from 640 to 1280 LBM time steps, a small portion of the magnetic energy is transferred back to kinetic energy, interrupting the dissipative decay of the magnetic energy slightly.

A useful check of the performance of numerical simulations of one dimensional fluid flow comes from analyzing the energy spectra in wave number space. Tur-

B_y vs. z at t=640

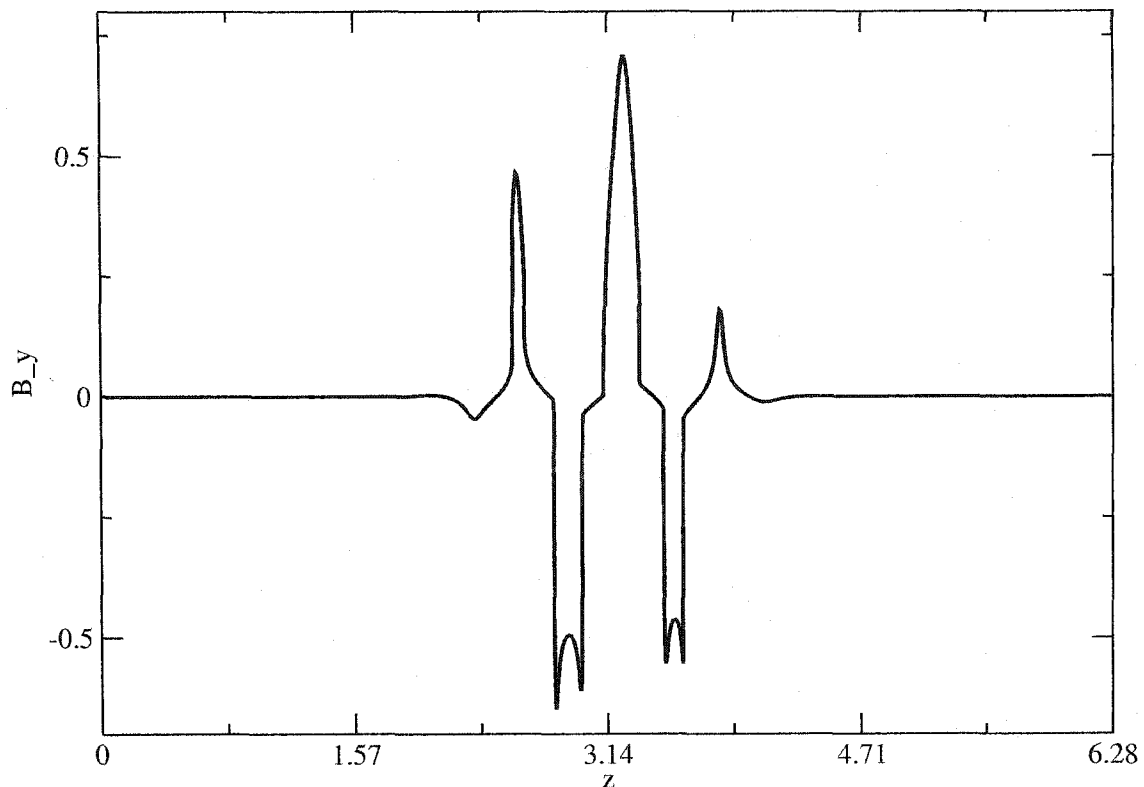


Figure 9.16: *The profile of the “y” component of the magnetic field after 640 LBM time steps. This profile has also formed characteristic step like shapes with spikes in the regions where velocity shock fronts have coalesced.*

bulence theory indicates that the energy in wavenumber (k) space should scale as k^{-2} [15, 4, 29]. While the dissipative terms in the velocity and magnetic induction equations tend to inhibit the strict k^{-2} scaling, this effect is negligible for large Reynolds and magnetic Reynolds numbers. The presence of a magnetic field also tends to inhibit the strict k^{-2} scaling of the kinetic energy slightly. This is equivalent to the mediative effect that the magnetic field has on coalescing shock fronts. However, the total energy for large values of the Reynolds and magnetic Reynolds numbers should display a strong k^{-2} dependence as the magnetic energy spectrum

Kinetic, Magnetic and Total Energy vs. Time

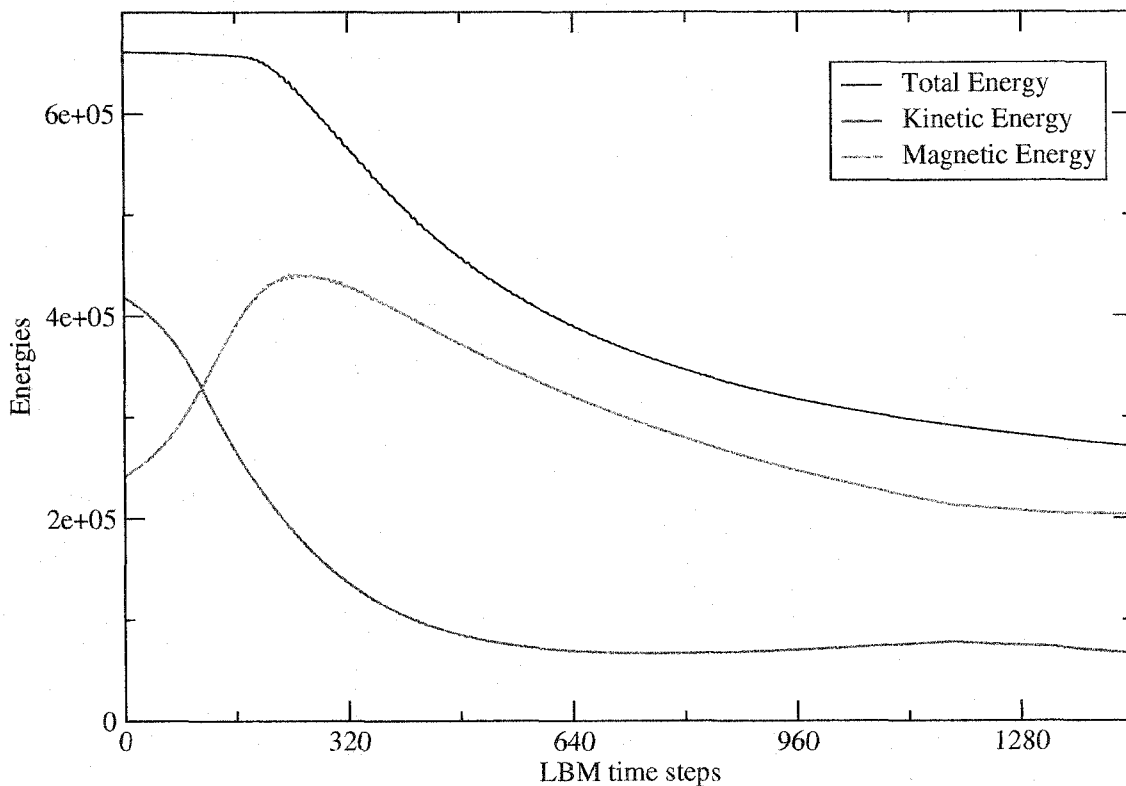


Figure 9.17: A plot of the kinetic, magnetic and total energy as a function of time. Much of the kinetic energy is transferred to magnetic energy during the formation of steep sawtooth shocks. The total energy then begins to dissipate due to the viscous and resistive effects.

acts to compensate for deficiencies in the kinetic energy spectrum. The fast Fourier transform of the velocity and magnetic fields were taken using the DFFFTRF subroutine from the International Mathematical and Statistical Libraries. The kinetic, magnetic, and total energy at a given time were defined as

$$E_{kin}(k) = \frac{1}{2}v(k, t_n)^2, \quad (9.10)$$

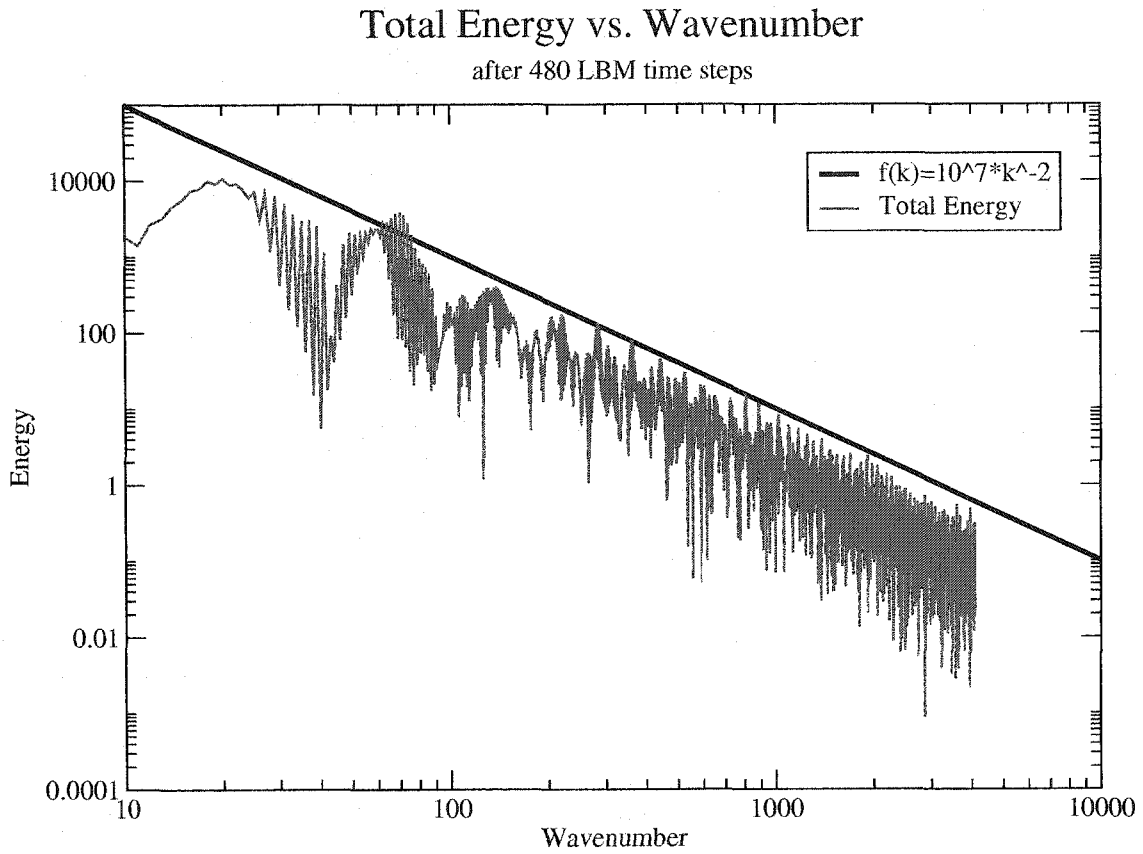


Figure 9.18: A log-log plot of the total energy in wavenumber space compared against a reference function. The total energy displays a strong k^{-2} dependence.

$$E_{mag}(k) = \frac{1}{2}[B_x(k, t_n)^2 + B_y(k, t_n)^2], \quad (9.11)$$

$$E_{tot}(k) = E_{kin}(k) + E_{mag}(k). \quad (9.12)$$

Figure (9.18) shows the total energy in wavenumber space after 480 LBM time steps. Both of the axes use a logarithmic scaling. The function

$$f(k) = 10^7 k^{-2} \quad (9.13)$$

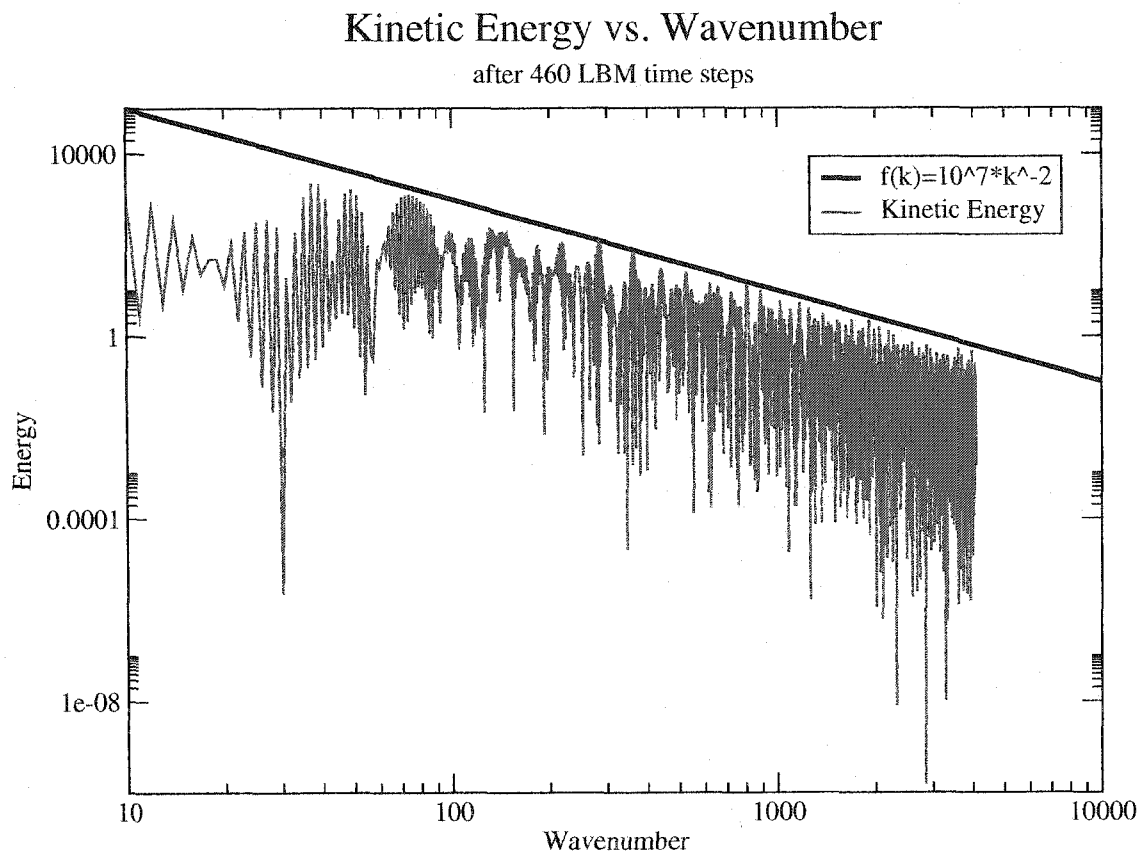


Figure 9.19: A log-log plot of the kinetic energy in wavenumber space compared against a reference function. The kinetic energy displays a k^{-2} dependence with some initial fall off for low values of the wavenumber due to the anisotropic initial spectrum.

is plotted in black for comparison against the energy spectra. The total energy demonstrates strong agreement with the k^{-2} scaling rule. Further, the use of a computationally efficient non-uniform grid has allowed us to recover the correct scaling even for large value of the wavenumber. Traditionally, less refined computational procedures see a pile up of the energy in the region of large wavenumbers due to their inability to transfer the energy to higher wavenumbers. Figure (9.18) thus demonstrates this resolution problem can be fixed with the non-uniform refinement of the region around the turbulent activity, which eliminates the need for a global refinement. Figure (9.19) shows a log-log plot of the kinetic energy spectra in wavenumber

Magnetic Energy vs. Wavenumber

after 460 LBM time steps

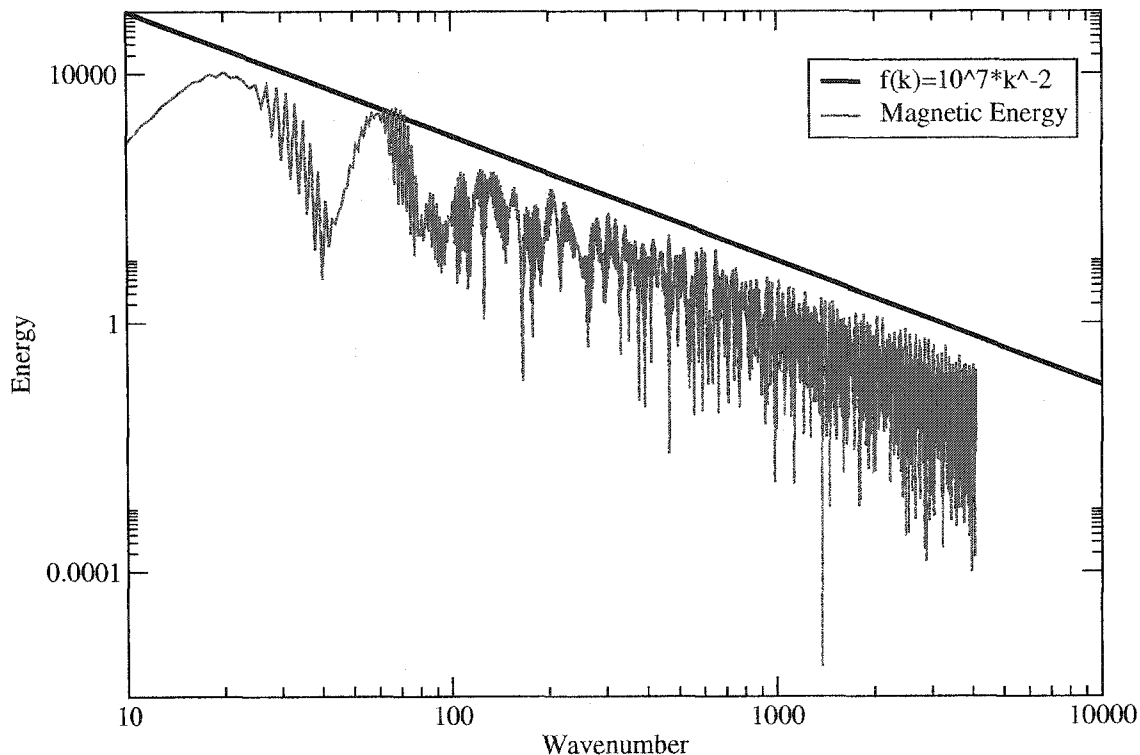


Figure 9.20: A log-log plot of the magnetic energy in wavenumber space compared against a reference function. The magnetic energy displays a k^{-2} dependence with some initial fall off for low values of the wavenumber due to the anisotropic initial spectrum.

space. The kinetic energy also shows strong agreement with the k^{-2} scaling rule. Finally, a log-log plot of the magnetic energy spectra is shown in Fig. (9.20), which also demonstrates the k^{-2} scaling rule.

Our simulation of this set of Gaussian wave packet initial conditions, which contain comparable amounts of kinetic and magnetic energy have yielded some interesting results. Namely, we have seen the formation of the characteristic sawtooth shapes in the velocity field and step like shapes in the magnetic field components. The spikes in the magnetic field at the region where the velocity shocks coalesce indicate that the magnetic field continues to have a mediative effect of the veloc-

ity shock fronts although this effect is much less pronounced for large Reynolds and magnetic Reynolds numbers. The transfer of energy behaves such that the magnetic energy increases exponentially as the velocity shocks are formed. After which, the total energy begins to dissipate due to the presence of the viscosity and resistivity terms.

9.3 1-D MHD Simulation Using an Initially Large Magnetic Field

We have now seen the evolution of profiles, which contain an initially large kinetic energy and small magnetic energy and of profiles, which contain comparable amounts of kinetic and magnetic energy. As an obvious next step, we will investigate the evolution of a profile that contains an initially large magnetic energy and an initially small kinetic energy. Because the previous simulations have consisted primarily of the transfer of kinetic to magnetic energy, we hope to create a situation where a strong transfer from magnetic to kinetic energy develops. This situation forms the one dimensional analogue to two and three dimensional magnetic reconnection; a process that creates large particle velocities from the reconnection and relaxation of the magnetic topology. In one dimensional MHD we are not able to simulate the reconnection of the magnetic field lines, but we can create a region of high current density, which should excite large peaks in the velocity field.

For this simulation we use Gaussian wave packets similar to those used in section 9.2. The initial profiles of the fields take the form

$$v(z) = v_0 \sin(z), \quad (9.14)$$

Initial Field Profiles

v, B_x and B_y vs. z

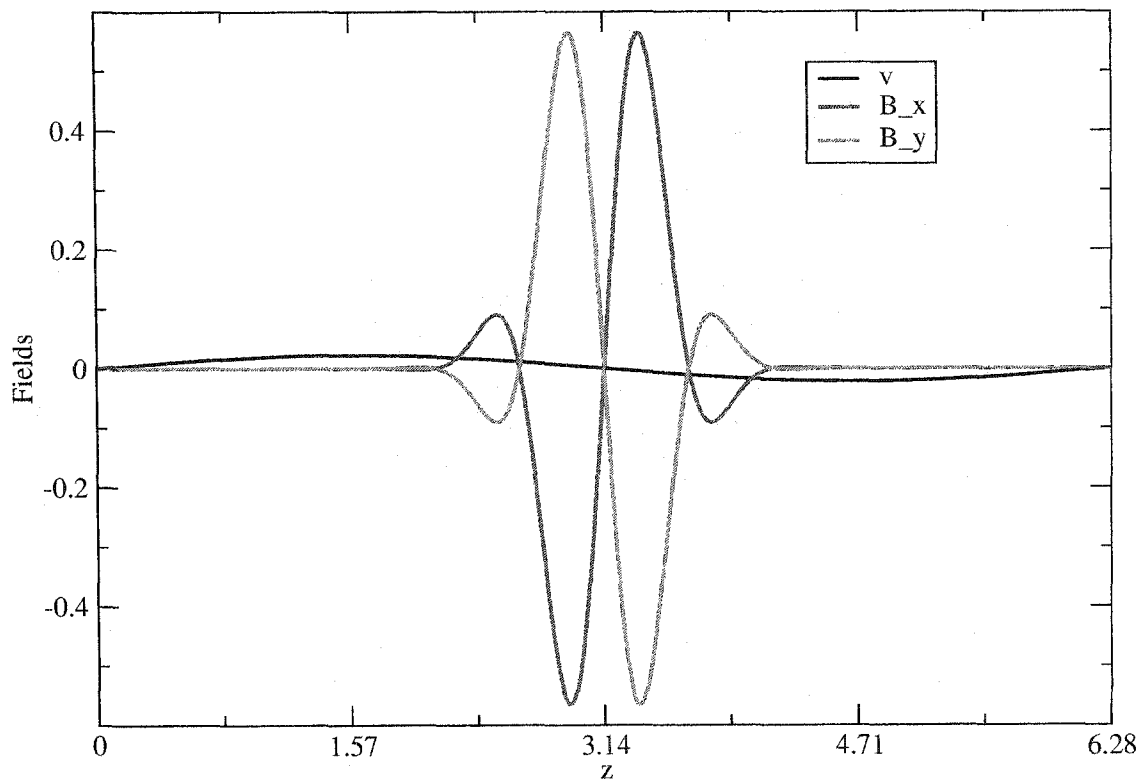


Figure 9.21: The profile of the initial fields. The magnetic field contains most of the initial energy.

$$B_x(z) = B_{x,0} \exp[-4.0(z - \pi)^2] \sin(6z), \quad (9.15)$$

$$B_y(z) = B_{y,0} \exp[-4.0(z - \pi)^2] \sin(6z) \quad (9.16)$$

where the initial velocity field was set to $v_0 = .02236$ and the initial magnetic field was set to $B_x = B_y = .7071$. The kinetic energy, hence accounts for only ten percent of the total energy and the magnetic energy accounts for the remaining majority. The initial profile of the fields is shown in Fig. (9.21).

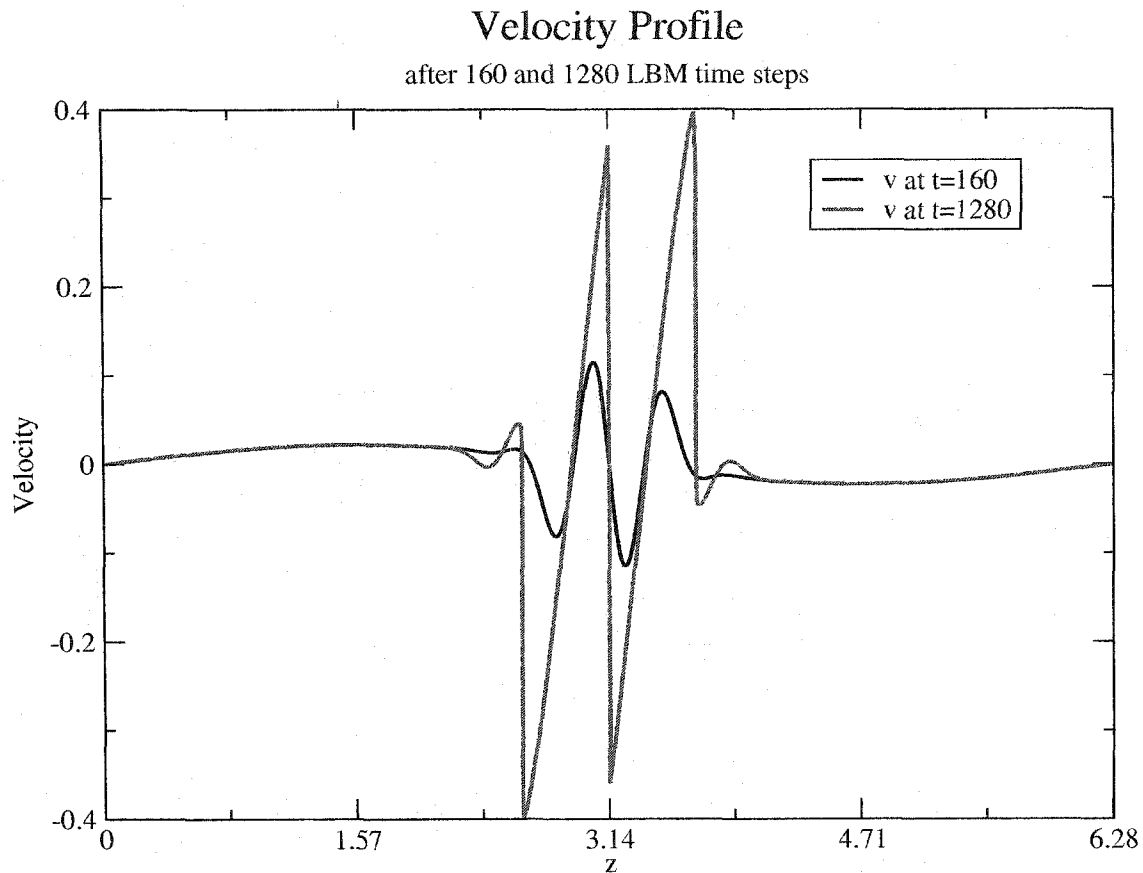


Figure 9.22: *The velocity profile after 160 and 1280 LBM time steps. The regions of large current have excited oscillations in the velocity field, which grow in energy and then form sawtooth shocks.*

The relaxation constants were set to $\tau_\nu = \tau_\mu = .55$ and the dissipative parameters were set to $\alpha = \beta = \frac{25}{3}$ to give a viscosity and resistivity of $\nu = \mu = .4167$. A non-uniform grid was used with 1025 nodes spanning the region from 0 to $\frac{\pi}{2}$, 8192 nodes spanning the region from $\frac{\pi}{2}$ to $\frac{3\pi}{2}$, and 1025 nodes spanning the region from $\frac{3\pi}{2}$ to 2π . The central region hence uses a refinement factor of $m = 4$. The resulting Reynolds number is $R = 219.8$ and the magnetic Reynolds number is $R_m = 9830.4$. The simulation was run for 14450 LBM time steps.

The profile of the velocity field after 160 and 1280 LBM time steps is shown in

Magnetic Field Profile

B_x after 160 and 1280 time steps

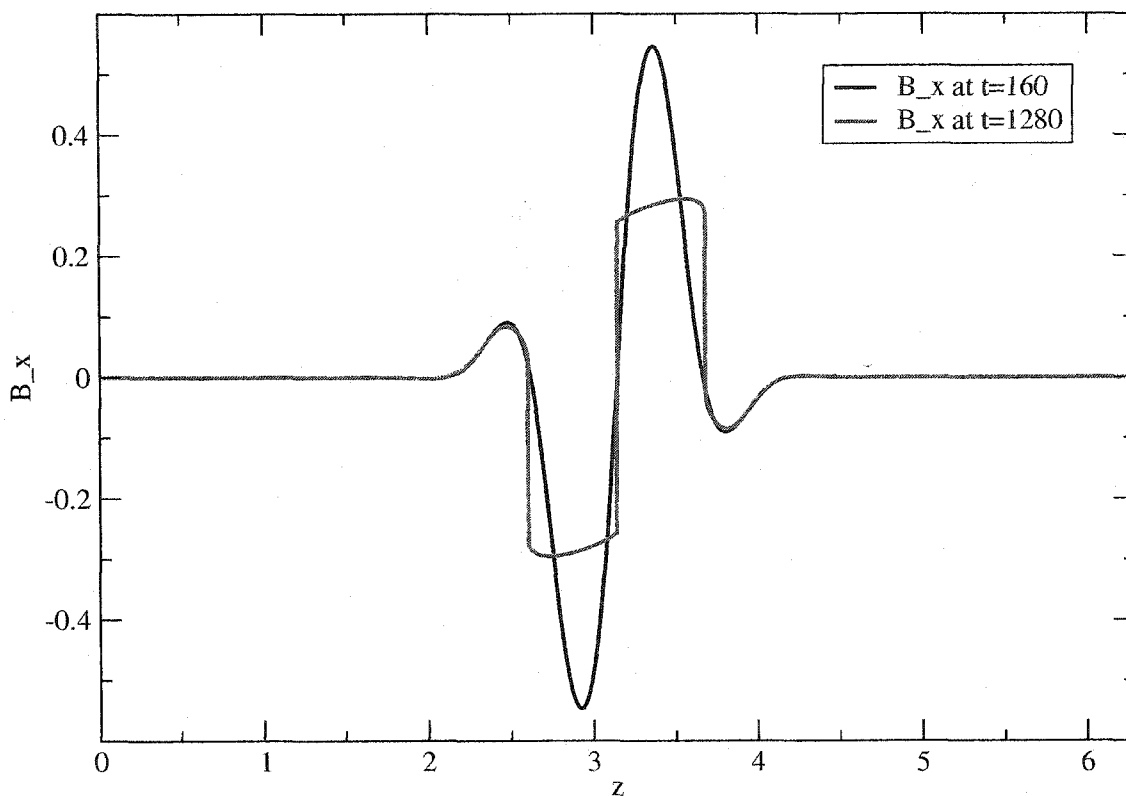


Figure 9.23: The “x” component of the magnetic field after 160 and 1280 LBM time steps. The magnetic oscillations loose energy and then distort to form step like shapes as the velocity profile forms sawtooth shocks.

Fig. (9.22). After 160 LBM time steps the magnetic field has transferred some of its energy to the velocity field to form small oscillations. The peaks of the oscillations occur in the region of large currents where the current is defined as the curl of the magnetic field

$$J_x(z) = -\partial_z B_y(z), \quad (9.17)$$

Magnetic Field Profile

B_y after 160 and 1280 time steps

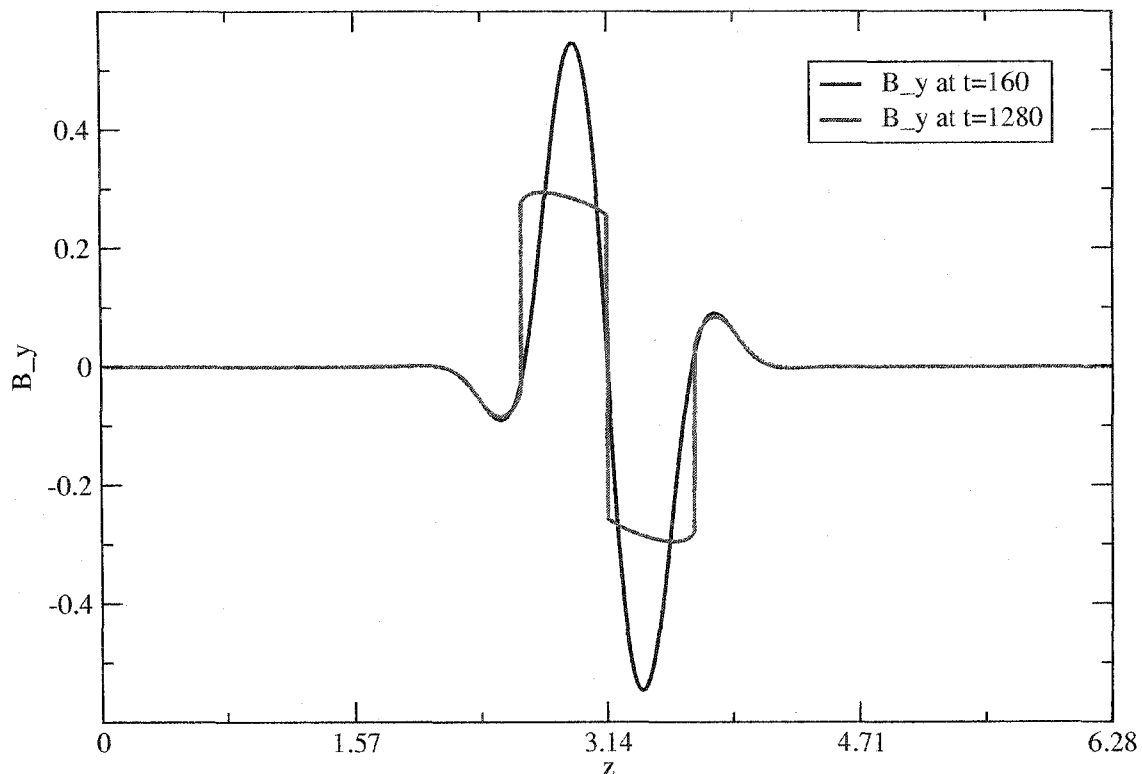


Figure 9.24: The “y” component of the magnetic field after 160 and 1280 LBM time steps. This profile mirrors the “x” component of the magnetic field.

$$J_y(z) = -\partial_z B_x(z). \quad (9.18)$$

After 1280 LBM time steps, the velocity profile has gained more energy and the velocity oscillations have begun to evolve into saw tooth shocks. Figures (9.23) and (9.24) show the profiles of the “x” and “y” components of the magnetic field after 160 and 1280 LBM time steps. The oscillations in the magnetic field initially decay without losing their initial shape as energy is transferred to the velocity field. After the velocity field gains a significant amount of energy and begins to form sawtooth shocks, it acts back on the magnetic field causing the distorted step like functions

Kinetic, Magnetic and Total Energy vs. Time

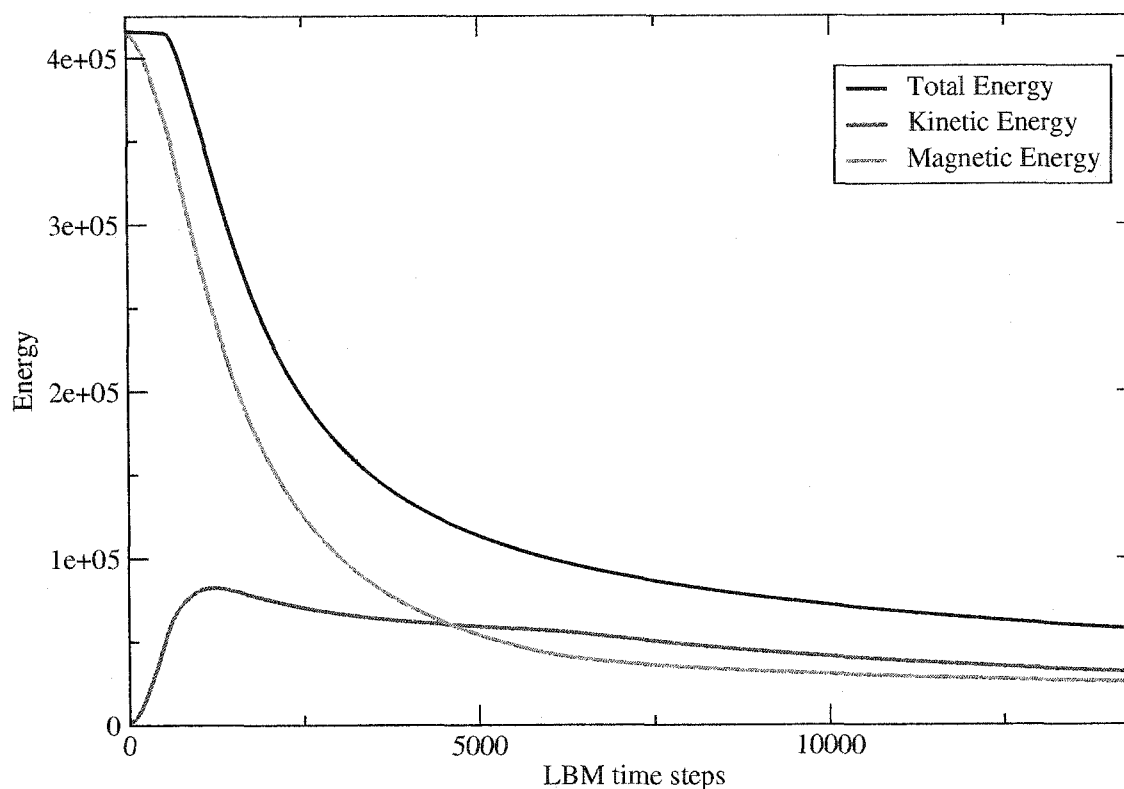


Figure 9.25: *The kinetic, magnetic, and total energy evolution in time. The kinetic energy increases exponentially during the initial period. After which, all of the energy decays away due to the presence of the dissipative terms.*

that are visible after 1280 LBM time steps.

The kinetic, magnetic, and total energy plotted in time is shown in Fig. (9.25). The transfer of energy closely resembles that of the simulation which began with a majority of the energy contained in the velocity field. The magnetic energy is initially transferred to the velocity field and after sawtooth shocks are formed, the total energy begins to dissipate. The kinetic energy increases exponentially during the formation of the velocity oscillations just as it did in the simulation with large initial kinetic energy.

Figure (9.26) shows a log-log scale plot of the total, kinetic and magnetic energy spectra plotted in wavenumber space. All of the energy spectra demonstrate a strong k^{-2} dependence although there appears to be some fall off for large wavenumbers. This shows that the magnetic field transfers energy to the velocity field in a cascading manner; similar to the way that kinetic energy is transferred to magnetic energy.

An interesting aspect of this evolution comes from the invariance of the energy transfer procedure whether it proceeds from a large initial kinetic energy or a large initial magnetic energy. In both cases the total energy does not begin to decay until a large portion of the dominant field has been transferred to the passive field. Also the passive field acquires energy at exponential rates during the initial period. This interestingly contrasts with the evolution of the shapes of the field profiles. If the velocity field dominates the initial profile it immediately begins to form sawtooth shocks that distort the magnetic field. Where as a dominant magnetic field decays away without distortion of the initial shape. Only after the velocity oscillations grow sufficiently large and begin to evolve into sawtooth shocks does the magnetic field begin to be distorted.

We thus conclude our simulations of one dimensional resistive magnetohydrodynamics with a strong understanding of the phenomena that characterizes one dimensional MHD turbulence. The invariance of the transfer of kinetic and magnetic energy has been demonstrated in simulations which use one initially large field. The energy spectra have been found to demonstrate a k^{-2} scaling rule. Finally, the total energy has been shown to be initially constant in time during the transfer of energy and then to dissipate after the formation of sawtooth shocks in the velocity field.

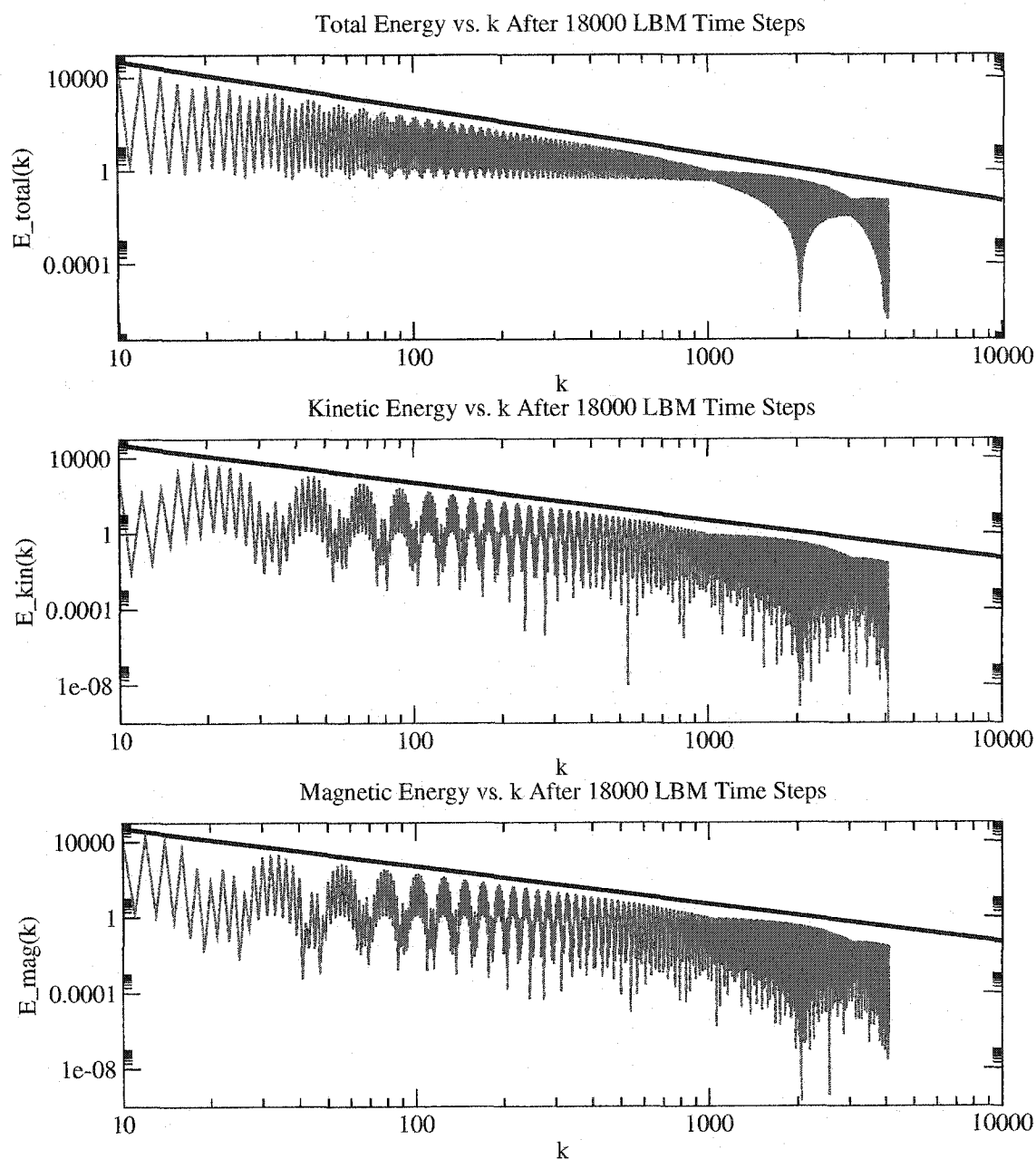


Figure 9.26: A log-log plot of the kinetic, magnetic, and total energy spectra in wavenumber space after 18000 LBM time steps. A reference k^{-2} function is also plotted in black for comparison. The kinetic, magnetic, and total energy spectra all show a strong k^{-2} dependence with some fall off for large values of k .

CHAPTER 10

Conclusion

The study of turbulent one and two dimensional dissipative single fluid systems reveals a large amount of fascinating dynamic phenomena. The development of lattice Boltzmann methods for one and two dimensional magnetohydrodynamic systems has allowed us to examine the turbulent and dissipative evolution of these systems to gain some insight into the physical processes, which govern dissipative magnetohydrodynamic turbulence.

Our development of the octagonal scalar-vector LBM for dissipative MHD represent a significant improvement over previous bi-directional streaming models. The model has the advantage of an inherently simpler algebraic form due to the removal of the coupled bi-directional streaming vectors. Additionally the octagonal streaming lattice produces a higher degree of rotational symmetry, relative to the square and hexagonal streaming lattices. As a result, the tensors formed from products of the streaming vectors summed over all of the streaming directions have a higher level of isotropy than their square and hexagonal counterparts. With the cost of an additional interpolation step, the higher isotropy results in increased numerical sta-

bility and the ability to investigate simulations with higher Reynolds and magnetic Reynolds numbers.

Our simulations of the Orszag-Tang vortex model agree with previous spectral simulations and demonstrate most of the notable features of MHD turbulence. In our simulations of the Orszag-Tang and modified Orszag-Tang vortex models we have seen clear evidence of the mutual interaction between the velocity and magnetic field profiles. These profiles begin with large scale current and vorticity structures that evolve to form thin sheets of current and vorticity. In the later stages of the evolution, the effects of the viscosity and resistivity terms begin to dissipate the total energy of the system.

The analysis of one dimensional dissipative magnetohydrodynamic systems provides some useful insight into the evolution of turbulent systems. Our development of lattice Boltzmann methods that utilize a non-uniform distribution of grid points provides an efficient numerical scheme for simulating these one dimensional systems. In particular, the use of non-uniform grids provide a cost effective method for decreasing the numerical oscillations that arise from low resolution simulations. The computational expenditure of non-uniform grid LBMs is significantly decreased because non-uniform grid LBMs allow us to focus the majority of our computational effort around the regions where the velocity and magnetic fields develop large gradients.

In our simulations of one dimensional MHD systems we have seen the turbulent interaction and dissipative decay of the velocity and magnetic field profiles. The invariance of the transfer of energy from kinetic to magnetic and from magnetic to kinetic is particularly striking. This is contrasted with the lack of invariance in the evolution of the velocity and magnetic fields themselves. In particular, we have shown that the dominant initial field transfers energy to the passive field during the

turbulent initial stage of the evolution. During this time period, the passive field demonstrates an exponential increase in energy and the total energy is conserved. In the later stages of the evolution, the total energy decays due to the presence of the viscosity and resistivity terms. Examination of the velocity profile reveals that the initial formation of sawtooth shocks is responsible for the initial transfer of kinetic energy to magnetic energy. The convergence and interaction of the shock fronts, through the magnetic field, then stimulates the dissipative decay. The magnetic field profiles, however retain their initial shapes while they transfer energy to the velocity profile. Only after the velocity profiles gain sufficient energy, do they evolve to form sawtooth shocks. The formation of these sawtooth shocks then distorts the shape of the magnetic field profiles and the dissipative decay of the total energy begins.

Any rigorous scientific quest answers a few of the questions that the scientist set out to answer, but more importantly, reveals an astonishing array of compelling new questions that merit careful investigation. The acute scientist will then prove his worth, by selecting a scientific program which answers the most compelling questions. Without making any claims about our acuteness in developing a scientific program, we will now suggest a number of future topics that are meritorious of further investigation. These topics can be broadly classified as developments in LBMs that will aid in the application of the methods to the simulation of realistic plasma physics problems, and those that continue to test the limits of the LBM kinetic modeling procedure.

After developing and investigating one and two dimensional LBMs for resistive MHD the obvious next step would be to develop a three dimensional LBM model. Such a model could be used to investigate a number of interesting phenomena in space plasma physics. The applicability of three dimensional LBMs would be fur-

ther aided by the inclusion of toroidal boundary conditions. This would allow for the investigation of the plasma phenomena that occur within Tokamak fusion reactors, which have direct political and socio-economic implications. These large scale three dimensional simulations would clearly benefit from the use of a computational algorithm, which adaptively distributes the grid points in a non-uniform manner in order to resolve regions containing large field gradients in more detail. Finally, the desire to increase the Reynolds and magnetic Reynolds numbers to the regime of weakly viscous and resistive Tokamak plasmas provides the impetus for the development of LBMs that use implicit time stepping. Implicit time stepping, although computationally expensive, is widely known to increase the numerical stability of finite difference models.

In testing the limits of the kinetic modeling procedure used in LBMs, it would be interesting to develop more sophisticated MHD models that include some of the higher order kinetic effects. The inclusion of Landau damping into LBMs could serve as a first step in investigating whether LBMs are capable of reproducing these kinetic effects. One could also investigate the development of a two fluid LBM approach. By developing an LBM for the ion and electron fluid equations one could potentially recover aspects of the finite (rather than infinitesimal) interaction between ions and electrons such as the effects of a finite Larmor radius.

Whatever they may be, the future development of lattice Boltzmann models and their application to magnetohydrodynamic turbulence should prove to be an interesting scientific endeavor. Furthermore, the continued development of computational algorithms of all kinds have become an essential component of the design of new experiments and of the testing of new theoretical models. The exponential increase in computational resources will only increase the scientific community's dependence on these computational tools.

BIBLIOGRAPHY

- [1] D. Balsara. Total time diminishing scheme for adiabatic and isothermal magnetohydrodynamics. *Astrophysical Journal Supplement Series*, 116:133–153, May 1998.
- [2] P. Bhatnagar, E. Gross, and M. Krook. A model for collisionless process in gases. i. small amplitude processes in charged and neutral one-component system. *Physical Review*, 94:511, 1954.
- [3] D. Biskamp. Current sheet profiles in two-dimensional magnetohydrodynamics. *Physics of Fluids B-Plasma Physics*, 5(11):3893–3896, November 1993.
- [4] D. Biskamp. *Magnetic Reconnection in Plasmas*. Cambridge University Press, New York, NY, 2000.
- [5] D. Biskamp and H. Welter. Dynamics of decaying two-dimensional magnetohydrodynamic turbulence. *Physics of Fluids B-Plasma Physics*, 1(10):1964–1979, October 1989.
- [6] J. Brackbill and D. Barnes. The effect of nonzero $\text{div } \mathbf{b}$ on the numerical solution of the magnetohydrodynamic equations. *Journal of Computational Physics*, 35(3):426–430, May 1980.
- [7] S. Chapman and T. Cowling. *The Mathematical Theory of Non-Uniform Gases*. Cambridge University Press, Cambridge, 1990.
- [8] H. Chen, W. Matthaeus, and L. Klein. An analytic theory and formulation of a local magnetohydrodynamic lattice gas model. *Physics of Fluids*, 31(6):1439–1455, June 1988.
- [9] Y. Chen. *Lattice Bhatnagar-Gross-Krook Method for Fluid Dynamics: Compressible, Thermal and Multi-Phase Models*. PhD thesis, University of Tokyo, June 1994.
- [10] P. Dellar. Lattice kinetic schemes for magnetohydrodynamics. *Journal of Computational Physics*, 179(1):95–126, June 2002.

- [11] K. Elsasser. The hydromagnetic equations. *The Physical Review*, 79(1):183, July 1950.
- [12] O. Filippova and D. Hanel. Grid refinement for lattice-bgk models. *Journal of Computational Physics*, 147(1):219–228, November 1998.
- [13] O. Filippova and D. Hanel. Acceleration of lattice-bgk schemes with grid refinement. *Journal of Computational Physics*, 165(2):407–427, December 2000.
- [14] Huang. *Statistical Mechanics*. Cambridge University Press, New York, NY, 2000.
- [15] M. Lesieur. *Turbulence in Fluids*. Kluwer Academic Publishers, Boston, MA, third revised and enlarged edition edition, 1997.
- [16] A. Macnab, G. Vahala, L. Vahala, and P. Pavlo. Lattice boltzmann model for dissipative incompressible mhd. *Proceeding of the 28th Conference on Controlled Fusion and Plasma Physics*. *ECA*, 25(A):853–856, June 2001.
- [17] A. Macnab, G. Vahala, L. Vahala, P. Pavlo, and M. Soe. Some progress in the development of lattice boltzmann methods for dissipative mhd. *Czechoslovak Journal of Physics*, 52(suppliment D):D59–D64, June 2002.
- [18] D. Martinez, S. Chen, and W. Matthaeus. Lattice boltzmann magnetohydrodynamics. *Physics of Plasmas*, 1(6):1850–1867, June 1994.
- [19] S. Orszag and C. Tang. Small-scale structure of two-dimensional magnetohydrodynamic turbulence. *Journal of Fluid Mechanics*, 90(1):129–143, January 1979.
- [20] P. Pavlo, G. Vahala, and L. Vahala. Preliminary results in the use of energy-dependent octagonal lattices for thermal lattice boltzmann simulations. *Journal of Statistical Physics*, 107(1–2):499–519, April 2002.
- [21] R. Polovin and V. Demutski. *Fundamentals of magnetohydrodynamics*. Plenum Publishing Corporation, New York, NY, 1990.
- [22] S. Succi. *The Lattice Boltzmann Equation for Fluid Dynamics and Beyond*. Oxford University Press, New York, NY, 2001.

- [23] S. Succi, I. Karlin, and H. Chen. Colloquium: role of the h theorem in lattice boltzmann hydrodynamic simulations. *Reviews of Modern Physics*, 74(4):1203–1220, October 2002.
- [24] G. Toth. The div $b=0$ constraint in shock-capturing magnetohydrodynamics codes. *Journal of Computational Physics*, 161(2):605–652, July 2000.
- [25] G. Vahala, P. Pavlo, L. Vahala, and N. Martys. Thermal lattice-boltzmann models (tlbm) for compressible flows. *International Journal of Modern Physics C-Physics and Computers*, 9(8):1247–1261, December 1998.
- [26] L. Vahala, D. Wah, G. Vahala, J. Carter, and P. Pavlo. Thermal lattice boltzmann simulation for multispecies fluid equilibration. *Physical Review E-Statistical Physics, Plasmas, Fluids and Related Interdisciplinary Topics*, 62(1):507–516, July 2000.
- [27] D. Wolf-Gladrow. *Lattice Gas Cellular Automata and Lattice Boltzmann Models: an Introduction*. Springer, New York, NY, 2000.
- [28] G. Yan, Y. Chen, and S. Hu. A lattice boltzmann method for kdv equation. *Acta Mechanica Sinica*, 14(1):17–26, 1998.
- [29] S. Yanase. New one dimensional model equations of magnetohydrodynamic turbulence. *Physics of Plasmas*, 4(4):1010–1017, April 1997.
- [30] D. Yu, R. Mei, and W. Shyy. A multi-block lattice boltzmann method for viscous fluid flows. *International Journal for Numerical Methods in Fluids*, 39:99–120, 2001.

VITA

Angus Ian Duncan Macnab

Angus Ian Duncan Macnab was born on May 17, 1975 in Auckland, New Zealand. Graduated from Bellevue High School in Bellevue, Washington, June of 1994. Received a Bachelor of Science degree, from The Evergreen State College in Olympia, Washington, March of 1998. Received a Master of Science degree in physics from the College of William and Mary in Virginia, December of 2000. Received a Doctor of Philosophy degree in physics from the College of William and Mary in Virginia, July of 2003. Accepted a position as a research associate at the Center for Scientific Computation and Mathematical Modeling at the University of Maryland in College Park, Maryland, August of 2003.